Lappeenranta
University of Technology

Nikita Uzhegov

DESIGN AND MATERIAL SELECTION OF HIGH-SPEED ROTATING ELECTRICAL MACHINES

Thesis for the degree of Doctor of Science (Technology) to be presented with due permission for public examination and criticism in the Auditorium 2310 at Lappeenranta University of Technology, Lappeenranta, Finland on the 3rd of June, 2016, at noon.

Acta Universitatis
Lappeenrantaensis 702

Supervisors Professor Juha Pyrhönen
LUT School of Energy Systems
Lappeenranta University of Technology
Finland

Dr. Janne Nerg
LUT School of Energy Systems
Lappeenranta University of Technology
Finland

Reviewers Professor Yujing Liu
Department of Energy and Environment
Chalmers University of Technology
Sweden

Dr. Jenni Pippuri
VTT Technical Research Centre of Finland Ltd.
Finland

Opponents Professor Yujing Liu
Department of Energy and Environment
Chalmers University of Technology
Sweden

Dr. Jenni Pippuri
VTT Technical Research Centre of Finland Ltd.
Finland

ISBN 978-952-265-965-1
ISBN 978-952-265-966-8 (PDF)
ISSN-L 1456-4491
ISSN 1456-4491

Lappeenrannan teknillinen yliopisto
Yliopistopaino 2016

Abstract

Nikita Uzhegov
Design and Material Selection of High-Speed Rotating Electrical Machines
Lappeenranta 2016
60 pages

Acta Universitatis Lappeenrantaensis 702
Diss. Lappeenranta University of Technology
ISBN 978-952-265-965-1, ISBN 978-952-265-966-8 (PDF), ISSN-L 1456-4491, ISSN 1456-4491

The increasing emphasis on energy efficiency is starting to yield results in the reduction in greenhouse gas emissions; however, the effort is still far from sufficient. Therefore, new technical solutions that will enhance the efficiency of power generation systems are required to maintain the sustainable growth rate, without spoiling the environment. A reduction in greenhouse gas emissions is only possible with new low-carbon technologies, which enable high efficiencies.

The role of the rotating electrical machine development is significant in the reduction of global emissions. A high proportion of the produced and consumed electrical energy is related to electrical machines. One of the technical solutions that enables high system efficiency on both the energy production and consumption sides is high-speed electrical machines. This type of electrical machines has a high system overall efficiency, a small footprint, and a high power density compared with conventional machines. Therefore, high-speed electrical machines are favoured by the manufacturers producing, for example, microturbines, compressors, gas compression applications, and air blowers.

High-speed machine technology is challenging from the design point of view, and a lot of research is in progress both in academia and industry regarding the solution development. The solid technical basis is of importance in order to make an impact in the industry considering the climate change.

This work describes the multidisciplinary design principles and material development in high-speed electrical machines. First, high-speed permanent magnet synchronous machines with six slots, two poles, and tooth-coil windings are discussed in this doctoral dissertation. These machines have unique features, which help in solving rotordynamic problems and reducing the manufacturing costs.

Second, the materials for the high-speed machines are discussed in this work. The materials are among the key limiting factors in electrical machines, and to overcome this limit, an in-depth analysis of the material properties and behavior is required. Moreover, high-speed machines are sometimes operating in a harsh environment because they need to be as close as possible to the rotating tool and fully exploit their advantages. This sets extra requirements for the materials applied.

Keywords: electrical machine, high-speed, design process, permanent magnet synchronous machine, tooth-coil winding, aging, active magnetic bearing

Acknowledgments

This work was carried out during the years 2012–2016 at the Laboratory of Electrical Drives Technology at Lappeenranta University of Technology (LUT), Finland. The research was funded by Lappeenranta University of Technology.

First of all, I would like to thank my supervisor Professor Juha Pyrhönen for his guidance and infinite optimism. I am grateful to you for being an example for me and many other people, and for your skills to motivate and lead the researchers. Many thanks go to my second supervisor Dr. Janne Nerg for his support and fruitful discussions. It is hard to overestimate your contribution to the publications we have made together.

The comments and constructive advice from the preliminary examiners Professor Yujing Liu from Chalmers University of Technology and Dr. Jenni Pippuri from VTT Technical Research Centre are highly appreciated.

My sincerest thanks are due to the colleagues from the laboratories of Electrical Drives Technology, Machine Design, Fluid Dynamics, Control Engineering and Digital Systems, and LUT Voima. I have learned a lot in our various collaboration projects, which made this doctoral dissertation possible.

I am grateful to Dr. Sergei Shirinskii from Moscow Power Engineering Institute, Dr. Emil Kurvinen, and Dr. Arto Pihlajamäki from LUT for developing the ideas of the journal papers and for their continuous cooperation. I wish to thank Dr. Ilya Petrov for sharing his expertise with me in the course of my studies.

I would like to thank Peter Jones for improving the language in my papers and for the valuable language lessons. I express my gratitude to Dr. Hanna Niemelä for her contribution towards editing the language of this doctoral dissertation and one of the journal papers.

My special thanks go to the SpinDrive Oy team, Dr. Janne Heikkinen, Dr. Alexander Smirnov, and Mr. Teemu Sillanpää. I believe that together we can solve even the most difficult problems.

The financial support by Walter Ahlström Foundation, The Foundation of Technology, The Research Foundation of Lappeenranta University of Technology, and Henry Ford Foundation is gratefully acknowledged.

I extend my heartfelt thanks to my friends from the Czech Republic, Estonia, Finland, Germany, India, Iran, Italy, Kazakhstan, Mexico, the Netherlands, Poland, Russia, and Spain for all activities, trips, and events together. You made my stay in Lappeenranta truly enjoyable.

Finally, I want to thank my dearest Maria for your love, support, and understanding over the years. I wish to thank my father Pavel and mother Elena for your unconditional love and priceless advice. This work would not have been possible without your trust in me.

Nikita Uzhegov
March 2016
Lappeenranta, Finland

Contents

List of publications

Publication I

Uzhegov, N., Pyrhönen, J., and Shirinskii, S., "Loss minimization in high-speed permanent magnet synchronous machines with tooth-coil windings," in *39th Annual Conference of the IEEE Industrial Electronics Society, IECON 2013*, pp. 2960–2965, Nov. 2013

Publication II

Uzhegov, N., Kurvinen, E., and Pyrhönen, J., "Design limitations of 6-slot 2-pole high-speed permanent magnet synchronous machines with tooth-coil windings," in *16th European Conference on Power Electronics and Applications (EPE'14-ECCE Europe), 2014*, pp. 1–7, Aug. 2014

Publication III

Uzhegov, N., Nerg, J., and Pyrhönen, J., "Design of 6-slot 2-pole High-Speed Permanent Magnet Synchronous Machines with Tooth-Coil Windings," in *XXI International Conference on Electrical Machines (ICEM), 2014*, pp. 2537–2542, Sept. 2014

Publication IV

Uzhegov, N., Nerg, and J., Pyrhönen, J., "An Analysis of the 6-Slot 2-Pole High-Speed Permanent Magnet Synchronous Machines with Tooth-Coil Windings," in *41st Annual Conference of the IEEE Industrial Electronics Society, IECON 2015*, pp. 1867–1872, Nov. 2015

Publication V

Uzhegov, N., Kurvinen E., Nerg, J., Pyrhönen, J., Sopanen, J., and Shirinskii, S., "Multidisciplinary Design Process of a 6-Slot 2-Pole High-Speed Permanent Magnet Synchronous Machine," *IEEE Transactions on Industrial Electronics*, vol. 63, no. 2, pp. 784–795, Feb. 2016

Publication VI

Uzhegov, N., Pihlajamäki, A., Nerg, J., and Pyrhönen, J., "Magnetic Wedges in a Steam-resistant Electrical Machine Insulation System," *IEEE Transactions on Dielectrics and Electrical Insulation*, vol. 22, issue 6, pp. 3153–3162, Dec. 2015

Publication VII

Pyrhönen, J., Ruoho, S., Nerg, J., Paju, M., Tuominen, S., Kankaanpää, H., Stern, R., Boglietti, A, and Uzhegov, N., "Hysteresis Losses in Sintered NdFeB Permanent Magnets in Rotating Electrical Machines," *IEEE Transactions on Industrial Electronics*, vol. 62, no. 2, pp. 857–865, Feb. 2015

Nomenclature

Latin alphabet

B	magnetic flux density	T
B_r	permanent magnet remanence	T
D_e	external diameter of the stator	m
D_r	rotor outer diameter	m
D_δ	air gap diameter	m
I	current	A, RMS
k_{Fe}	space factor for iron	–
l	active stator length	m
l_{PM}	permanent magnet length	m
n	rotational speed	rpm
p	number of poles	–
Q_s	number of stator slots	–
R	resistivity	Ω·m
T	torque	Nm
U	voltage	V, RMS

Greek alphabet

λ	thermal conductivity	W/m·K
ρ	density	kg/m^3

Subscripts

n	nominal
PM	permanent magnet
r	rotor
s	stator
δ	air gap

Abbreviations

2D	two-dimensional
3D	three-dimensional
Al-Fe	aluminum-iron
AMB	active magnetic bearing
Co-Fe	cobalt-iron
COP21	21st Conference of the Parties to UNFCCC
DFMA	Design for Manufacture and Assembly
DW	distributed windings
FEM	finite element method

FTIR	Fourier Transform Infrared spectroscopy
GHG	greenhouse gas
HS	high-speed
HVAC	heating, ventilation and air conditioning
IEA	International Energy Agency
IM	induction machine
LUT	Lappeenranta University of Technology
NdFeB	neodymium-iron-boron (magnet)
ORC	Organic Rankine Cycle
PEEK	polyetheretherketone
PM	permanent magnet
PMSG	permanent magnet synchronous generator
PMSM	permanent magnet synchronous machine
rpm	revolutions per minute
Si-Al-Fe	silicon-aluminum-iron
Si-Fe	silicon-iron
SmCo	samarium-cobalt (magnet)
TC	tooth-coil (winding)
THD	total harmonic distortion
UMP	unbalanced magnetic pull
UNFCCC	United Nations Framework Convention on Climate Change

1 Introduction

Sustainable growth of the world economy is only possible with clever deployment of electrical energy, which is a critical resource. According to the report of the International Energy Agency, the global energy demand in 2015 was about 21 000 TWh, and it will grow from the present level by more than 15% by 2020, and by more than 30% by 2030 (IEA, 2015). Power generation is following this demand and expanding its capacities. This situation inevitably seems to lead to an increase in global CO_2 emissions despite the actions governments have decided to take. The emphasis on the energy efficiency together with the carbon markets and other important measures are aimed to decrease the current level of greenhouse gas (GHG) emissions. These steps are starting to bring valuable results; however, the effort is still far from sufficient.

Political regulations play a very important role in the reduction of CO_2 emissions. Extending the Kyoto Protocol, the United Nations Framework Convention on Climate Change (UNFCCC) was adopted in 1992. According to this document, targets for the reduction of GHG emissions were set for industrialised countries. The recent steps in these regulations were taken in the 21st Conference of the Parties to the United Nations Framework Convention on Climate Change (COP21) in December 2015. The major outcome of this meeting is a new international agreement on climate change, which will allow keeping global warming below 1.5–2 °C.

Together with political regulations and strategies, new technical solutions that will enhance the efficiency of energy systems are required. These actions will make it possible to maintain the current economic growth rate without dramatic environmental consequences. Rotating electrical machines are used in industry all over the world, and they play a significant role in energy consumption and production. At present, the electrical machines account for about 40% of the electric energy demand (de Almeida et al., 2014). This fact shows the need to develop new highly efficient solutions in the field because they have a direct influence on the global GHG emissions.

One field of technical solutions aimed to enhance the energy efficiency on both the generation and consumption sides is provided by high-speed (HS) electrical machines. Because of their advantages, these machines are used in a vast array of industrial applications. These benefits include a higher overall system efficiency in certain applications, a higher power density, and a smaller footprint compared with conventional electrical machines (Bianchi et al., 2003). The manufacturers producing gas compression equipment, micro and small gas turbines, machine tools, spindle drives, air blowers, and vacuum pumps are highly interested in the advantages of the high-speed machinery and use them in their applications.

Over the last decade, the markets in which high-speed machines have shown their benefits have been growing exceptionally. For example, the oil and gas compressor market is estimated to reach 9.5 billion EUR in 2018 (GIA, 2011), and the heating, ventilation, and

air conditioning (HVAC) market is estimated to be 75.5 billion EUR in 2018 (TMR, 2012).

High-speed electrical machines are challenging from the design point of view, which has led to extensive research in the field. At Lappeenranta University of Technology (LUT), the HS machinery has been a research topic for more than 25 years (Sihvo, 2010; Aho, 2007; Huppunen, 2004; Pyrhönen, 1991). An indicator of the high importance of this topic is the number of collaborating projects between LUT and the industry on HS machines and the related equipment.

This doctoral dissertation continues the research in the field of high-speed electrical machines. The main objectives include design and optimization of the HS permanent magnet synchronous machine (PMSM) with proposed topology and selection of the materials for the HS electrical machines.

1.1 High-speed electrical machines

There is no exact definition of the term high-speed electrical machine. Most of the authors agree that a machine with the rotor peripheral speed above 100–150 m/s supplied by a frequency converter can be considered a high-speed machine (Binder & Schneider, 2007). Another interesting criterion is to use the HS–index presented in (Moghaddam, 2014). The HS–index is the product of the electrical machine nominal power and speed. Its behavior depends on the rotational speed in different machines.

The most popular machine types among HS machines are the permanent magnet synchronous machine and the induction machine (IM) (Pyrhönen et al., 2008a). These HS electrical machine types are usually used in the majority of industrial applications. Each of these machine types has its benefits and drawbacks, and the final selection is always application dependent. Comparisons of these machine topologies for different applications based on the existing solutions can be found in the literature (Gerada et al., 2014; Moghaddam, 2014; Tenconi et al., 2014).

In general, the advantages of HS IM over HS PMSM are their rigid rotor construction, low-cost materials, and the simpler manufacturing process. Figure 1.1 shows the stator of a manufactured HS IM. This 10 kW, 30 000 rpm machine has two poles and 12 slots. The stator construction of the HS IM is similar to the conventional induction motor.

The key features of the HS machines are usually related to the rotating part. This is due to the high mechanical stresses in the rotor during the operation. The machine shown in Figure 1.1 has a slitted solid rotor, which is the second most rigid rotor construction. The most rigid one is a smooth solid rotor, which may also be equipped with a well-conducting nonferrous coating. However, the power factor and efficiency of the machines equipped with the solid rotor are lower than that of the other solutions (Pyrhönen et al., 2010). The machine of Figure 1.1 was made for an active magnetic bearing (AMB) test rig.

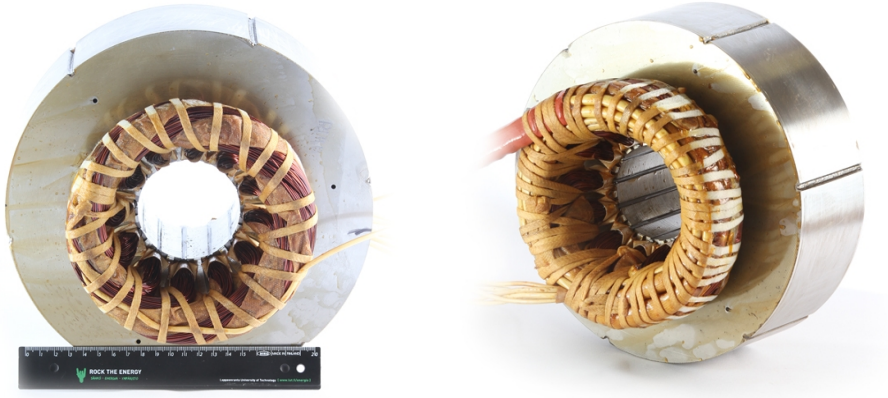

Figure 1.1 Photos of the stator of a 10 kW, 30 000 rpm induction motor

Another example of the HS IMs designed and constructed at LUT is shown in Figure 1.2. The main objective of this machine development was to demonstrate the advantages of the AMB technology for the HS machinery. For this purpose, the industrial stator was kept as it was, and the slitted rotor with copper end rings was redesigned as it was constructed to operate at 12 000 rpm. Because of the implementation of the AMB instead of ball bearings and insignificant electromagnetic changes in the machine, the operating speed and output power from the same volume are increased by 25%.

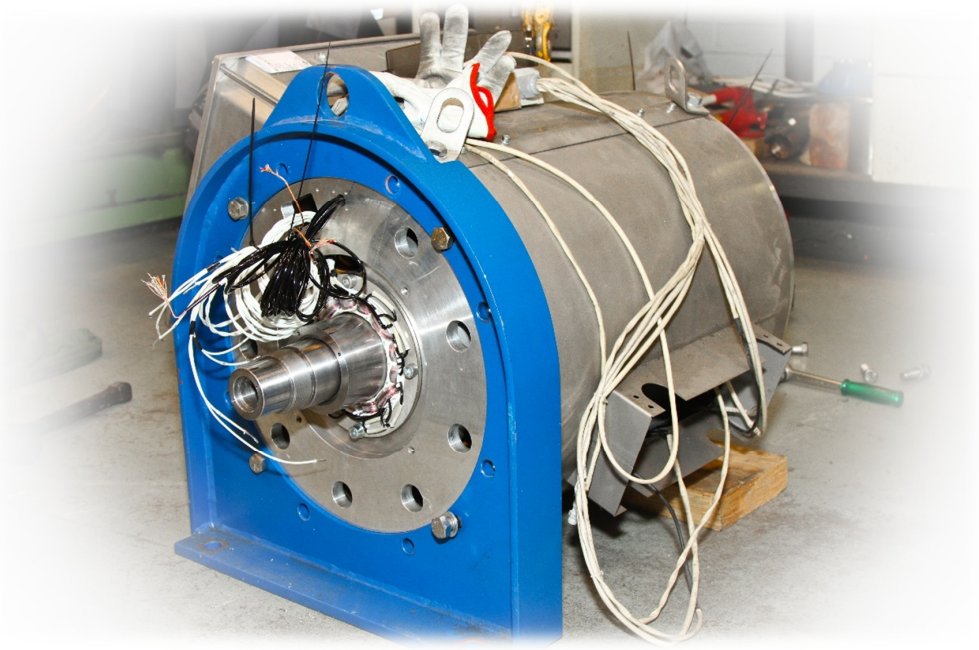

Figure 1.2 Prototype of a 350 kW, 15 000 rpm HS IM with active magnetic bearings

The slitted solid rotor with copper end rings, implemented in this HS IM, is more complex from the manufacturing point of view, but it provides a better performance than the smooth solid rotor. Another HS machine rotor construction is the squirrel cage solid rotor. A rotor of this kind has even better electromagnetic performance. The rotor slip-dependent losses are lower because of the low slip. Further, the power factor of the machines with the squirrel cage solid rotor is higher compared with the other solid rotor solutions (Pyrhönen et al., 2008b; Huppunen, 2004).

The industrial mining of rare-earth elements and a variety of inventions related to the permanent magnet (PM) production have enabled the application of permanent magnets in electrical machines (Morimoto et al., 2014). In the HS machinery, owing to their characteristics, NdFeB and SmCo magnets are the primary alternatives. The key qualities of these PMs are the high remanent flux density and high temperature tolerance, which are important factors in the HS PMSM design.

Similarly to the conventional electrical machines, HS PMSMs have a higher efficiency and a better power factor than HS IMs (Arkkio et al., 2005; Kolondzovski et al., 2011). The frequency converter design is simpler for the HS PMSM because no magnetizing power is needed to be fed through the converter. The rotor design requires high accuracy, and manufacturing has to be performed with adequate tolerances to ensure proper operation. Special attention must be paid to the rotor losses because they can lead to irreversible demagnetization of the magnets.

1.2 Special high-speed PMSM topology

Permanent magnet synchronous machine is a popular machine type in high-speed applications. These machines can have a very high power density, which is especially appreciated if the physical size is a limiting factor. Moreover, high-power HS PMSMs can provide significant energy savings thanks to their high efficiency, which in some cases can reach 98 %. Nevertheless, typical HS PMSM topologies may suffer from some problems.

Permanent magnet synchronous machines for high-speed applications usually have a rotor-surface-magnet rotor. To keep the magnets in their place at high rotational speeds, a retaining sleeve is installed around the magnets (Borisavljevic et al., 2010; Li et el., 2014a). A construction of this kind leads to a complicated manufacturing process.

To limit the operating frequency and to reduce the iron losses in the HS electrical machines, the number of poles is selected as low as possible. In the case of a two-pole machine with distributed windings (DW), the axial protrusion length of the end winding can be equal to the machine active length. This situation is clearly seen in Figure 1.1 with the example of the 2-pole HS IM.

The end winding axial protrusion can increase the total rotor length by 50% in some cases because of the longer shaft as it was shown in Publication I. This lowers the rotor natural frequencies, and in undercritical applications, limits the maximum rotational speed.

The special HS PMSM topology discussed in this work minimizes the problems related to the distributed windings. Simultaneously, the objective of the proposed technology is to reduce the manufacturing costs and simplify the assembly process.

The topology under investigation is a 2-pole, 6-slot HS PMSM with tooth-coil (TC) windings. The rotor is made of a solid cylindrical diametrically magnetized permanent magnet and a retaining sleeve around it. The stator has six slots, and contrary to distributed winding two-pole stators, can be made segmented. The machine uses tooth-coil, that is, nonoverlapping concentrated windings, which significantly help in reducing the total axial length of the machine.

Figure 1.3 illustrates the cross-sectional area of an HS PMSM. The left-hand part shows a typical magnetic flux density distribution in the machine. Some saturation can be seen at the stator tooth tips. The right-hand part shows the flux lines of this 2-pole machine at a nominal load. The two-layer winding arrangement and coil shapes are also shown in this figure.

A diametrically magnetized cylindrical magnet is located in the center. There is no shaft inside the magnet, and therefore, the torque is transmitted through the retaining sleeve. The retaining sleeve around the PM is made of nonmagnetic material, and its permeability is similar to the air, but it allows eddy currents in this case because it is metallic.

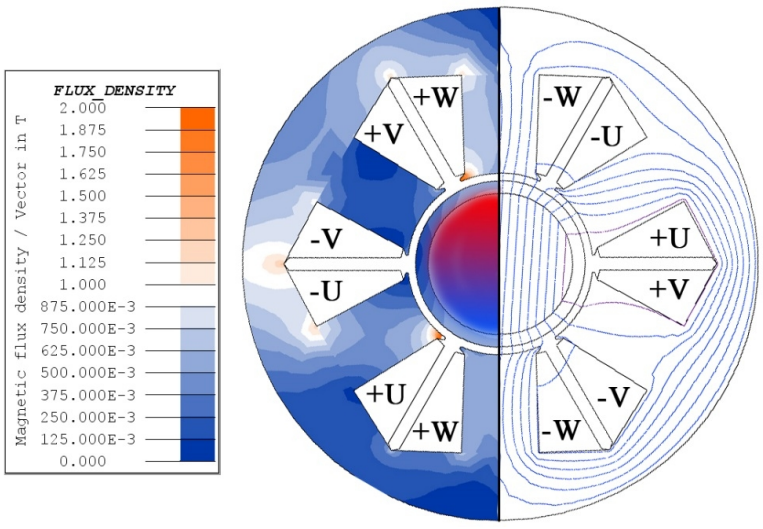

Figure 1.3 Cross-section of the HS PMSM with two poles and six stator slots. The flux density distribution and PM magnetization are shown on the left and the flux lines on the right

Figure 1.4 shows the stator prototype with the studied topology. The machine is designed as an HS permanent magnet synchronous generator (PMSG) with the rated operating point at 31 200 rpm producing 11 kW of electric energy. The generator is used to generate electricity as a part of a micro-Organic Rankine Cycle (ORC) power plant.

The machine is installed on the same shaft with the turbine. This placement allows using the working fluid as a direct cooling for the generator.

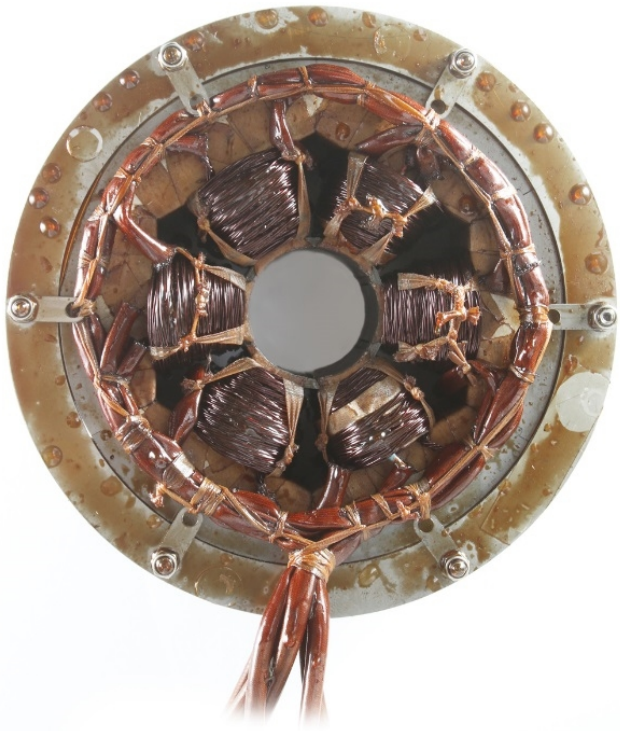

Figure 1.4 Photo of the 11 kW, 31 200 rpm HS PMSM stator having six slots and tooth coils

The detailed analysis of the presented HS PMSM topology in this work includes the design procedure, geometry, materials, loss minimization techniques, magnet demagnetization risk analysis, power and speed limitations, and prototype measurement results.

Table 1.1 lists the HS electrical machines to whose design process the author has contributed. The status of the prototypes is also given. The dissertation concentrates mostly on the results already published of the two-pole HS PMSM topology with tooth-coil windings.

Table 1.1 Designed HS electrical machines in the course of the doctoral studies

Power, kW	Speed, rpm	Type	Prototype Status
11	31 200	2-pole, 6-slot HS PMSM with tooth-coil windings	Built and tested
10	30 000	HS IM with a slitted solid rotor	Built and tested
350	15 000	HS IM with a slitted solid rotor and copper end rings	Built
250	33 000	HS PMSM with rotor-surface-mounted magnets	Built
1000	12 500	HS IM with a squirrel cage	Under construction

1.3 Material selection in high-speed electrical machines

In high-speed machines, the requirements for the materials are higher than for conventional electrical machines. This is mainly due to two key factors. The first one is the different extra losses resulting from the high nominal frequency. Therefore, the materials with low per unit loss values are usually selected in the HS machinery (Gonzalez & Saban, 2014; Etemadrezaei et al., 2012). The second factor is due to the high rotational and peripheral speeds. These set stringent requirements for the mechanical rigidity of the rotor (Li et al., 2014a; Li et al., 2014b).

The temperatures and thermal limitations are very important in high-speed electrical machines. Because of the fact that the same amount of losses is produced in a smaller volume, the cooling of the HS machines is more complicated. All these factors are acting simultaneously, and all the materials must be selected accordingly.

The stator lamination per-unit losses are very important for the high-speed machines. For the rotor retaining sleeve material, the conductivity, yield strength, and thermal conductivity are of a high importance (Zhang et al., 2015).

In the HS PMSM, the permanent magnet selection is critical because it defines the machine performance. Moreover, the high magnet temperature together with the high demagnetization field can cause irreversible magnet demagnetization. It will require rotor disassembly and PM replacement, which cause significant extra costs.

An example of an HS PMSM rotor structure is shown in Figure 1.5. In the center of the rotor there is a ferromagnetic yoke with cooling channels right below the permanent

magnets. The magnets are divided into segments both axially and radially to reduce the Joule losses caused by eddy currents. The retaining sleeve is installed around the magnets, ensuring rotor rigidity at high speeds.

This rotor structure is applied in a 250 kW HS PMSG to whose design process the author has contributed. The selection of the high-speed technology with permanent magnets was one of the factors that enabled the simulated high total system efficiency (Malkamäki et al., 2015).

Figure 1.5 Rotor model of the rotor-surface-magnet HS PMSM. Slots under the magnets are used for the rotor cooling

One of the key advantages of the HS machines is the option to provide a direct connection between the prime mover and the acting tool. This simplifies and lightens the construction by eliminating the need for a gearbox. Simultaneously, the total system efficiency is clearly increased. In some cases, the actuator is acting in a harsh environment, and therefore, the electrical machine must tolerate the same environment.

The electrical machine design is part of a project, the objective of which was to design and manufacture an integrated hermetic turbogenerator. The HS IM capable of producing 500 kW–1 MW of electricity was selected for the project. The electrical machine is positioned on the same shaft with the turbine, and therefore, there is a steam leakage from the turbine to the HS IM. The slightly superheated steam with a high temperature and about one bar absolute pressure is passing through the air gap of the HS IM. This means that all the materials employed in the machine must tolerate the steam atmosphere over the machine lifetime.

Aging tests in a steam atmosphere were performed to ensure the safe operation of all HS IM components. A number of analyses before and after the aging tests were made to select

the best suitable materials. A special equipment and test procedures aimed to perform aging tests in a steam atmosphere were designed and built. The harsh environment sets extra limitations on the HS machine materials (Sihvo et al., 2007).

1.4 Outline of the doctoral dissertation

The doctoral dissertation reports on the research and development work carried out from 2012 to 2016 to identify and solve problems in different high-speed electrical machines. The main objectives include the opportunity recognition for the implementation of HS machinery in different fields of industry, and selection of the suitable machine topology, design, analysis, and optimization of the HS machines.

This work focuses on two specific questions. The first one is a detailed study of the special HS PMSM topology having two poles, six slots, and tooth-coil windings. The analysis of this topology covers the design topology, geometry, loss minimization, magnet demagnetization risk, limitations, prototype measurements, and several types of comparisons.

The second topic is the materials employed in the HS machines. It includes an analysis of the HS IM operating in a harsh environment and the behavior of the selected materials. Considerations of the material selection for lamination, rotor retaining sleeve, permanent magnet, and magnetic wedges are presented in this work. The hysteresis loss phenomenon in permanent magnets and its risk in the HS machines are also studied.

The areas of research include electromagnetic design and performance analysis, thermal design and limitations, mechanical behavior, material science, and systematic design of the HS machine.

Publication I introduces a special HS PMSM topology having two poles and six stator slots with tooth-coil windings and describes the key advantages of this solution. The paper investigates all machine losses. Methods to reduce stator, rotor, and PM losses are proposed. The machine working temperature and the risks of the PM demagnetization in normal working conditions and in cases of two- and three-phase short circuits are studied. The publication was a joint effort of researchers from LUT and Moscow Power Engineering Institute, Russia. Mr. Uzhegov was the principal author and investigator in this paper. Prof. Pyrhönen supervised the project. Dr. Shirinskii and Prof. Pyrhönen were responsible for the revision of the paper.

Publication II describes the mechanical and electromagnetic limitations of the topology under study. The equations for the maximum rotor diameter, sleeve thickness, and dynamical interference fit between the retaining sleeve and the permanent magnet are given. The introduction of the rotor dynamical behavior and critical rotor speeds are presented. This paper investigates the influence of the magnetic wedges on the rotor losses in the proposed HS PMSM. Mr. Uzhegov was the principal author and investigator in this paper. Dr. Kurvinen performed the mechanical modeling and analysis. He was also

in charge of the description of the mechanical limitations including the rotordynamics and structural analysis. Prof. Pyrhönen was responsible for the supervision of the project and the revision of the paper.

Publication III investigates the advantages and drawbacks of the proposed HS PMSM topology. The analysis is based on two machines having 3.5 kW and 11 kW output power. The similarities and differences of these machines are discussed. The test setup and some prototype measurements are presented. Mr. Uzhegov was the principal author and investigator in the paper. Dr. Nerg was responsible for the 3.5 kW HS PMSM design and all the measurements. Prof. Pyrhönen was in charge of the supervision of the project and the revision of the paper.

Publication IV provides a detailed comparison of the distributed and tooth-coil windings in the HS topology under study. A detailed loss distribution analysis and the reasons for the extra copper losses are shown. Mr. Uzhegov was the principal author and investigator in the paper. Dr. Nerg was responsible for the analysis of the 3.5 kW HS PMSM and all the measurements. Prof. Pyrhönen was in charge of the supervision of the project and the revision of the paper.

Publication V describes the HS electrical machine design flow divided into steps with an emphasis on the electromagnetic, mechanical, and thermal analyses. The features of every step are discussed, and the prerequisites to move to the next steps are given. The design flow is tested with two HS PMSM prototypes having the studied topology. The measurement results, which include an efficiency map, have a very good agreement with the results calculated using the presented design methodology. The paper is a joint effort of LUT Electrical Engineering, LUT Mechanical Engineering, and Moscow Power Engineering Institute. Mr. Uzhegov was the principal author and investigator in the paper. He was responsible for the electromagnetic analysis and case studies. Dr. Kurvinen provided the initial design flow idea. He was also responsible for the mechanical analysis including the rotordynamics and incorporation of these steps into the design flow. Dr. Nerg performed the thermal design and prototype measurements. Prof. Sopanen, Prof. Pyrhönen and Dr. Shirinskii were responsible for the revision of the paper. Dr. Nerg, Prof. Sopanen, and Prof. Pyrhönen supervised the project.

Publication VI investigates the materials for the magnetic wedges, which are suitable for the operation in a steam atmosphere. In this paper, the simulations confirm the important role of the magnetic wedges in the HS IM. Aging tests of different magnetic wedges were designed and performed. A number of analyses before and after the test were conducted to select the best suitable steam-resistant magnetic wedge. The paper is a joint effort of LUT Electrical Engineering and LUT Chemical Engineering. Mr. Uzhegov was the principal author and investigator in this paper. He was responsible for the measurement design and analysis. Dr. Pihlajamäki carried out the Fourier Transform Infrared Analysis (FTIR). Dr. Nerg has largely been responsible for the test installation setup. Dr. Nerg and Prof. Pyrhönen supervised the project.

Publication VII introduces the possibility of hysteresis losses in sintered NdFeB permanent magnets. In the paper, the theoretical background, hysteresis measurements, and the possibility of hysteresis losses in sintered NdFeB PM in HS rotating electrical machines are investigated. Prof. Pyrhönen was the main author of the paper, Dr. Ruoho, Dr. Nerg, and Prof. Boglietti contributed to the understanding of the PM hysteresis theory, Mr. Paju, Mr. Tuominen, and Mr. Kankaanpää were responsible for the PM measurements in Pori, and Dr. Stern in Tallinn. Mr. Uzhegov made the finite element method (FEM) analysis of the HS surface-mounted PMSM, which clearly demonstrated the possibility of hysteresis losses in sintered NdFeB PM in HS electrical machines.

This introductory Chapter 1 provides the background and motivation for this study. The benefits and applications of the high-speed electrical machines are presented. Chapter 2 is based on Publications I–V. It shows the advantages of the HS PMSMs with an emphasis on a special topology. Chapter 3 is based on Publications VI–VII. It analyzes the materials used in HS electrical machines. The HS machines in a harsh environment and the risk of hysteresis losses in sintered NdFeB permanent magnets are shown. Chapter 4 concludes the doctoral dissertation and provides ideas for future work.

1.5 Scientific contributions

This doctoral dissertation analyzes implementation of the high-speed electrical machines in different industries and applications. The technical and economic advantages of the HS machines for several applications are analyzed. The work provides solutions to a number of problems related to the HS machine design, topology selection, and implemented materials. These include, for instance, combining the analysis from several fields into a multidisciplinary design flow, loss minimization in the 2-pole, 6-slot HS PMSM with tooth-coil windings, and selection of the magnetic wedge coating for a harsh environment.

The design process of HS electrical machines is a highly multidisciplinary task. It involves knowledge of electromagnetics, thermal engineering, static structural and dynamic mechanics, and material science. In this work, each of these key HS machine design aspects are addressed. The findings are supported by prototype measurements and material behavior tests.

The main scientific contributions of this dissertation can be divided into four groups:

- A multidisciplinary design flow for the HS PMSM is introduced in this work. It includes rotor structural, electromagnetic, rotordynamics, thermal designs, manufacturing, and assembling. The existing publications on the multidisciplinary design of the high-speed machines did not include one or several above-mentioned design stages or concentrated on different machine topologies. The proposed design flow provides a straightforward path to design high-speed electrical machines. The design process involves engineers from different fields. It divides the responsibilities of every involved party and defines the criteria to

move to the next step. The design flow provides the options and design solutions if the next step criteria are not met. The implementation of the proposed multidisciplinary design flow can significantly cut the HS electrical machine design time, and reduce the number of errors and related costs.

- The work shows the detailed analysis of a special HS PMSM topology. To the author's knowledge, the PMSM topology with two poles, six slots, and tooth-coil windings has seldom been used in high-speed applications, and the constructed prototypes have lower output power. The advantages of the topology for the HS machinery are elaborated on. The topology is investigated from electromagnetic, mechanical, and thermal points of view. The results of the analytical and numerical calculations are confirmed by prototype measurements. The topology is suitable for a variety of low-power high-speed applications. Its performance limits are demonstrated in the work, in other words, the application field of the machine type is scientifically determined.
- The investigation of the magnetic wedge materials and their covers for a harsh environment is presented in this dissertation. The motivation for this work was the lack of an information about the ability of the magnetic wedges to tolerate a harsh environment. The methods and analyses used in the study are shown. The results demonstrate the suitability of some of the studied materials for operation in the steam atmosphere and underline the best option among the samples under study.
- The dissertation evaluates the risk of hysteresis losses in sintered NdFeB permanent magnets in high-speed electrical machines. This topic has not been studied before in the context of the high-speed electrical machines. A FEM study illustrates the conditions that can lead to these extra losses in the rotor. These losses can cause the PM irreversible demagnetization and must be avoided at the design stage of the electrical machine.

2 Special high-speed PMSM topology

The design process of any electrical machine is a multidisciplinary task. In the case of a high-speed machine, the multidisciplinary nature of the design process is of even higher importance. In addition to the electromagnetic design, mechanical and thermal calculations are involved in the design process. The design process is further complicated by a need to take into account phenomena from different scientific fields during the HS machine design. This fact is confirmed by the continuous research regarding different aspects of HS electrical machines in academia all over the world (Bárta & Ondrůšek, 2016; van der Geest et al., 2014; Pyrhönen et al., 2010; Jang et al., 2007; Bianchi et al., 2003).

High-speed electrical machines with permanent magnets require appropriate design to avoid critical failures during the operation. This is due to the nature of the SmCo and NdFeB permanent magnets. They are brittle, and therefore, precise mechanical calculations have to be made to avoid crumble. Joule losses caused by eddy currents occur in these magnets because of the significant conductivity. This leads to a temperature increase, which, together with the magnetic field, can cause the PM demagnetization. To avoid the risk of demagnetization, electromagnetic and thermal calculations of the PM rotor have to be performed together. In addition, the magnet remanence decreases with the higher temperatures, which can affect the machine performance and must be taken into account at the early design stage.

Figure 2.1 illustrates a cross-section of the topology under investigation. In the rotor part, a full cylindrical permanent magnet has two poles. It is magnetized diametrically and the poles are shown in red and blue colors. A retaining sleeve around the magnet is shown in light green. The construction and thickness of the retaining sleeve are one of the key design components because thermal, electromagnetic, and mechanical limitations are applied to this part.

Stator winding phases are shown in red, green, and blue colors. The opposing coils belong to the same phase, and because of the 2-pole structure, they produce flux in the same direction. In this figure, the tooth-coil windings are made prewound to simplify the manufacturing process; however, this leads to a poor copper space factor.

There are magnetic wedges between the stator tooth tips, which are shown in yellow. These wedges are a very important component in this topology because they can significantly improve the electromagnetic performance.

In this chapter, the detailed analysis of the proposed topology is presented from different points of view.

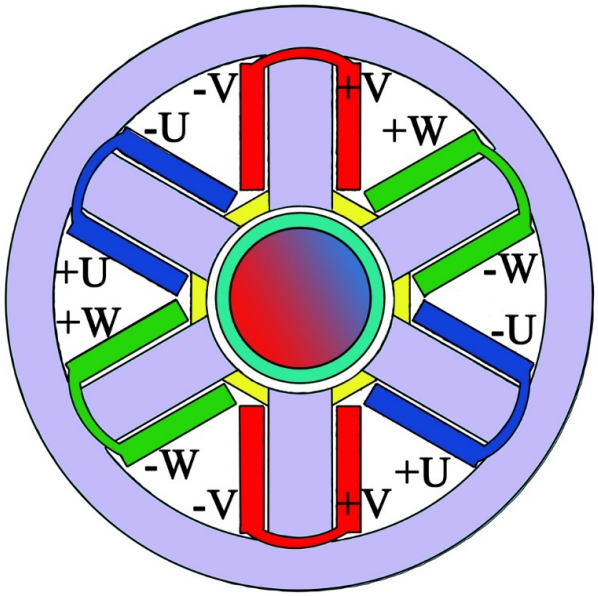

Figure 2.1 Cross-section of the 2-pole, 6-slot HS PMSM with tooth-coil windings

2.1 Design process

The design of a conventional electrical machine is defined mostly by the electromagnetic calculations. In the case of a high-speed machine there are always limitations from the mechanical and thermal parts. Because of these limitations, there is a narrow window for the electromagnetic design. The task of the HS machine designer is not only to find the best solution from the electromagnetic point of view, but also to reach a compromise with designers from the other fields and to come up with a feasible solution.

Figure 2.2 shows a design flowchart, which was specially developed for the HS PMSM topology under investigation. It consists of nine steps, conditions that have to be met in order to move to the next step, and suggestions for the designer if these conditions are not met.

First, a requirement list is defined and a feasibility study is conducted to verify the initial design. For this task, a simple analytical model is suitable. If even the first feasible design cannot be found, some changes in the requirements may be considered.

The actual design starts with the study of the rotor mechanical limitations. At this step, the rotor materials are preliminarily defined, or a couple of material options are analyzed. The analytical expressions presented in Publication V are used to find the limiting rotor size. The actual electromagnetic design starts with analytical calculations, followed by the FEM analysis. At this stage, also the initial cooling solution is selected. After that, the parameters of the machine are transferred to the next step for the initial rotordynamics

analysis. The sixth step is the selection or design of the bearings, for instance, in the case of active magnetic bearings. Then, the casing design must be performed to verify the dimensions of the system.

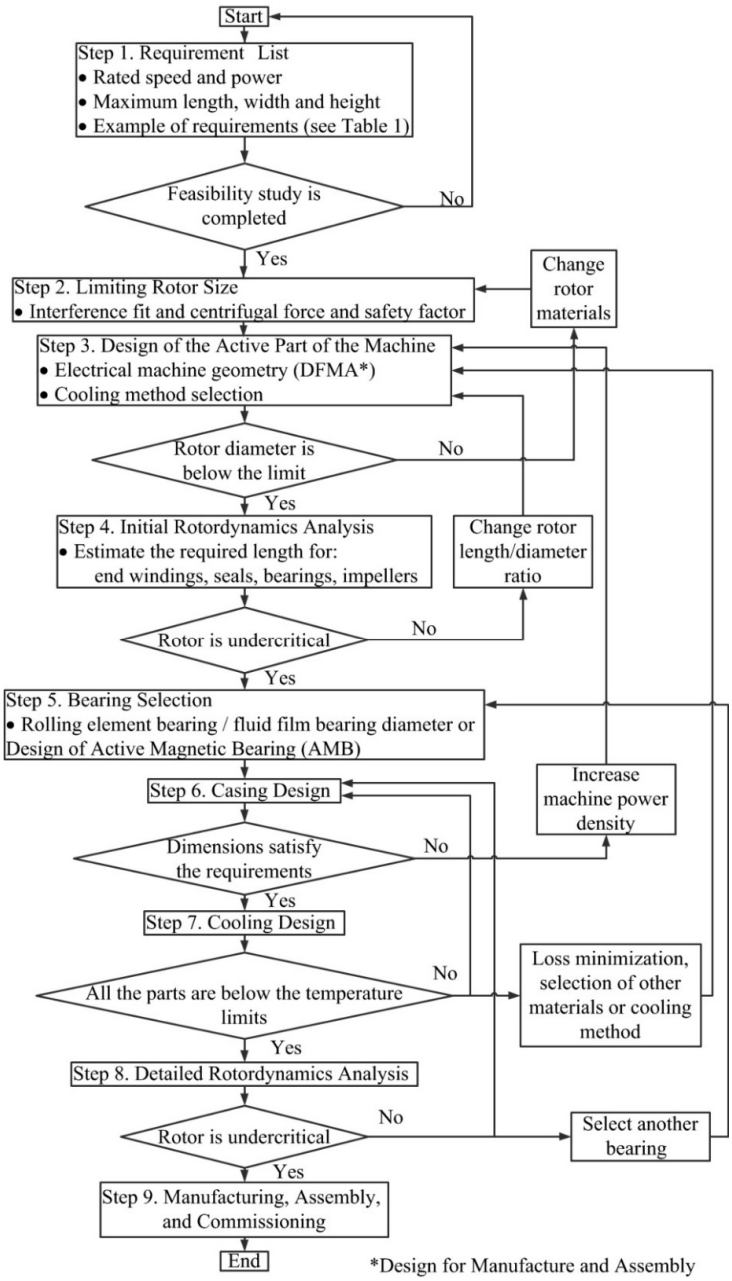

Figure 2.2 Flowchart of the high-speed PMSM design

The data for the cooling design are collected from the previous step and from the electromagnetic design. Thermal analysis is performed applying lumped-parameter-based model. If the thermal limitations are met, a detailed rotordynamics analysis is performed using analytical toolbox in Matlab® (MathWorks, 2016). In the final step, the manufacturing drawings are prepared, and the machine is assembled and commissioned. After that, different test procedures can be conducted in order to verify the design assumptions.

This design flowchart was proposed for the HS electrical machine topology under investigation; however, with slight modifications, it is applicable to any HS machine. The detailed description of every step can be found in Publication V. This dissertation work concentrates mostly on step 3, which deals with the electromagnetic design of the HS PMSM.

Numerical electromagnetic analysis was performed using the FLUX 2D commercial FEM software (Cedrat, 2016). The results were obtained using two-dimensional, transient analysis with sinusoidal voltage sources.

2.2 Geometry

The cross-sections of the different HS PMSMs with the proposed topology are illustrated in Figure 1.3 and Figure 2.1. A 3D model of the designed 6-slot, 2-pole electrical machine is shown in Figure 2.3. The geometry features of this machine follow the key design ideas and are aimed to find a compromise between mechanical, thermal, and electromagnetic requirements.

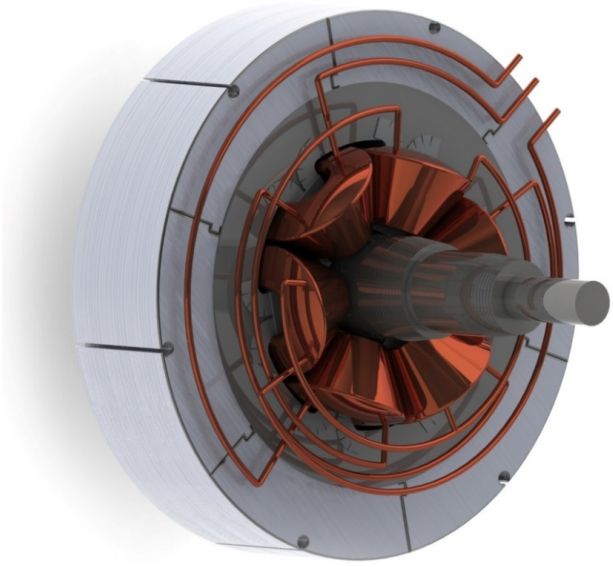

Figure 2.3 3D model of the HS PMSM having six slots and two poles

The geometry configuration of the HS PMSM under consideration is made to satisfy the following requirements:

- simple and cost-effective manufacture,
- short total axial length, and
- low electromagnetic losses.

In this machine there are only six slots to minimize the work required for the stator manufacture. Tooth-coil windings allow two possible ways of cost-effective manufacturing. In the first case, the coils are prewound and placed above the insulated stator teeth in the machine assembly process. This option is illustrated in Figure 2.1. It must be noted that the copper space factor is very low in this case. The machine must be always made open-slot to enable coil assembly.

The second option of the cost-effective winding manufacture is shown in Figure 1.3 and Figure 2.3. The stator is made of six separate segments, which are then assembled together. Each segment is prewound before the assembly, which enables a very high copper space factor and allows modifying the stator tooth tip geometry and making semi-closed slots. The segmented stator structure reduces the material loss in the laser cutting. From one single lamination sheet, more useful stator lamination can be produced and less material is discarded. One prewound segment is shown in Figure 2.4. Both winding manufacturing options reduce manufacturing costs in serial production.

Figure 2.4 Photo of the prewound segment for the 6-slot stator

A short total axial length is important from the rotordynamics point of view. A shorter rotor enables higher critical frequencies, which, in turn, allow higher rotational speeds in undercritical operation. An overcritical system is also possible; however, it introduces a number of difficulties to be solved for a stable operation.

To reduce losses in the electrical machine and in the frequency converter, a low number of poles is selected in high-speed applications. In the case of a 2-pole machine with distributed windings, the protrusion length of the end windings can be equal or even more than the active stator length. This leads to a longer rotor and sets an extra limitation from the rotordynamics.

A comparison of the total axial machine length in the case of distributed and tooth-coil windings is provided in Publication I. It also can be seen in Figure 1.1 that the protrusion length of the distributed windings is significant. In contrast, Figure 2.4 shows that the tooth-coil windings do not increase the machine total length almost at all.

The geometry considerations that enable loss minimization include the stator yoke thickness, the air gap length, and optimization of the tooth tips and wedge geometries. A detailed discussion of these aspects is given in the following section.

2.3 Losses and loss minimization

A high power density and a high nominal frequency in high-speed electrical machines cause extra losses in the small machine volume. This fact leads not only to a poor electromagnetic performance, but the losses may even cause machine breakdown. Two most critical areas in the topology under study are the permanent magnet and the stator end windings.

A high end winding temperature is a common problem in many rotating electrical machines (Boglietti et al., 2009). In the topology under investigation, the end winding temperature is less critical because in the case of forced air cooling, the heat is dissipated directly from the winding surface. There are also cooling air passages between the coils.

A comparison of the distributed and tooth-coil windings in high-speed machines is given in Publication IV and in (Merdzan et al., 2015). The winding factor in the case of a 6-slot, 2-pole machine with tooth-coil windings is only 0.5 (El-Refaie, 2010; Magnussen et al., 2007). However, the end windings are significantly shorter in this topology. For the comparative analysis, a machine with distributed windings and the same power, speed, and current density was designed. It has 12 slots, 2 poles, and double-layer windings with short pitching equal to 5/6. The copper loss level was about 100% higher in the case of the tooth-coil machine because of the lower winding factor. Copper losses in 12-slot, 2-pole machine with distributed windings were 44 W in the nominal operating point, and copper losses in 6-slot, 2-pole machine with tooth-coil windings were 88 W in the nominal operating point.

This problem could be partly solved by changing over to a 3-slot, 2-pole design, which has a high fundamental winding factor. However, a 3-slot machine produces significantly higher rotor eddy current losses compared with the 6-slot topology because of the air gap spatial harmonics. According to (Noguchi & Kano, 2007a; Noguchi et al., 2007b), the total losses can be 130% higher in a 3-slot, 2-pole machine compared with a 6-slot, 2-pole machine. In addition, there is always a high unbalanced magnetic pull (UMP) in a 3-slot configuration. It is caused by the odd space harmonics of the radial forces, particularly by the fundamental harmonic (Lim et al., 2015; Zhu et al., 2007). These radial forces significantly reduce the lifetime of traditional bearings. Therefore, in spite of the lower copper losses and a more simple construction, a 3-slot, 2-pole machine has high rotor losses and a high UMP, which are critical drawbacks.

Extra copper losses may occur at high frequencies for numerous reasons. These extra losses have to be minimized as they can significantly raise the winding temperature (Gonzalez & Saban, 2014). First, skin effect in the conductors must be avoided (Sullivan, 1999). For this reason, in the designed machines, each conductor was divided into several wires with a diameter less than the penetration depth at the operating frequency.

Several parallel wires together with, for example, rotating magnetic field produced by the permanent magnet may cause circulating currents, which increase copper losses. An effective way to reduce these losses is the use of Litz wires (Hämäläinen et al., 2014; Wojda & Kazimierczuk, 2012). However, this solution is quite expensive in small machines, and one of the objectives of the topology under study is cost minimization. Therefore, several parallel wires were twisted with some 360-degree twists per stator stack length. This solution provides results similar to the Litz wires but at lower production costs (van der Geest et al., 2014). One stator segment with the proposed windings is shown in Figure 2.4.

Magnetic wedges between the tooth tips enable different aspects of loss minimization including the winding shielding from the rotating field produced by the PM. This shielding reduces the extra eddy currents in the conductors and reduces the copper extra losses. The other loss minimization effects obtained by the magnetic wedges are discussed further in this section.

The comparison of the distributed and tooth-coil windings is not limited to the copper losses only. The air gap flux density and its harmonic contents are different in these types of windings. Figure 2.5 illustrates these parameters in the designed HS PMSM with distributed windings.

Figure 2.6 shows the normal component of the flux density in the middle of the air gap and its per unit harmonic contents for the studied 6-slot, 2-pole machine with tooth-coil windings. Both machines were simulated using the FEM and, the results were obtained in the nominal point.

In the case of the DW machine, the 11th and 13th harmonics are dominant, and for the machine with TC windings, the 5th and 7th are the highest. The number of stator slots, which is 12 in the DW case and 6 in the TC winding case, is the key reason for this kind of a distribution.

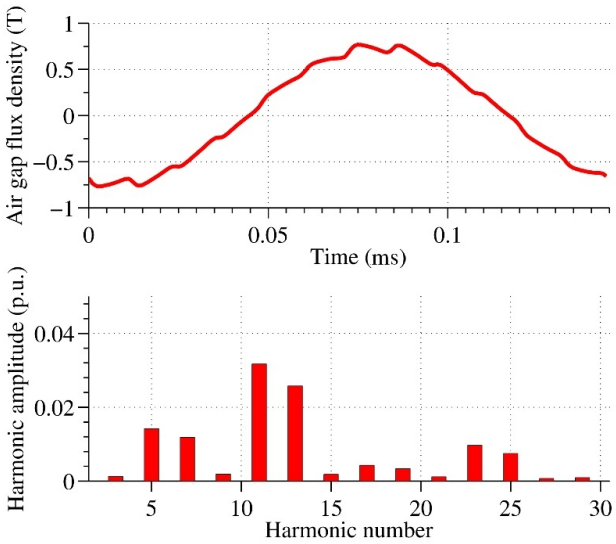

Figure 2.5 Normal component of the flux density in the middle of the air gap and its per unit harmonic contents in a 12-slot HS PMSM with distributed windings. The amplitude value of the fundamental component is 0.74 T

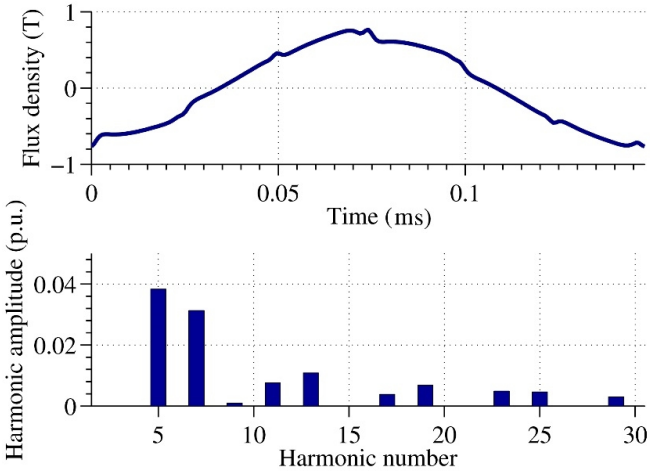

Figure 2.6 Normal component of the flux density in the middle of the air gap and its per unit harmonic contents in a 6-slot HS PMSM with tooth-coil windings. The amplitude value of the fundamental component is 0.76 T

These harmonic contents are the main reasons for the rotor losses, which consist of the PM losses and the retaining sleeve losses. The 5^{th} and 7^{th} harmonics cause more losses than the 11^{th} and 13^{th} ones because of their lower number in the case of the same amplitude. Moreover, the total harmonic distortion (THD) is higher in the case of the tooth-coil windings. Thus, the total rotor losses are 45 W in the case of the TC winding machine and 18 W in the case of the DW machine. The nominal power of both machines is 11 kW at 31 200 rpm.

If there is no limitation on the machine outer diameter, the yoke thickness can be optimized to minimize the total core losses. According to the different models of core losses, an increase in the flux density leads to a significant increase in the total core losses in high-speed electrical machines (Choi et al., 2013). Therefore, it is possible to increase the yoke thickness, which, in turn, decreases the yoke flux density. The lower yoke flux density provides lower per unit core losses. On the other hand, an increase in the stator outer diameter also increases the stator yoke volume, which leads to higher material consumption. Finally, it is possible to find an optimum outer diameter with which the yoke core losses can be minimized keeping a reasonable amount of lamination applied.

Figure 2.7 shows the total stator core losses and their components at different stator outer diameters. The results were produced by the FEM in the nominal operating point. The value of the stator teeth losses remains almost unchanged with an increase in the stator outer diameter. The yoke core losses decrease with an increase in the stator diameter, which causes a decrease in the total stator core losses. The optimum value of the stator outer diameter in the designed 11 kW, 6-slot, 2-pole HS PMSM is 242 mm.

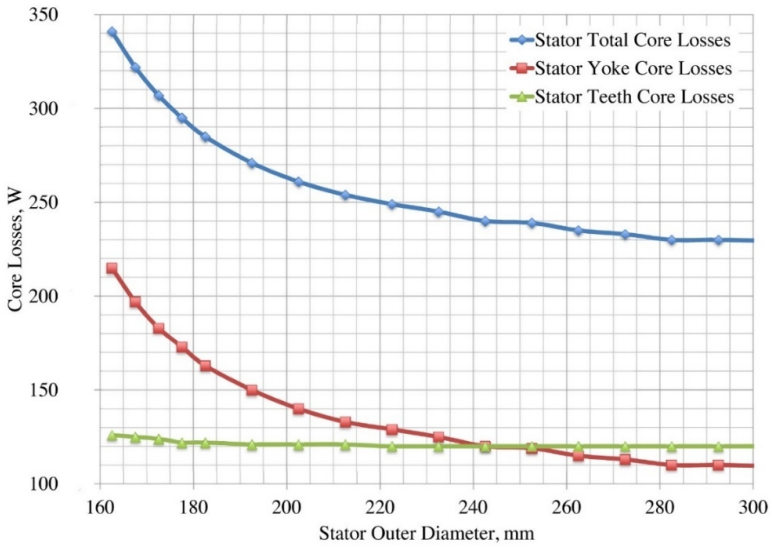

Figure 2.7 Stator core loss distribution with different stator outer diameters

At this diameter value, the teeth core losses are equal to the yoke core losses. A further increase in the stator outer diameter does not significantly decrease the total core losses but leads to inefficient lamination material usage.

In the topology under investigation, the rotor PM temperature is one of the most critical parameters. To reduce this value, some rotor loss minimization solutions must be implemented. One of the ways to reduce rotor losses in the FEM design stage is the adjustment of the air gap length. An increase in the physical air gap enables filtering of the high-order harmonics and reduces the Joule losses caused by eddy currents in the retaining sleeve and in the magnet (Liu, 2010). However, an increase in the air gap length negatively affects the PMSM performance and a change only below 20% is allowed.

The next solution for the rotor loss minimization is the optimization of the stator tooth tip zone. It includes geometry modification of the tooth tips in order to reduce the air gap harmonics resulting from the slotting. In the case of the prefabricated winding solution, shown in Figure 2.1, it is not possible because of the open slot requirement. However, in the case of the segmented structure, tooth tips can be modified to achieve minimum rotor losses. The limiting factor during the optimization process is the increase in the tooth tip flux leakage.

The installation of the magnetic wedges between the tooth tips enables a further reduction of the air gap flux density harmonics and the rotor losses. The influence of the magnetic wedge installation on the reduction of slot opening harmonics is studied in Publication II. Figure 2.8 shows the harmonic content reduction of the air gap flux density normal component in the middle of the air gap resulting from the implementation of the magnetic wedges. The harmonic magnitudes are presented in per unit values for a fair comparison. All the harmonics were calculated by a FEM analysis. The harmonics caused by the slot openings were calculated at no load and at the rated speed without current in the stator.

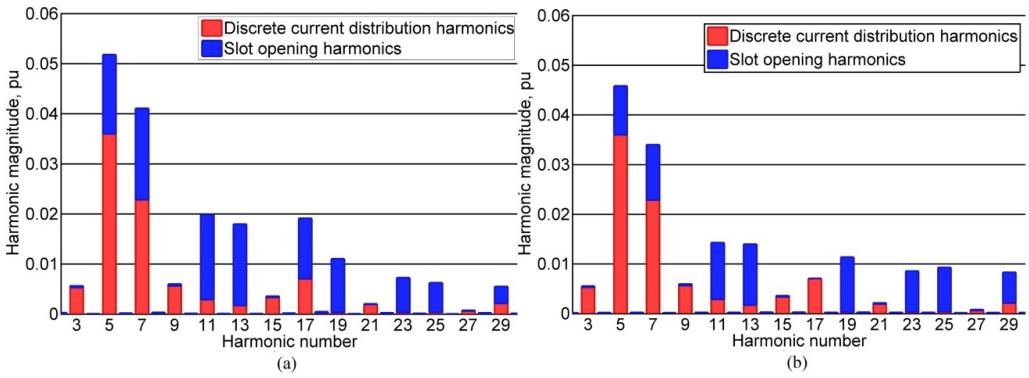

Figure 2.8 Air gap flux density normal component harmonics caused by the discrete current distribution and the slot openings (a) without magnetic wedges (amplitude of the fundamental component is 0.68 T) and (b) with installed magnetic wedges (amplitude of the fundamental component is 0.70 T)

After that, the slot permeance and the current harmonics were separated from each other at the nominal load. The voltage source supply was used for the FEM simulations. The 5^{th}, 7^{th}, 11^{th}, and 13^{th} harmonics caused by the slot openings were reduced. The THD reduction after the magnetic wedge installation is about 25% in the 11 kW, 31 200 rpm HS PMSM with the topology under investigation. This leads to a reduction in the rotor losses both in the retaining sleeve and in the permanent magnet.

The magnetic wedge shape has a major impact on the reduction of slot harmonics. The optimization of the magnetic wedge shape is performed together with the tooth tip optimization. One of the limiting factors is the manufacturability of the proposed wedge shape. Another factor that should be taken into account in the wedge shape optimization is the possible increase in the air gap friction losses.

Publication I describes the effects of the above-mentioned solutions on the HS PMSM rotor loss minimization. The effect of the different optimization options for the 11 kW HS PMSM with the proposed topology is shown in Figure 2.9. The results of the FEM simulation illustrate the losses in the rated operating point in each case. The first option represents the initial machine configuration calculated by analytical tools. To reduce the

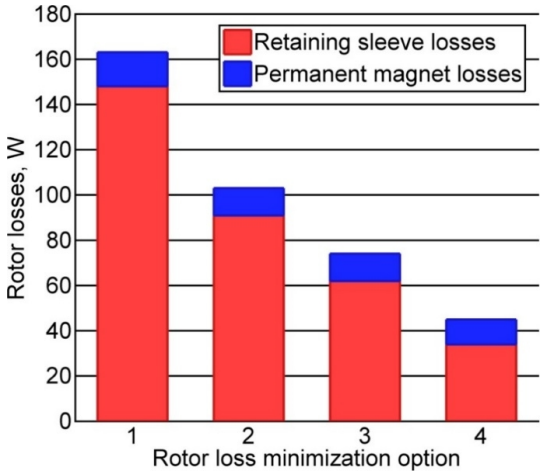

Figure 2.9 Rotor loss minimization options and their effect on the total rotor losses: 1) Physical air gap equal to 2 mm, no wedges, the retaining sleeve thickness is 3 mm; 2) Physical air gap equal to 2 mm, magnetic wedges with a relative permeability of 3, the retaining sleeve thickness is 3 mm; 3) Air gap 2 mm, magnetic wedges with a relative permeability of 3, the retaining sleeve thickness is reduced to 2.5 mm; 4) Air gap is increased to 3.4 mm by increasing the stator inner diameter, magnetic wedges with a relative permeability of 3 and optimized shape, the retaining sleeve thickness is 2.5 mm

rotor losses, several design solutions were implemented. The option number two represents the installation of the magnetic wedges between the tooth tips, and leads to an about 37% reduction in the total rotor losses. The option number three increases the physical air gap by a reduction in the retaining sleeve thickness from 3 to 2.5 mm. Finally, the option number four includes an additional increase in the physical air gap by increasing the stator inner diameter and by wedge shape optimization. The total rotor losses after the proposed optimization steps are only 27% of the initial design rotor losses.

A typical loss distribution in the topology under investigation is illustrated in Figure 2.10. It is possible to design the machine so that the core and copper losses in this HS PMSM are approximately equal. Together, these losses account for about 25 % of the total losses. Further, as it was shown in Figure 2.7, the yoke and teeth core losses are about the same. These two factors are considered the rule of thumb for the optimal loss distribution.

In spite of the significant difference in the copper and rotor losses with the tooth-coil winding configuration, the total losses are only 13% higher for the TC windings compared with the designed DW machine. The TC winding design allows a significantly shorter rotor, and further, this solution shifts the limitations from the rotordynamics to the electromagnetics and heat transfer. Therefore, loss minimization mechanisms are required in the proposed 6-slot, 2-pole HS PMSM with TC windings.

After the rotor loss minimization, the rotor losses account for only 7% of the total losses. The additional losses are calculated as 0.5% of the output power. The mechanical losses are dominant in this kind of an HS PMSM. This is because the bearing losses are included in the calculations. The implementation of AMBs can significantly reduce the proportion of mechanical losses, increase the total system efficiency, and extend the drive system lifetime.

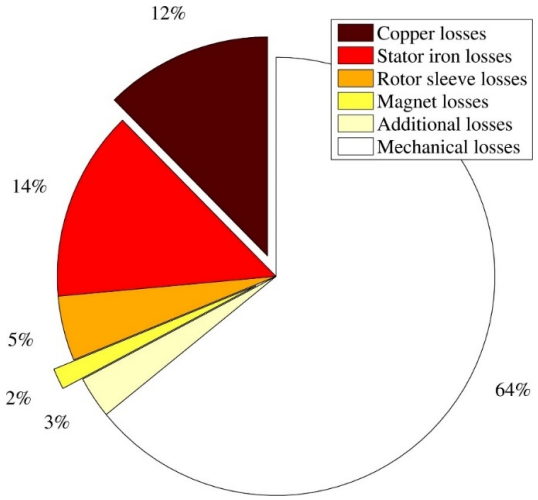

Figure 2.10 Loss distribution in the 11 kW, 31 200 rpm HS PMSM with the proposed topology. The results are obtained by the FEM in the nominal point

2.4 Measurement results

The verification of the analytical and FEM calculations is possible only through measurements. For this purpose, prototypes are required. Following the design flowchart introduced in Figure 2.2, two prototypes were built with the topology under investigation. The first one is a 3.5 kW, 45 000 rpm HS PMSM for a gas blower application. Dr. Nerg made the electromagnetic design of this machine. The machine has open slots, and its cross-section is illustrated in Figure 2.1. It is equipped with active magnetic bearings, which significantly reduce the mechanical losses and increase the total system efficiency (Jastrzebski et al., 2013).

The second prototype is the 11 kW, 31 200 rpm PM generator for a micro-Organic Rankine Cycle (micro-ORC) power plant. The ORC is a Rankine cycle in which the working fluid is an organic fluid (Uusitalo et al., 2014). In this application, the electrical machine is installed on the same shaft with the turbine. Part of the organic fluid is passing through the generator air gap and through the stator slots between the coils. Because of the low temperature, this working fluid ensures cooling of the HS PMSM. Photos of this machine are shown in Figure 1.4 and Figure 2.4. The loss minimization analysis in Section 2.3 is related to this machine.

The key design parameters of the constructed prototypes are listed in Table 2.1. A detailed comparison of these machines is presented in Publication III. Both machines have six stator slots, two poles, and tooth-coil windings. The rotors are made of a full cylindrical magnet and a retaining sleeve around it. SmCo magnets are used in both prototypes to ensure stable operation also at high operating temperatures.

The machines have similar hot areas, which are the permanent magnet and the end windings. To minimize the rotor losses, different approaches are adopted in each case. In the case of the 3.5 kW HS PMSM, more expensive materials are selected to decrease losses. They include titanium for the retaining sleeve and NO10 for the stator stack lamination (Cogent, 2016). For the 11 kW HS PMSM, inexpensive materials with higher per unit losses were chosen. The loss minimization options in this machine are reported in Section 2.3. These options are aimed mostly at the machine geometry optimization.

The use of active magnetic bearings in the 3.5 kW HS PMSM enables equal loss distribution. The loss proportions of the copper, core, rotor, and mechanical losses each account for about 25 % of the total losses. This leads to an optimal loss distribution, less complicated cooling, and reliable operation. In contrast, the use of ball bearings in the 11 kW machine leads to the fact that about two-thirds of the total losses are due to the mechanical losses, as it is shown in Figure 2.10.

Table 2.1 Main parameters of the HS PMSM prototypes

Machine parameter	3.5 kW PMSM	11 kW PMSM
Rated rotational speed n_n, rpm	45 000	31 200
Number of stator slots Q_s	6	6
Number of poles p	2	2
Rated torque T_n, Nm	0.74	3.36
Rotor outer diameter D_r, mm	39	46
Air gap diameter D_δ, mm	43	52
External diameter D_e, mm	140	242
Active length l, mm	22	60
Permanent magnet length l_{PM}, mm	32	70
Permanent magnet remanence B_r, T	1.10	1.12
Stator stack lamination material	NO10	M-270-35A
Retaining sleeve material	Ti-6AL-4V	Stainless steel AISI 316L
Magnetic wedge material	Spindurol™	Magnoval 2067™
Bearing type	AMB	Ball bearing

The measurement setup for the prototypes includes an eddy current brake and a radially flexible mechanical coupling between it and the tested machine. Figure 2.11 shows the test setup, where the eddy current brake is the green device on the right and the 11 kW HS PMSM prototype in a special testing configuration is on the left.

No-load and load tests were performed for this machine. The full load tests were limited to 25 000 rpm owing to the limitation of the eddy current brake bearings. However, the nominal power operating point was achieved by using a higher load torque. The machine was working in the motor mode, and the input power was measured by a power analyzer. The output power was measured by the eddy current brake. The measurement results of the 11 kW HS PMSM provide the efficiency map shown in Figure 2.13. The results above 25 000 rpm were extrapolated from the measured data using gridfit analytical procedures in Matlab® (Mathworks, 2016; Keim & Herrmann, 1998).

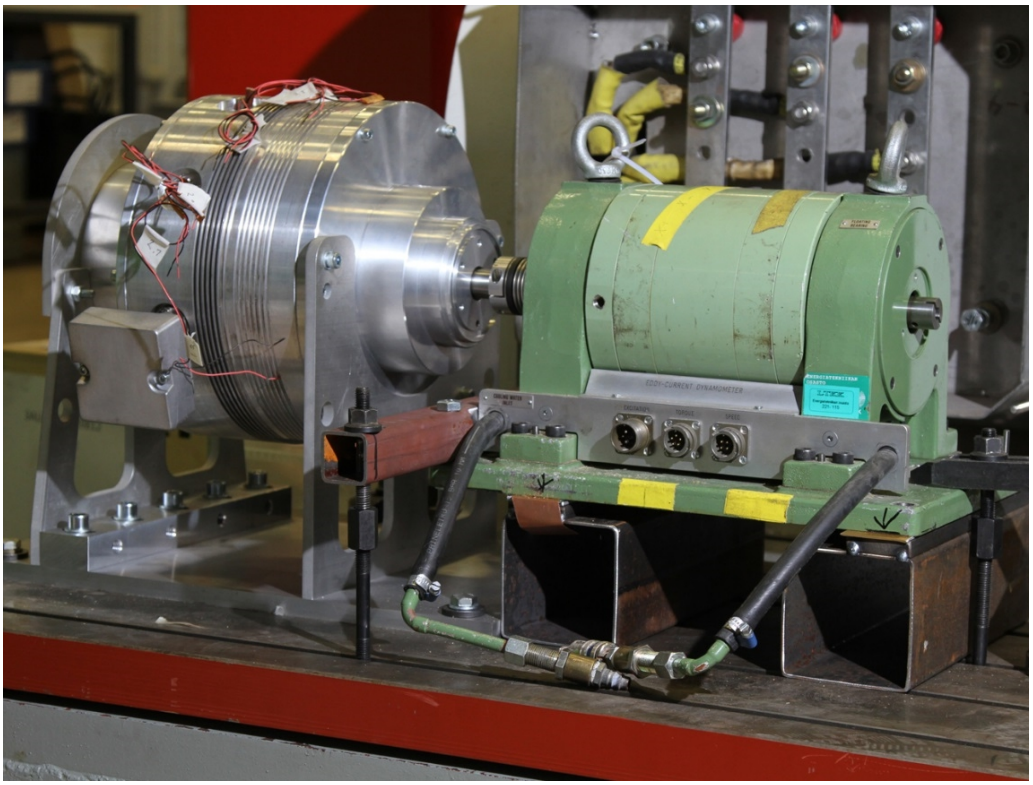

Figure 2.11 Test setup of the 11 kW HS PMSM prototype

The calculated efficiency map for the 11 kW HS PMSM is shown in Figure 2.12. A FEM analysis of about 400 points was performed to achieve a calculated efficiency map. The nominal operating point is indicated by a green circle in both efficiency maps. The measured and calculated results show a good agreement, especially at high rotational speeds. In the nominal operating point, the efficiency difference between the measured and calculated data is below 1%.

These results verify the considerations and assumptions made in the machine design. The topology under investigation with an appropriate design is suitable for low-power, high-speed applications. The benefits of this topology include simple and cost-effective manufacturing process, short total axial length, and lower electromagnetic losses.

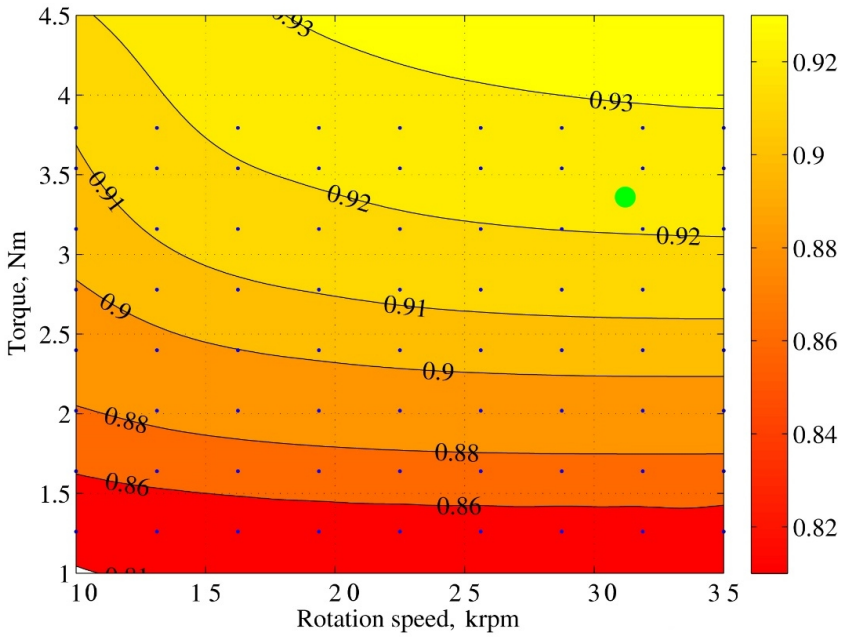

Figure 2.12 Calculated efficiency map of the 11 kW HS PMSM

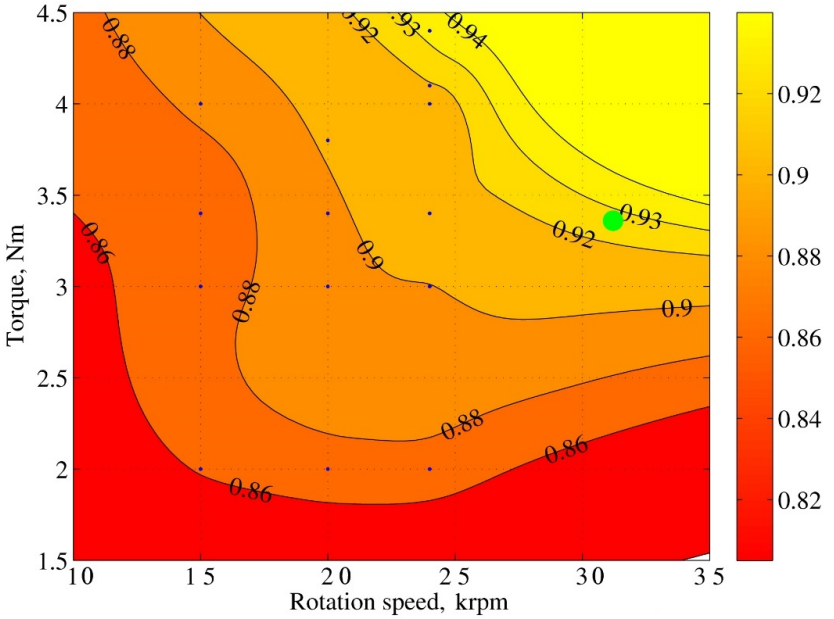

Figure 2.13 Measured efficiency map of the 11 kW HS PMSM. The results above 25 000 rpm were extrapolated from the measured data using analytical procedures

3 Material selection in high-speed electrical machines

The development of electrical machines follows the invention and industrial production of new materials. Compared with previously used materials, new ones may provide a more rigid structure, lower per unit losses, better electromagnetic properties, lower costs, or a combination of these advantages. For example, the invention of the NdFeB magnet manufacturing process has boosted the development of the PMSMs (Morimoto et al., 2014; Petrov & Pyrhönen, 2013; Sagawa et al., 1984).

New materials are usually used in electrical machines to overcome their physical limitations. This is especially important in high-speed machines, because in many cases the performance and the maximum achievable speed or power are limited by the material properties. Moreover, numerous factors such as high mechanical stresses and high temperatures are acting simultaneously on the materials in the high-speed electrical machines.

The design stage of the HS PMSM with the topology under study includes a selection of the stator lamination, rotor retaining sleeve, and permanent magnet materials. In this process, not only the physical properties of the materials are taken into account, but the material cost and availability are important factors. Special attention is paid to the extra losses in the materials because of the high operating frequencies.

One of the advantages of the HS machines is the direct connection with the working tool, which eliminates a need for a gearbox. In the applications such as a gas compressor or a hermetic turbogenerator, the process environment is aggressive and sets extra limitations on the insulation materials if the electrical machine is in direct contact with the harsh environment. The aging tests should be performed to confirm the stable operation, for instance, in a steam atmosphere or natural gas, of all materials applied in such electrical machines.

3.1 Stator lamination

Stator lamination in the electrical machines can be silicon-iron (Si-Fe), aluminum-iron (Al-Fe), silicon-aluminum-iron (Si-Al-Fe), or cobalt-iron (Co-Fe) based alloys. Co-Fe enables high saturation magnetization and low core losses at very high frequencies (Bernard et al., 2012; Gerada et al., 2014). However, the price of Co-Fe materials is significantly higher compared with Si-Fe, and therefore, they are not used in the PMSM topology under investigation because it aims at a low-cost production price.

Lamination properties include, for example, losses at different frequencies and flux densities, space factor, saturation magnetization, resistivity, and yield strength. These parameters for the most commonly used laminations in high-speed machines are shown in Table 3.1. The data are obtained from several manufacturers (Arnold Magnetics, 2016; Cogent, 2016; Senda et al., 2004).

Table 3.1 Stator lamination material parameters

Material	Loss at 400 Hz and 1 T, W/kg	Loss at 2500 Hz and 1 T, W/kg	Thick-ness, mm	Space factor, k_{Fe}	Satura-tion flux density, T	Resistivity, R, $(\Omega \cdot m)^{-8}$ (μOhm·cm)	Yield strength, MPa	Price
M270-50A	24.1	627	0.5	0.97	1.77	55	470	Low
M270-35A	17.1	352	0.35	0.96	1.76	55	455	Low
NO27	13.7	255	0.27	0.94	1.75	59	440	Medium
NO20	12.2	205	0.2	0.92	1.82	52	400	Medium
NO10	12.1	119	0.1	0.9	1.75	52	400	High
Arnon 5™	9	110	0.125	0.91	1.7	48	320	Very high
10JNEX-900™	6	98	0.1	0.9	1.84	48	610	Very high

The lamination material selection is highly dependent on the required machine efficiency and nominal working frequency. Therefore, losses at the required frequency and lamination thickness are the key material parameters. The other parameters are very similar for all listed materials and do not play a significant role in the case of the stator lamination application. The material cutting method can also influence the core losses (Liu et al., 2008).

Thin and low per unit loss materials are more expensive and may not be available in stock. For example, Arnon 5 and 10JNEX900 have exceptional properties and are expensive. These materials are selected for the most demanding applications.

According to Table 2.1, NO10 was the stator lamination in the 3.5 kW, 45 000 rpm PMSM, and M270-35A was used in the 11 kW PMSM. More expensive NO10 lamination was used in the 3.5 kW prototype because of the high nominal frequency. An acceptable level of losses was achieved using less expensive M270-35A in the 11 kW PMSM.

3.2 Retaining sleeve materials

Selection of the retaining sleeve material is one of the most important steps during the design process of an HS PMSM. In the case of the TC topology used here, the selection of the sleeve material is even more critical. It affects the stable machine operation under rated and partial loads. The factors that define the suitability of the material for the retaining sleeve application are the high mechanical rigidity, low per unit losses, and high thermal conductivity. It is important to combine these properties in one material.

Because of the tough requirements, only a few materials are suitable for the rotor retaining sleeve application. The most commonly used materials are different stainless steel grades (e.g. ANSI 316L), titanium (e.g. TI6Al4V), Inconel 718, and different carbon fiber grades. The parameters of these materials are shown in Table 3.2 (Kolondzovski et al., 2009; Cho et al., 2006). Some other less common materials can be found in the literature (Li et al., 2014b; Yon et al., 2012).

Table 3.2 Rotor retaining sleeve material parameters

Material	Yield strength, MPa	Density, ρ, kg/m^3	Thermal conductivity, λ, W/(m·K) at 100 °C	Resistivity, R, $(\Omega\cdot m)^{-8}$ (μOhm·cm)	Price
ANSI 316L	205	8000	16.2	74	Low
TI6Al4V	880	4430	6.7	178	Medium
Inconel 718	1100	8190	11.4	125	High
Carbon fiber	1000	1800	0.9	2850	High

The yield stress together with the material density defines the maximum rotational speed of the rotor with the fixed geometry. Resistivity defines the amount of losses generated in the retaining sleeve as a result of eddy currents (Li et al., 2014b). Thermal conductivity determines the ability of the material to transfer the heat generated in the permanent magnet and the retaining sleeve.

Stainless steel retaining sleeves can be used only if the stresses are low, for example, if the peripheral speed is below 150 m/s. The losses caused by eddy currents are high in these sleeves because of the low material resistivity value. Therefore, an appropriate geometry design is required to minimize the asynchronous harmonic content of the air gap flux density, which causes eddy currents in the retaining sleeve. The advantages of this material are high thermal conductivity, low price, and wide availability.

The high yield strength and low density of titanium allow tolerating high mechanical stresses. The high resistivity of this material is one of its key advantages. This property allows an electrical machine designer to modify the HS machine parameters in a wider range. A titanium retaining sleeve has an attractive cost/performance ratio and is often the first option in the HS machine topology design under consideration.

Inconel and carbon fiber are used in very demanding applications. They both have outstanding mechanical properties; however, their price is high and availability is limited. The resistivity of Inconel 718 is 30% less than that of TI6Al4V, which causes higher losses. This is compensated with an about 40% higher thermal conductivity of the Inconel enabling better heat dissipation.

Carbon fiber can tolerate the highest stresses because of its high yield strength and low density. It is possible to suggest that, in practice, there are no losses in the carbon fiber retaining sleeve because of the very high material resistivity. The key drawback of the carbon fiber is the very low thermal conductivity caused by the impregnating resin. The heat generated in the PM under the retaining sleeve has to be dissipated. For this purpose, an internal rotor cooling is required in the case of the carbon fiber retaining sleeve. It is very difficult to arrange such cooling in the HS topology under study.

The selection of the retaining sleeve material is defined by the stresses between the rotor sleeve and the magnet, electromagnetic performance requirements, cost issues, and, sometimes, by the operation medium.

In some cases, it is possible to use rotor coating to reduce eddy current losses in the retaining sleeve. Coating with a material with a very high conductivity, for example, copper can significantly reduce rotor losses caused by eddy currents. In addition, a highly conductive coating filters air gap flux density harmonics and reduces permanent magnet losses caused by eddy currents. This principle is also used in the copper-coated solid rotor high-speed induction motors.

3.3 Permanent magnets

In order to minimize the rotor eddy current losses, appropriately designed HS electrical machines require high values of air gap flux density together with a long air gap. Therefore, only SmCo and NdFeB magnets are usually used in HS PMSMs. NdFeB magnets are more common in PMSM applications and have a higher remanence compared with SmCo. SmCo magnets can tolerate higher temperatures, but they are more expensive. The latest achievements in SmCo materials show a superior performance; a high remanence and an extremely high operating temperature. For example Arnold's Recoma 33 E™ has approx. 1.15 T remanence at 100 °C and can tolerate demagnetization field creating zero flux density in the magnet at 300 °C.

There are many different grades of neodymium permanent magnets, and the grade names depend on manufacturers. In general, the amount of terbium and dysprosium in the

permanent magnet defines the temperature tolerance and demagnetization properties. Simultaneously, a high terbium and dysprosium content decreases the magnet remanent flux density. A high amount of terbium and dysprosium significantly increases the permanent magnet price.

The key parameters of the magnet material for the HS machine design are remanence and demagnetization curves at different temperatures. Even in the high-class magnet grades there is a compromise between high remanence and high temperature tolerances. It is important to remember that the PM properties vary depending on the temperature, and for instance, the magnet remanent flux density must be selected for the rated operating temperature.

Figure 3.1 shows a typical demagnetization curve for a NdFeB magnet. The curve includes the second and third quadrants of the *BH* plane. The demagnetization curves are given for different temperatures. Usually, the manufacturers provide the magnet demagnetization curves for the second quadrant only. In some cases, there can be a requirement for the PMSM to tolerate terminal short-circuits without PM irreversible demagnetization. During a short-circuit, the peak currents may produce negative values of flux density inside the permanent magnet for a very short period. Because of this risk, it is necessary to check the third quadrant of the PM demagnetization curve. In Figure 3.1, the second quadrant is provided by the manufacturer, and the third quadrant is drawn by the author based on the manufacturer's data.

For example, the magnet shown in Figure 3.1 can tolerate negative flux density values down to –0.4 T at 120 °C without irreversible demagnetization. If the working temperature of the magnet is 100 °C, it can tolerate negative flux density down to –0.7 T.

Permanent magnets are prone to Joule losses produced by eddy currents (Dubas & Rahideh, 2014; Bianchi et al., 2010; Han et al., 2010). These eddy current are caused by asynchronous air gap flux density harmonics, which are not filtered by the air gap and the retaining sleeve. The proportion of the PM losses in the total rotor losses grows when the frequency increases. This is because the higher order harmonics pass the retaining sleeve material and penetrate the permanent magnets more easily.

The mechanism of possible hysteresis losses in sintered NdFeB magnets is studied in Publication VII. The paper discusses the theoretical background of the PM polarization behavior, hysteresis behavior, the measurement results, and the role of sintered PM hysteresis losses in the rotating electrical machines.

According to the theoretical studies and measurements, hysteresis losses in PMs seem possible when the flux density in the magnet fluctuates above and below the remanent flux density. This situation is not typical for conventional electrical machines. However, in the case of an HS PMSM, the armature reaction may cause a situation where hysteresis losses occur in normal operation.

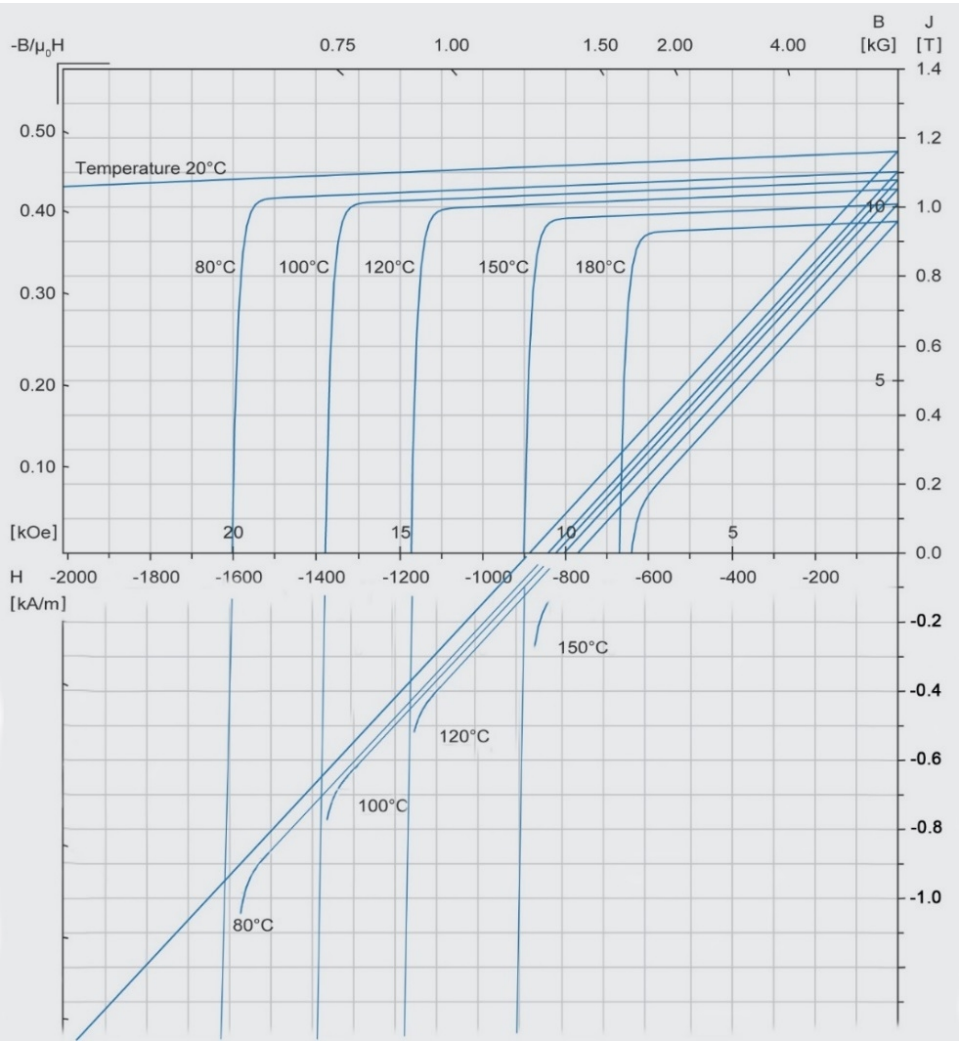

Figure 3.1 Magnet demagnetization curves at different temperatures (Neorem, 2016)

Figure 3.2 illustrates an HS PMSM, which was designed to demonstrate the possibility of PM hysteresis losses. The armature reaction of the machine was designed to be extremely high. The colors show the flux densities inside the magnets in the rated point operation. The magnets located in the center part of the poles are operating close to the magnet remanent flux density, which is 1.01 T in this design. Figure 3.3 shows the variations of the flux density inside the center magnets during one electrical period. It can be seen that the flux density travels above and below the PM remanent flux density.

This situation can cause additional hysteresis losses inside the PM, and therefore, this kind of a PMSM design must be avoided.

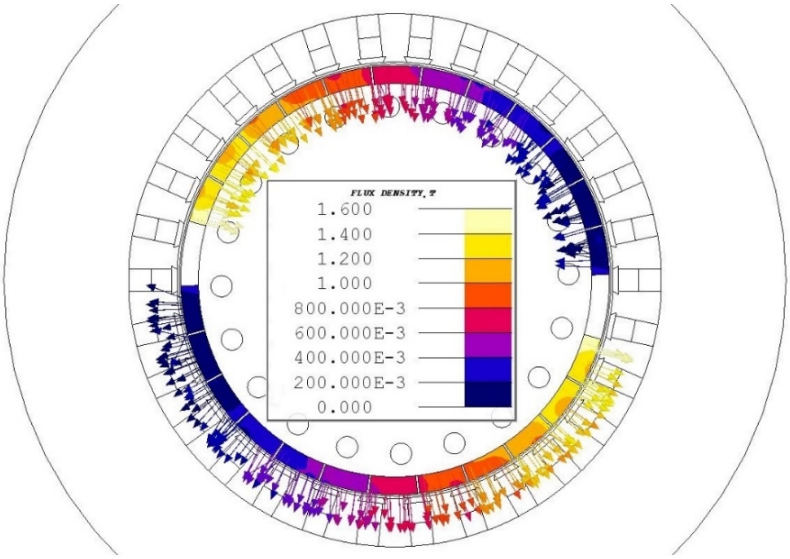

Figure 3.2 Flux distribution of an HS PMSM with a high armature reaction at the rated load

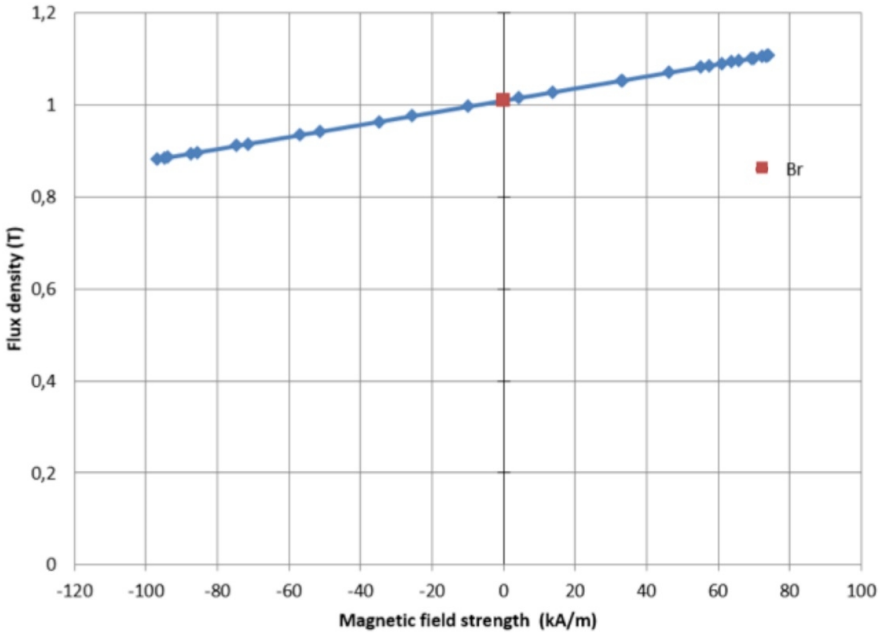

Figure 3.3 PM flux density variation in the magnet located in the center part of the poles during one electrical period

3.4 Materials in a harsh environment

The application of HS electrical machines can significantly increase the efficiency of small turbogenerators. A direct coupling of the electrical machine rotor with the turbine wheel eliminates a need for a gearbox, which increases the system efficiency and enhances the reliability of the turbogenerator.

Publication VI describes a hermetic 1 MW, 12 500 rpm HS IM, designed to operate in a direct contact with the turbine leakage steam. This solution provides an extremely high level of integration and reduces the size of the system. The hermetic construction enables a small power plant without a massive boiler feedwater purification system. As a result, all the materials applied in this high-speed induction machine must tolerate the leakage steam, which has a temperature of about 120 °C, over the machine lifetime.

The material aging tests were performed to verify their applicability before building the prototype. Figure 3.4 shows a test setup built to perform the aging tests in a steam atmosphere. The test column consists of the top part with the input, output, and pressure-relief valves and the removable bottom part.

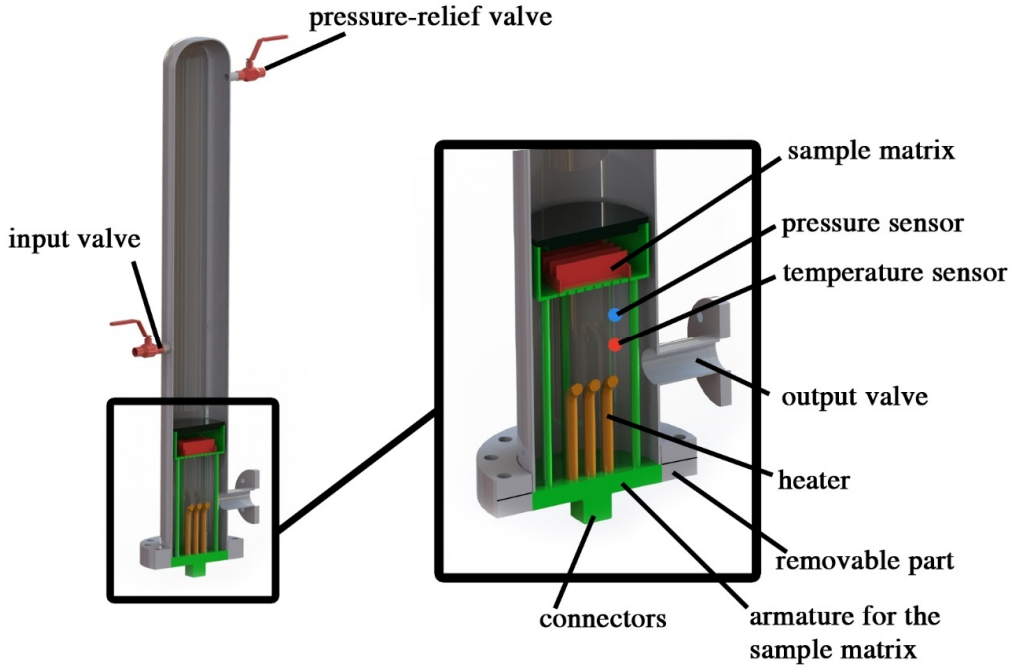

Figure 3.4 Test column for the materials to be used in a steam atmosphere

The bottom part consists of the matrix in which the test samples can be placed, the temperature and pressure sensors, and a controllable heater. In the tests, the samples are

placed into the matrix, the bottom part is fixed, and the column is filled with water. After that, the heater boils water to achieve the required steam atmosphere parameters based on the sensor data. In the test, the required parameters are automatically maintained for a given period.

First, the described test installation was used for the magnetic slot wedge tests. Information about the capability of wedge products to tolerate a steam atmosphere was not available from the wedge manufacturers. Several base materials and coatings were selected and tested in different conditions. A photo of the samples right after the 300 h aging test is shown in Figure 3.5.

Before and after every test all the samples were analyzed, and the results of the measurements were compared. The analyses include visual diagnostics, analysis of the microscope images, measurement of physical dimensions, and the FTIR. Figure 3.6 shows microscope images of one sample before and after the test. Degradation of the coating material is clearly seen in the figure. A detailed description of the magnetic wedge tests can be found in Publication VI.

Figure 3.5 Magnetic wedge samples after the aging test, 300 hours at 150 °C temperature

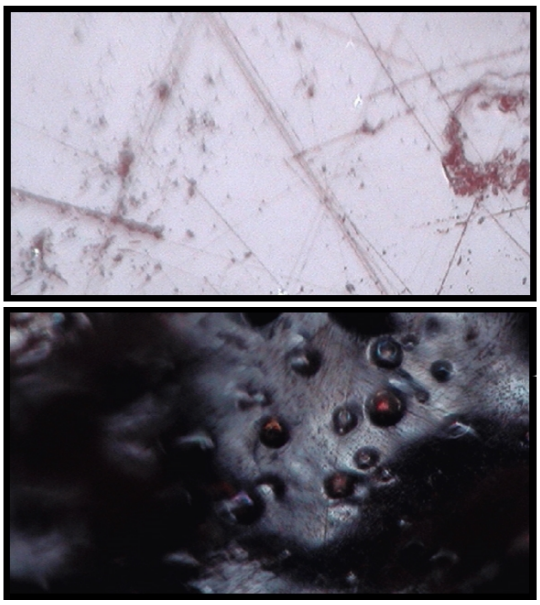

Figure 3.6 Microscope image of the wedge sample before (top) and after the aging test (bottom), 300 hours at 150 °C temperature

Some manufacturers of glued lamination stacks have confirmed the ability of their product to tolerate a steam atmosphere. However, it was decided to verify this fact by measurements in the installation under consideration. The tested glues retained the lamination contact after a 500 h test in all samples. Some sample photos after the test are shown in Figure 3.7 and Figure 3.8. The physical dimension measurements also confirmed the visual observations.

Figure 3.7 Lamination sample glued with Suralac 9000™ (Cogent, 2016) after the aging test, 500 hours at 160 °C temperature

Figure 3.8 Lamination sample glued with VOLTATEX E 1175 W™ (Axalta, 2016) after the aging test, 500 hours at 160 °C temperature

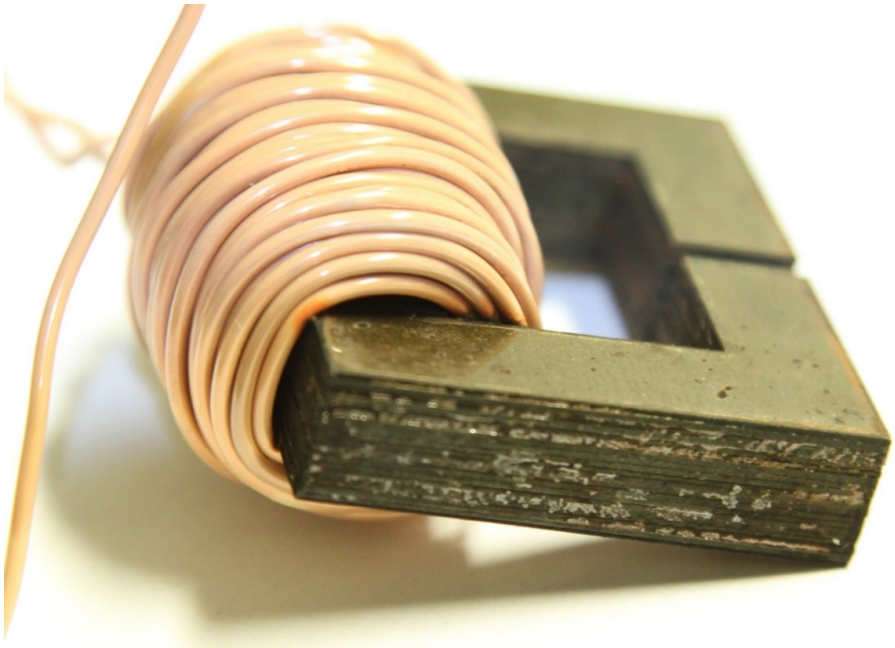

Figure 3.9 Glued lamination wound with a PEEK (Zeus, 2016) insulated wire after the aging test, 500 hours at 160 °C temperature

The other components of the steam-resistant electrical machine insulation system were selected based on the previous research (Sihvo, 2010; Sihvo et al., 2007). Copper wire PEEK (polyetheretherketone) insulation was tested together with one of the glued lamination tests. In this test, the PEEK insulation was broken because of the sharp lamination edges and the absence of any insulation between the wire and the lamination

stack corners. A photo of the broken PEEK insulation is shown in Figure 3.9. Careful winding work must be ensured to avoid the insulation breakdown in the prototype machine.

Based on the previous research and extra aging tests, all components of the steam-resistant insulation system were selected, and their ability to tolerate a steam atmosphere was confirmed. These components are listed in Table 3.3.

Table 3.3 Materials for the steam-resistant insulation system

System component	**Material type**	**Material example**
Conductor insulation	PEEK	PEEK insulated wire
Wire outer insulation	Aramid paper	e.g. Nomex
Impregnating resin	Single-component epoxy resin	e.g. Epoxylite 578EB™
Wedge	Brushed painting with Alkyd lack and dipped in epoxy resin	Epoxy resin 60841
Lamination	M270-50A with bonding core sheet varnish	VOLTATEX E 1175 W™

The materials applied in high-speed electrical machines have to combine high values of the several parameters in order to achieve mechanical rigidity, high electromagnetic performance, acceptable thermal conductivity, and high temperature tolerance. The material price must be taken into account in most of the designs. In addition to these challenges, there can be extra requirements involved in every specific case. For example, when the armature reaction is high permanent magnet hysteresis losses may occur. In applications where the electrical machine is in a direct contact with a harsh environment, aging tests of the insulation system must be performed.

4 Conclusions

In this doctoral dissertation, the important role of high-speed electrical machines in various fields of industry was highlighted. The advantages provided by the HS machinery were discussed, and design problems were introduced. A special HS PMSM topology that helps to overcome rotordynamic and high cost problems related to the HS machines was studied.

The PMSMs having two poles, six stator slots, and tooth-coil windings were designed to enable simple and cost-effective manufacturing, a short total axial length, and low electromagnetic losses. The key geometry dimensions, losses, and ways to minimize these losses were presented in the doctoral dissertation. The loss distribution in the proposed topology is highly dependent on the selected bearing type because friction losses constitute the major part of the total losses.

Two prototypes were built adopting different loss minimization approaches. In the 3.5 kW, 45 000 rpm machine for a turbo blower application, expensive materials with low per unit losses were used. In the 11 kW, 31 200 rpm generator for a micro-ORC power plant, less expensive materials were used, and an effort for the geometry optimization was made to minimize the losses. The stator outer diameter was optimized to minimize the losses and keep the low material consumption. The rotor losses were minimized by using the air gap length and optimization of the tooth tip and magnetic wedge geometries.

The prototype measurement results show a good agreement with the simulation studies. The proposed topology is suitable at least for low-power high-speed applications, and it enables reaching the design targets, namely, simple and cost-effective manufacture, short total axial length, and low electromagnetic losses.

The multidisciplinary nature of the HS PMSM design was illustrated by the two tested prototypes. A design flowchart, which presents the required input and output parameters for the mechanical, electromagnetic, and thermal engineers, was introduced. This flowchart defines the conditions that have to be met to move to the next step and suggests the actions that can be undertaken if these conditions are not met. The implementation of the proposed design procedure can help specialists from different fields to design HS PMSMs effectively, and, with small modifications, other types of HS machines.

In this doctoral dissertation, the most commonly used materials in the HS PMSM were discussed. Lamination, rotor retaining sleeve, and permanent magnet material properties and considerations for the selection of these materials were discussed. Price is one of the key parameters in the material selection for a low-cost HS electrical machine.

Further, the risk of hysteresis losses in sintered NdFeB magnets was discussed in this doctoral dissertation. It is possible to obtain conditions that can cause PM hysteresis losses in HS electrical machines in the rated operating point. The armature reaction is

typically high in machines with a low pole number, which usually the case in HS applications.

Material selection for a steam-resistant insulation system and the material testing procedure were described in this work. These materials will be used in a hermetic turbogenerator.

4.1 Suggestions for further research

The design of an HS electrical machine starts with the selection of the machine topology. The most commonly used machine types are PMSMs and IMs with integral slot distributed windings. It is important to first compare these types of machines in order to start a detailed design. The development of a straightforward procedure that can suggest the most suitable topology based on the input parameters and boundary conditions will be very useful for a fast design concept selection.

The limitations of the presented HS PMSM topology would be studied. The maximum speed and power limits and the factors defining them in the proposed topology should be determined. This will help to overcome the limits and increase the application range of the topology under investigation. It would be advisable to assess methods that help to overcome the limitations in order to minimize the effort needed to increase the machine speed and power and decrease production costs.

The advantages of the AMBs in the HS machines can be fully exploited in cases with a high system integration level. For this purpose, an instrument aimed at the combined design of HS machines with AMBs is required. The development of such an instrument can be beneficial for the electrical, mechanical, and control engineers because it cuts down the design time and the number of errors.

The development of an analytical model for the hysteresis loss assessment in sintered NdFeB PM should be provided. The risk of PM hysteresis losses at a very early stage should be predicted with this model. In the case of such a risk, the machine design can be rapidly adjusted to avoid PM hysteresis losses.

References

Aho, T. (2007), *Electromagnetic Design of a Solid Steel Rotor Motor for Demanding Operation Environments*, Doctoral dissertation (Acta Universitatis Lappeenrantaensis 292), Lappeenranta University of Technology.

de Almeida, A. T., Ferreira, F. J. T. E., and Duarte, A. Q. (2014), "Technical and Economical Considerations on Super High-Efficiency Three-Phase Motors," *IEEE Transactions on Industry Applications*, 50(2), pp. 1274–1285.

Arkkio, A., Jokinen, T., and Lantto, E. (2005), "Induction and permanent-magnet synchronous machines for high-speed applications," in *IEEE Eighth International Conference on Electrical Machines and Systems, ICEMS 2005*, pp. 871–876.

Arnold Magnetics (2016), *Arnon Electrical Steel*, [Online], [Accessed 21 March 2016], available from: http://www.arnoldmagnetics.com.

Axalta (2016), *Axalta Coating Systems*, [Online], [Accessed 5 May 2016], available from: http://www.axaltacs.com.

Bárta, J. and Ondrůšek, Č. (2016), "Finite Element Analysis of High-Speed Solid Rotor Induction Machine with Copper Cage," *Advanced Mechatronics Solutions*, Vol. 393, pp. 195–200.

Bernard, N., Martin, F., and Zaim, M. E. H. (2012), "Design Methodology of a Permanent Magnet Synchronous Machine for a Screwdriver Application," *IEEE Transactions on Energy Conversion*, 27(3), pp. 624–633.

Bianchi, N., Bolognani, S., and Fornasiero, E. (2010), "An overview of rotor losses determination in three-phase fractional-slot PM machines," *IEEE Transactions on Industry Applications*, 46(6), pp. 2338–2345.

Bianchi, N., Bolognani, S., and Luise, F. (2003), "Potentials and limits of high speed PM motors," in *38th IAS Annual Meeting on Conference Record of the Industry Applications Conference, 2003.*, 3(6), pp. 1570–1578.

Binder, A. and Schneider, T. (2007), "High-speed inverter-fed AC drives," in *International Aegean Conference on Electrical Machines and Power Electronics and Electromotion, ACEMP'07 Joint Conference*, pp. 9–16.

Boglietti, A., Cavagnino, A., Staton, D., Shanel, M., Mueller, M., and Mejuto, C. (2009), "Evolution and Modern Approaches for Thermal Analysis of Electrical Machines," *IEEE Transactions on Industrial Electronics*, 56(3), pp. 871–882.

Borisavljevic, A., Polinder, H., and Ferreira, J. A. (2010), "On the Speed Limits of Permanent-Magnet Machines," *IEEE Transactions on Industrial Electronics*, 57(1),

pp. 220–227.

Cedrat (2016), *Cedrat Flux Software*, [Online], [Accessed 16 May 2016], available from: http://cedrat.com.

Cho, H. W., Jang, S. M., and Choi, S. K. (2006), "A design approach to reduce rotor losses in high-speed permanent magnet machine for turbo-compressor," *IEEE Transactions on Magnetics*, 42(10), pp. 3521–3523.

Choi, W., Li, S., and Sarlioglu, B. (2013), "Core loss estimation of high speed electric machines: an assessment," in *Industrial Electronics Society, IECON 2013 - 39th Annual Conference of the IEEE*, pp. 2691–2696.

Cogent (2016), *Material properties*, [Online], [Accessed 21 March 2016], available from: http://cogent-power.com.

Dubas, F. and Rahideh, A. (2014), "Two-dimensional analytical permanent-magnet eddy-current loss calculations in slotless PMSM equipped with surface-inset magnets," *IEEE Transactions on Magnetics*, 50(3), pp. 54–73.

El-Refaie, A. M. (2010), "Fractional-Slot Concentrated-Windings Synchronous Permanent Magnet Machines: Opportunities and Challenges," *IEEE Transactions on Industrial Electronics*, 57(1), pp. 107–121.

Etemadrezaei, M., Wolmarans, J. J., Polinder, H., and Ferreira, J. A. (2012), "Precise calculation and optimization of rotor eddy current losses in high speed permanent magnet machine," in *2012 XXth International Conference on Electrical Machines*, pp. 1399–1404.

van der Geest, M., Polinder, H., Ferreira, J. A., and Zeilstra, D. (2014), "Current sharing analysis of parallel strands in low-voltage high-speed machines," *IEEE Transactions on Industrial Electronics*, 61(6), pp. 3064–3070.

Gerada, D., Mebarki, A., Brown, N. L., Gerada, C., Cavagnino, A., Member, S., and Boglietti, A. (2014), "High-Speed Electrical Machines : Technologies, Trends, and Developments," *IEEE Transactions on Industrial Electronics*, 61(6), pp. 2946–2959.

GIA (2011), *Compressors and Vacuum Pumps - A Global Strategic Business Report*.

Gonzalez, D. A. and Saban, D. M. (2014), "Study of the Copper Losses in a High-Speed Permanent-Magnet Machine With Form-Wound Windings," *IEEE Transactions on Industrial Electronics*, 61(6), pp. 3038–3045.

Han, S. H., Jahns, T. M., and Zhu, Z. Q. (2010), "Analysis of rotor core eddy-current losses in interior permanent-magnet synchronous machines," *IEEE Transactions on*

Industry Applications, 46(1), pp. 196–205.

Huppunen, J. (2004), *High-speed solid-rotor induction machine–electromagnetic calculation and design*, Doctoral dissertation (Acta Universitatis Lappeenrantaensis 197), Lappeenranta University of Technology.

Hämäläinen, H., Pyrhönen, J., Nerg, J., and Talvitie, J. (2014), "AC Resistance Factor of Litz-Wire Windings Used in Low-Voltage High-Power Generators," *IEEE Transactions on Industrial Electronics*, 61(2), pp. 693–700.

IEA (2015), *World Energy Outlook 2015*, Paris, [Online], [Accessed 21 March 2016], Available from: https://www.iea.org.

Jang, S. M., Cho, H. W., and Choi, S. K. (2007), "Design and Analysis of a High-Speed Brushless DC Motor for Centrifugal Compressor," *IEEE Transactions on Magnetics*, 43(6), pp. 2573–2575.

Jastrzebski, R. P., Smirnov, A., Hynynen, K., Nerg, J., Sopanen, J., Lindh, T., Heikkinen, J., and Pyrhönen, O. (2013), "Commissioning and Control of the AMB Supported 3.5 kW Laboratory Gas Blower Prototype," in *Mechatronic Systems and Materials IV*, pp. 451–456.

Keim, D. A. and Herrmann, A. (1998) "The Gridfit algorithm: an efficient and effective approach to visualizing large amounts of spatial data," *Visualization '98. Proceedings*, Research Triangle Park, NC, USA, 1998, pp. 181-188.

Kolondzovski, Z., Arkkio, A., Larjola, J., and Sallinen, P. (2011), "Power limits of high-speed permanent-magnet electrical machines for compressor applications," *IEEE Transactions on Energy Conversion*, 26(1), pp. 73–82.

Kolondzovski, Z., Belahcen, A., and Arkkio, A. (2009), "Comparative thermal analysis of different rotor types for a high-speed permanent-magnet electrical machine," *IET Electric Power Applications*, 3(4), p. 279–288.

Li, W., Qiu, H., Zhang, X., Cao, J., and Yi, R. (2014a), "Analyses on Electromagnetic and Temperature Fields of Superhigh-Speed Permanent-Magnet Generator With Different Sleeve Materials," *IEEE Transactions on Industrial Electronics*, 61(6), pp. 3056–3063.

Li, W., Qiu, H., Zhang, X., Cao, J., Zhang, S., and Yi, R. (2014b), "Influence of rotor-sleeve electromagnetic characteristics on high-speed permanent-magnet generator," *IEEE Transactions on Industrial Electronics*, 61(6), pp. 3030–3037.

Lim, M., Chai, S., Yang, J., and Hong, J. (2015), "Design and Verification of 150-krpm PMSM Based on Experiment Results of Prototype," *IEEE Transactions on Industrial Electronics*, 62(12), pp. 7827–7836.

Liu, Y. (2010), "Critical wavelength of eddy currents and its influence on harmonic losses in solid poles,' in *XIX International Conference on Electrical Machines - ICEM 2010*, IEEE, pp. 1–6.

Liu, Y., Kashif, S. K., and Sohail, A. M. (2008), "Engineering considerations on additional iron losses due to rotational fields and sheet cutting," in *18th International Conference on Electrical Machines*, IEEE, pp. 1–4.

Magnussen, F. and Lendenmann, H. (2007), "Parasitic Effects in PM Machines With Concentrated Windings," *IEEE Transactions on Industry Applications*, 43(5), pp. 1223–1232

Malkamäki, M., Jaatinen-Värri, A., Honkatukia, J., Backman, J., and Larjola, J. (2015), "A High Efficiency Microturbine Concept", in *11th European Conference on Turbomachinery Fluid Dynamics and Thermodynamics, ETC11*, pp. 1–12.

MathWorks (2016), *Matlab and Simulink*, [Online], [Accessed 16 May 2016], available from: http://www.mathworks.com

Merdzan, M., Paulides, J. J. H., and Lomonova, E. A (2015), "Comparative analysis of rotor losses in high-speed permanent magnet machines with different winding configurations considering the influence of the inverter PWM," in *2015 Tenth International Conference on Ecological Vehicles and Renewable Energies (EVER)*, pp. 1–8.

Moghaddam, R. R. (2014), "High speed operation of electrical machines, a review on technology, benefits and challenges," in *2014 IEEE Energy Conversion Congress and Exposition, ECCE 2014*, pp. 5539–5546.

Morimoto, S., Asano, Y., Kosaka, T., and Enomoto, Y. (2014), "Recent technical trends in PMSM," in *2014 International Power Electronics Conference (IPEC-Hiroshima 2014 - ECCE-ASIA)*, pp. 1997–2003.

Neorem (2016), *Neorem Magnets*, [Online], [Accessed 21 March 2016], available from: http://www.neorem.fi.

Noguchi, T. and Kano, M. (2007a), "Development of 150000 r/min, 1.5 kW permanent-Magnet motor for automotive supercharger," in *Proceedings of the International Conference on Power Electronics and Drive Systems*, pp. 183–188.

Noguchi, T., Takata, Y., Pyamashita, Y., Komatsu, Y., and Ibaraki, S. (2007b), "220,000-r/min, 2-kW permanent Magnet Motor Drive for Turbocharger," *Electrical Engineering in Japan*, 161(3), pp. 31–40.

Petrov, I. and Pyrhönen, J. (2013), "Performance of Low-Cost Permanent Magnet Material in PM Synchronous Machines," *IEEE Transactions on Industrial*

Electronics, 60(6), pp. 2131–2138.

Pyrhönen, J. (1991), *The high-speed induction motor : calculating the effects of solid-rotor material on machine characteristics*, Doctoral dissertation, Acta Polytechnica Scandinavica EI 68.

Pyrhönen, J., Jokinen, T., and Hrabovcova, V. (2008a), *Design of Rotating Electrical Machines*, Chichester, UK: John Wiley & Sons.

Pyrhönen, J., Nerg, J., Kurronen, P., and Lauber, U. (2008b), "High-Speed, 8 MW, solid-rotor Induction motor for gas compression," in *Proceedings of the 2008 International Conference on Electrical Machines, ICEM'08*, pp. 1–6.

Pyrhönen, J., Nerg, J., Kurronen, P., and Lauber, U. (2010), "High-speed high-output solid-rotor induction-motor technology for gas compression," *IEEE Transactions on Industrial Electronics*, 57(1), pp. 272–280.

Sagawa, M., Fujimura, S., Yamamoto, H., Matsuura, Y., and Hiraga, K. (1984), "Permanent magnet materials based on the rare earth-iron-boron tetragonal compounds," *IEEE Transactions on Magnetics*, 20(5), pp. 1584–1589.

Senda, K., Namikawa, M., and Hayakawa, Y. (2004), "Electrical Steels for Advanced Automobiles — Core Materials for Motors , Generators , and High-Frequency Reactors," *JFE Technical Report*, 4(4), pp. 67–73.

Sihvo, V. (2010), *Insulation System in an Integrated Motor Compressor*, Doctoral dissertation (Acta Universitatis Lappeenrantaensis 411), Lappeenranta University of Technology.

Sihvo, V., Nerg, J., and Pyrhönen, J. (2007), "Insulation system and thermal design of a hermetically sealed turbo-generator operating in a small-power CHP plant," in *2007 International Conference on Clean Electrical Power, ICCEP '07*, pp. 45–50.

Sullivan, C. R. (1999), "Optimal choice for number of strands in a litz-wire transformer winding," *IEEE Transactions on Power Electronics*, 14(2), pp. 283–291.

Tenconi, A., Vaschetto, S., and Vigliani, A. (2014), "Electrical Machines for High-Speed Applications : Design Considerations and Tradeoffs," *IEEE Transactions on Industrial Electronics*, 61(6), pp. 3022–3029.

TMR (2012) *HVAC (Heating, Ventilation and Air Conditioning) Market - Global Industry Analysis, Size, Share, Growth, Trends and Forecast 2012 – 2018*.

Uusitalo, A., Honkatukia, J., Turunen-Saaresti, T., and Larjola, J. (2014), "A thermodynamic analysis of waste heat recovery from reciprocating engine power plants by means of Organic Rankine Cycles," *Applied Thermal Engineering*, 70(1),

pp. 33–41.

Wojda, R. P. and Kazimierczuk, M. K. (2012), “Winding resistance of litz-wire and multi-strand inductors,” *IET Power Electronics*, 5(2), pp. 257–268.

Yon, J. M., Mellor, P. H., Wrobel, R., Booker, J. D., and Burrow, S. G. (2012), “Analysis of Semipermeable Containment Sleeve Technology for High-Speed Permanent Magnet Machines,” *IEEE Transactions on Energy Conversion*, 27(3), pp. 646–653.

Zeus (2016), *Zeus Incorporated*, [Online], [Accessed 5 May 2016], available from: http://www.zeusinc.com.

Zhang, F., Du, G., Wang, T., Liu, G., and Cao, W. (2015), “Rotor Retaining Sleeve Design for a 1.12-MW High-Speed PM Machine,” *IEEE Transactions on Industry Applications*, 51(5), pp. 3675–3685.

Zhu, Z. Q., Ishak, D., Howe, D., and Chen, J. (2007), “Unbalanced Magnetic Forces in Permanent-Magnet Brushless Machines With Diametrically Asymmetric Phase Windings,” *IEEE Transactions on Industry Applications*, 43(6), pp. 1544–1553.

Publication I

Uzhegov, N., Pyrhönen, J., and Shirinskii, S.
Loss minimization in high-speed permanent magnet synchronous machines with tooth-coil windings

Reprinted with permission from
39th Annual Conference of the IEEE Industrial Electronics Society, IECON 2013
pp. 2960–2965, Nov. 2013

Loss Minimization in High-Speed Permanent Magnet Synchronous Machines with Tooth-Coil Windings

Nikita Uzhegov, Juha Pyrhonen, *Member*, *IEEE*
Electrical Engineering Department
Lappeenranta University of Technology
Lappeenranta, Finland
nikita.uzhegov@lut.fi, juha.pyrhonen@lut.fi

Sergey Shirinskii
Institute of Electrical Engineering
Moscow Power Engineering Institute
Moscow, Russia
shirinskiisv@gmail.com

Abstract— **This paper investigates loss minimization in high-speed, low-power Permanent Magnet Synchronous Machines (PMSMs) with tooth-coil windings (TC-PMSMs). The influence of the main geometric parameters on the loss distribution is studied. Stator core and winding losses as well as rotor sleeve and permanent magnet (PM) losses are evaluated. The effect of the magnetic wedges on the loss distribution is examined. The machine working temperature and related PM demagnetization risks at the rated working point are presented for two- and three-phase short-circuits. The total losses of the designed PMSM are evaluated and a minimum total loss value is obtained.**

Keywords—Permanent magnet (PM) machines; magnetic losses; design optimization.

I. INTRODUCTION

The aim of reducing energy production losses and increasing energy efficiency forms the underlying motivation for much research and new technology. Within this context, distributed generation is one of the more rapidly developing fields of energy research and production. The utilization of distributed power generation means the design of systems based on site-specific conditions, the minimization of transmission losses and a decrease in the share of conventional electricity production [1].

The Organic Rankine Cycle (ORC) is a well-known physical method used to transform waste heat into electrical energy and is eminently suitable for decentralized energy production applications [2]. An important part of ORC systems converting thermal energy first into mechanical energy and then to electricity is a high-speed turbo generator realized with a Permanent Magnet Synchronous Generator (PMSG).

Permanent Magnet Synchronous Machines (PMSMs) have found application in a number of fields, for instance, hybrid electric vehicles (HEV), ship propulsion, wind turbines and elevators [3]. The direct drive high-speed operation principle of PMSMs creates the possibility of increasing machine power and torque densities and also of simplifying the system design by removing the need for a gearbox [4]. Well-known examples of applications using high-speed Permanent Magnet Synchronous Machines (HSPMSM) are vacuum pumps, turbines, machine tools, compressors, blowers, friction welding units, and machine tool spindle drives, to name a few [4], [5]. In recent years, tooth-coil windings have gained popularity due to their manufacturing advantages. Such windings consist of section coils with a coil span of a slot pitch [6].

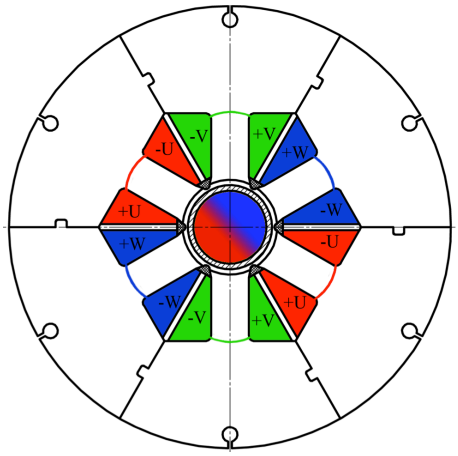

Figure 1 High-Speed Permanent Magnet Synchronous Generator geometry with segmented stator

This paper discusses loss minimization using as an example the design of a high-speed PM generator for a micro-ORC power plant project. In the generator design, the principal requirements of the project were low losses and short length. Based on the given boundary conditions, an electrical machine with a PM and tooth-coil windings was selected for investigation. Such coil configuration has a number of advantages, for example, short end turns, a high slot fill factor, low cogging torque and good fault tolerance [7]. The output power of the designed two-pole permanent-magnet synchronous generator (PMSG) is 11 kW at 31 200 rpm. The geometry of the PMSG is illustrated in Fig. 1.

Fig. 2 (a) shows the longitude section of PMSM with traditional distributed windings and the number of slots per pole and phase, q equal to 2 an equivalent to the designed

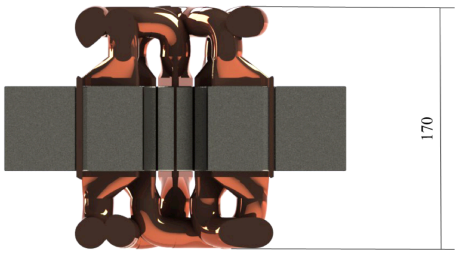

(a)

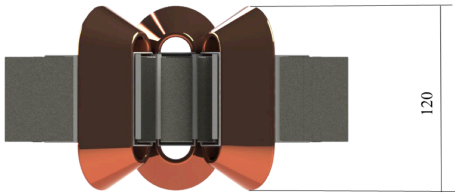

(b)

Figure 2 (a) Longitudinal section of a q=2 PMSM with distributed windings (b) Longitudinal section of a HSPMSM with tooth-coil windings

generator. In Fig. 2 (b) longitude section of the designed PMSM with tooth-coil windings is reported. The end windings lengths of these machines are 110 mm and 60 mm respectively. It should be noted that the total length of the machine with the tooth-coil windings configuration is significantly shorter, 50 mm less.

The main focus of the machine design process was loss minimization and, therefore, stator and rotor losses were examined in detail. The influence of the tooth-coil windings on the copper loss was compared with that of the distributed windings. Optimal design parameters were derived for the rated operating point. To ensure the viability of the PM, a worst-case scenario of the short-circuits was modelled using finite-element model (FEM) analysis.

II. Main Geometry Parameters Selection

Electrical machine design is an iterative process. After defining the boundary conditions and setting the performance goals, the first step is an analytical preliminary calculation. A computational method suitable for the developed HSPMSG is explained in detail in [8]. After that FEM analysis was performed based on the acquired parameters to obtain precise information about the behaviour of the machine.

One of the key advantages of tooth-coil winding PMSMs is a high slot fill factor, which can be achieved by stator segmentation. The segmented construction is shown in Fig. 1 and has been widely discussed in the literature [7], [9]-[11]. Moreover, the approach simplifies manufacturing, and due to the low magnetic flux density in the stator yoke and the tight segment connections, the approach does not cause extra eddy-current losses, as described in [12].

The low stator yoke induction is attained by selecting an exceptionally large stator outer diameter. The application discussed in this paper does not restrict this geometry parameter and consequently this optimization procedure was carried out.

The classical equation for iron power loss per unit value is:

$$P_c=(\sigma d^2/12)\cdot(1/T)\int_0^T B(t)^2\,dt\,, \qquad (1)$$

where P_c is the per unit power loss, and σ and d are the lamination sheet conductivity and thickness respectively [13]. Consequently, the power loss over the period T is proportional to the squared magnetic flux density B. Therefore, in order to reduce the stator yoke losses, it is necessary to lower the value of the flux density. In the optimization procedure, the value of the stator outer diameter was varied with the aim of finding the lowest value at which the heat exchange of the generator with the environment satisfies the given requirements.

Fig. 3 illustrates the iron losses of the stator yoke and the stator teeth as a percentage of the total stator iron losses for the machine under study. As the stator outer diameter increases, the share of the stator teeth losses grows and the proportion of the stator yoke losses reduces. At the point when the geometry parameter is equal to 242 mm, the losses shares from the two parts of the stator become equal, indicating appropriate heat transfer at the stator outer surface. Further enlargement of the stator has little impact on the total stator iron loss value and additional material expenses incurred in further enlargement are inefficient.

The PM length must be chosen carefully at the design stage, because the 2D FEM analysis does not consider the end effects. The current linkage of the permanent magnet behaves differently than the winding current linkage, therefore, to avoid back-electromotive-force (back EMF) reduction the magnet length must be at least an air-gap distance longer than the stator stack [14].

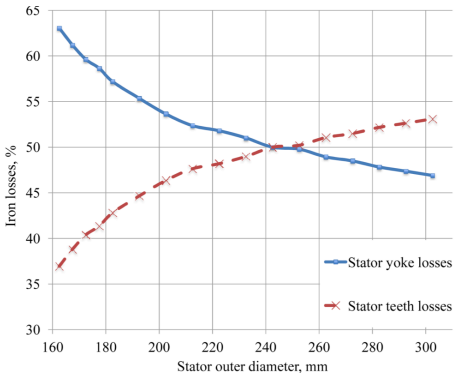

Figure 3 Stator iron losses in stator yoke and stator teeth versus stator outer diameter. Notice that the absolute value of the losses in stator teeth remains the same

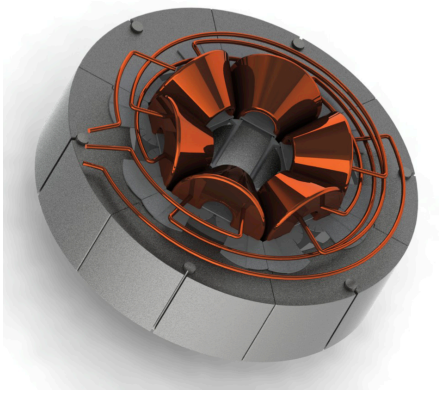

Figure 5 3D model of the Permanent Magnet Synchronous Generator stator

The stator configuration with winding turns, connection wires, slot wedges and insulation is given in Fig. 4.

III. Stator Losses

Stator iron losses are highly dependent on the operating frequency. According to (1) the per unit hysteresis power loss is inversely proportional to the period $T = 1/f$, where f is the synchronous frequency. Therefore, in high-speed machines, extra attention should be paid to the stator iron losses, which, it should be noted, are mainly caused by the PM flux.

The loss minimization task implies utilization of better materials than in conventional electrical machines. The first step is to reduce the lamination sheet thickness since the per unit power loss is proportional to the square of this geometry parameter. The second step is to select material with a low value of per unit loss at an acceptable price. Electromagnetic steel that satisfies the criteria in our case is M-270-35A.

Analytical calculation of core stator losses is very demanding and various methods and approaches have been published [15], [16]. Nonetheless, published analytical computations are not accurate enough because the different parts of the machine exhibit different directions and magnitudes of alteration of magnetic field. Consequently, FEM analysis was required to ensure the accuracy of the results. Based on the methods utilized in the 2D FEM software, in addition to the material resistivity, thickness, stator stack space factor and synchronous frequency of the generator, it was necessary to know also the coefficient of the magnetic losses by hysteresis k_h and the coefficient of the magnetic losses in excess k_e. First, data of per unit metal losses at the various values of the flux densities and frequencies had to be obtained. Manufacturers usually give information about per unit iron losses for the different steel types only for 50 Hz sinusoidal supply. However, in [17] it is possible to find loss data at higher frequencies. The loss coefficients can then be found using the method described in [13].

The main principal of the coefficients searching method is a minimization of the square of difference between the manufacturer measured loss data and the full iron losses calculated according to:

$$P_{\text{Bertotti}} = k_h B^2 f V + \frac{\pi^2 \sigma d}{6} f^2 B^2 V + k_e \cdot 8.67 \cdot (Bf)^{1.5} V \qquad (2)$$

where V is the volume occupied by one kilogram of a steel.

Fig. 5 shows the components of the lamination losses calculated with (2) including hysteresis, classical and excess losses. There are no excess losses; therefore, the coefficient of the magnetic losses in excess is equal to zero. The curves depicting measured and total computed losses correspond to each other well due to the sufficiently accurate value of the coefficient of magnetic losses by hysteresis. The hysteresis losses and the classical losses are almost the same.

The parameters were found for 400 Hz frequency and further exploration showed a slight increase in the k_h with higher sinusoidal frequency. Hence, interpolation of the coefficient was performed and the exact value for the rated operating conditions obtained.

The final step of the stator iron loss minimization was utilization of the above-mentioned parameters, including k_h and k_e, in the FEM analysis and application of the optimization procedure described in Section II, which lead to a total value of stator core losses equal to 100 W.

The second major part of the stator losses is the copper loss. Compared to the distributed windings generator, the designed tooth-coil windings generator has a low winding factor; however, the length of the end windings is less. Using the analytical procedure described in [8] for the PMSG with distributed windings, $q = 2$ and the same output parameters of the machine was computed. The copper loss analysis of the machine with distributed windings gave about the same value as for the tooth-coil winding machine. Furthermore, implementation of the tooth-coil windings makes stator segmentation possible and, maybe more importantly, the whole machine can be made shorter, making the first critical speed of the rotor higher. To avoid extra losses caused by skin-effect at high frequencies each coil turn was divided into several parallel wires with less diameter.

The segmented stator structure allows an increase in the copper space factor that in turn decreases the current density and leads to lower copper loss. The generator copper loss at the rated operating conditions is 88 W. The direct cooling

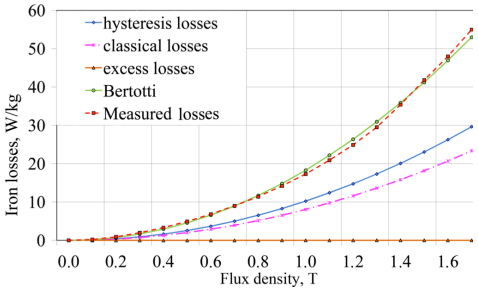

Figure 4 Iron losses model at 400 Hz

construction with the flow inside the stator slot facilitates the removal of heat from the winding surface.

Additional losses in electrical machines are difficult to calculate and the International Electrotechnical Commission (IEC) standard, IEC 60034-2-1 prescribes rules for determination of this kind of losses for induction machines. In [18] the advice is to calculate additional losses as 0.2 % of the input power for the PMSM. Thereby, the generator additional losses at the rated operating point are 22 W.

The design of the generator includes also magnetic wedges installed between the tooth tips. The aim of the wedges is to reduce slot harmonics components that result in decreased cogging torque and rotor eddy-current losses. Due to narrow slot opening, equal to 4 mm even without the wedges, the cogging torque is low and does not exceed 0.1% of the rated torque. The relative permeability of the magnetic wedges varies usually from 1 to 25, and it was noted that with increasing permeability, the stator core losses also increase. If material with a relative permeability value of 3 is applied, the stator teeth core losses increase by 9% due to the increased flux leakage. However, this type of construction significantly reduces rotor losses and helps in reduction of the total generator losses.

IV. Rotor Losses

The two main phenomena causing losses in the rotor are pulsations of the flux due to the stator slot openings [19] and pulsations due to non-sinusoidal and unbalanced armature currents [20]. Since the only rotor cooling mechanism is the air-gap flow and magnet overheating could lead to irreversible demagnetization, precise rotor loss computation is needed. Thermal analysis and appropriate selection of the magnet material are thus critical.

The designed rotor construction consists of a PM cylinder and a retaining sleeve. The FEM analysis revealed that the rotor sleeve makes up the majority of the rotor losses because in order to satisfy the mechanical requirements, it is made from AISI 304L steel, which is highly conductive material. The impossibility of the retaining sleeve segmentation also results from the mechanical rigidness of the construction in case of the high-speed operation.

One way to reduce the rotor sleeve losses would be to replace the material with a material with higher resistivity, for instance, titanium. However, this approach would significantly increase the price of the generator. Another possibility would be to narrow the sleeve to reduce the area of possible eddy-currents, but the minimum thickness must be above 2.5 mm to make manufacturing possible. The copper cladding discussed in [19] cannot be utilized in the considered machine because of the manufacturing and assembling complexity.

TABLE I. Rotor Temperature With Different Air-Gap Length

Air-Gap Length, mm	Rotor Surface Temperature, °C
2.9	142.7
3.4	141.2
4.4	138.7

By increasing the air-gap, the amount of flowing working fluid also grows. Increased air gap can be realized by cutting the lamination. Table I illustrates the dependence of the rotor temperature on the air-gap length provided for the working substance flow with constant amount of the rotor losses equal to 45 W. It is noticeable that with the same level of total rotor losses, widening of the air-gap does not affect enough the rotor surface temperature. Moreover, the machine performance does not meet the defined requirements when the air-gap length is above 3.5 mm.

Fig. 6 shows the effect of various approaches to total rotor loss minimization. In the first option, the parameters are an absence of wedges, a 3 mm thick retaining sleeve and a 2 mm air-gap. The rotor losses in this case are above 160 W and the temperature of the rotor surface exceeds the acceptable level. Options from two to five depict implementation of different combinations of the loss minimization steps discussed above. The most efficient option is number five, which involves reduction of the sleeve to the minimum allowed value, i.e. 2.5 mm, inclusion of magnetic wedges with a relative permeability of 3 between the tooth tips, and an increase in the air-gap by reducing the lamination by up to 3.4 mm.

Magnet eddy-current losses are low and decrease from 15 W to 11 W from option 1 to option 5, notwithstanding the rotor sleeve losses part decreasing dramatically. This result is explained by the fact that the flux pulsations do not penetrate deep into the magnet and mostly attenuate in the retaining sleeve.

Table II illustrates the final loss distribution in the designed machine in case of sinusoidal supply. It is noticeable that the major share of the losses occurs in the stator. The total

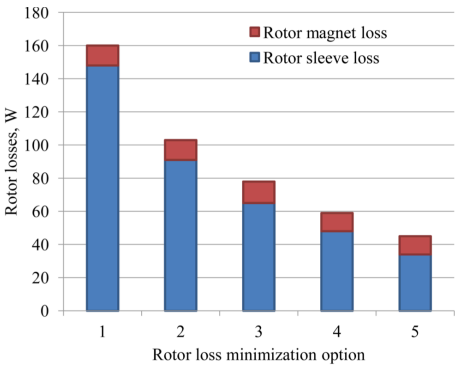

Figure 6 Rotor losses with varying machine structure
1) Air-Gap equal to 2 mm, no wedges, sleeve thickness 3 mm; 2) Air-Gap equal to 2 mm, wedges with relative permeability 3, sleeve thickness 3 mm; 3) Reduction sleeve thickness to 2.5 mm, wedges with relative permeability 3; 4) Increasing the Air-Gap to 2.9 mm by cutting the lamination, wedges with relative permeability 3, sleeve thickness 3 mm; 5) Reduction sleeve thickness to 2.5 mm, increasing the Air-Gap to 3.4 mm by cutting the lamination, wedges with relative permeability 3.

losses do not include mechanical losses for friction and windage. Without this component, the total value is equal to 255 W, which equals 2.32 % of the output power.

V. Magnet Demagnetization Risk

The capitalization of the HSPMSG high power density advantage requires the installation of the high-energy magnets. Utilization of a conducting retaining sleeve and barely cooled rotor would result in a high temperature in the rotor, which may cause magnet demagnetization. Thus, utilization of NdFeB would be risky because of its poor high-temperature tolerance. Although SmCo magnets have lower energy density and a higher price than NdFeB magnets, they would seem to be the only viable solution in the designed generator.

Of the SmCo magnets available, the Sm_2Co_{17} with higher energy density was selected. The demagnetization curves for the selected magnet are depicted in Fig. 7. The figure shows that irreversible demagnetization of the magnet will occur at 200 °C when the normal component of the flux density goes below 0.4 T. At the rated operating point, the temperature does not increase above 150 °C and the demagnetization limit in this case is about 0.38 T.

Fig. 8 illustrates the normal flux density component along the magnet diameter perpendicular to the flux. The FEM computation was made for the moment when one of the phase currents reaches its maximum value during the rated operation. In Fig. 8, it is clearly observed that the normal component of the flux is above 0.84 T at all points and the risk of demagnetization is eliminated even at the 200 °C operating temperature.

Demagnetization of the magnet during two- or three-phase short-circuits is a common problem of PMSMs that results in additional costs. Therefore, situations with two or three-phase short-circuits in normal operation were simulated by FEM. The most dangerous short-circuits occur when one of the current phases crosses the zero value.

Fig. 9 (a) illustrates one phase current behaviour during a two-phase short-circuit. The moment at which the magnet flux density is observed is marked with a line. This point was selected as the current has its maximum magnitude at that time. Fig 9 (b) shows the normal flux density component in the magnet during the short-circuit, obtained as in Fig. 8. It is remarkable that the flux density does not decline below 0.48 T, which shows that even at 200 °C there is not even a partial demagnetization of the PM.

TABLE II. Permanent Magnet Synchronous Generator Losses

Losses Type	Losses Value, W
Copper loss	88
Stator Iron loss	100
Rotor sleeve loss	34
Rotor magnet loss	11
Additional loss	22
Total losses	255

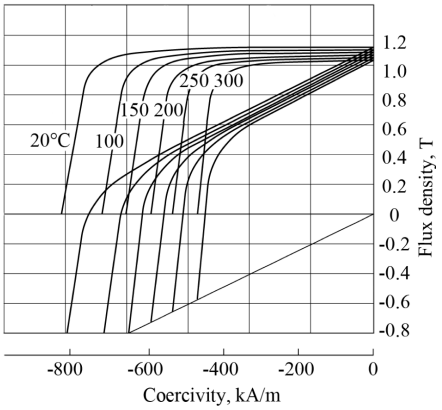

Figure 7 VacoMAX 240 HR demagnetization curve [21]

The situation is similar during the three-phase short-circuit. The normal component of the flux density in the magnet does not decrease below 0.54 T. Consequently, the selected SmCo PM is totally fault tolerant even in the worst-case scenario of short-circuits at a temperature of 200 °C.

VI. Conclusion

A high-speed PM generator for a micro-ORC power plant is briefly described in this paper. The benefits of the tooth-coil windings design are discussed. The focus is on PMSM losses and their reduction.

In minimization of stator losses, it is proposed that the stator outer diameter be increased to equalize the shares of the teeth and yoke iron losses, because this results in better heat exchange with the environment. The computation procedure for the stator iron losses is described in detail. In addition, a number of approaches to exclude possible extra losses in the high-speed PMSG are proposed.

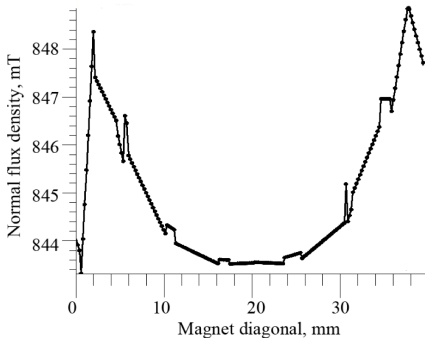

Figure 8 Magnet normal flux density at the rated operating point

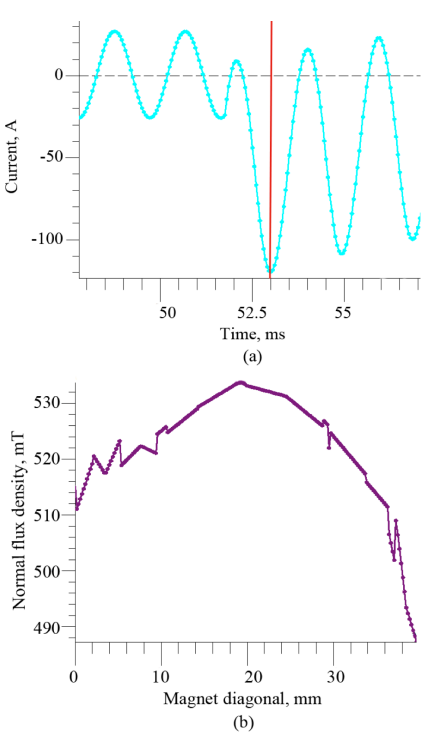

Figure 9 (a) One phase current behavior during a short-circuit
(b) Magnet normal flux density in case of a two-phase short-circuit

As a direct cooling method is used in the generator, the influence of the air-gap length on the rotor outer surface temperature with a constant level of the rotor losses is studied. The effect of magnetic wedges on both stator and rotor losses as well as conductive sleeve losses is shown.

Various loss minimization options are presented. An optimum approach is selected based on analysis that includes electro-magnetic, mechanical and thermal aspects. The loss distribution in the machine is illustrated and the total loss value calculated.

Selection of the PM type for the high-speed generator application is explained. Possible magnet demagnetization is described and the fault tolerance of the rotor during the rated point operation and the worst case short-circuit demonstrated.

REFERENCES

[1] J. Marsden, "Distributed generation systems: A new paradigm for sustainable energy," in Green Technologies Conference (IEEE-Green), 2011 IEEE, 2011, pp. 1-4.

[2] F. Felgner, L. Exel and G. Frey, "Component-oriented ORC plant modeling for efficient system design and profitability prediction," in *Clean Electrical Power (ICCEP), 2011 International Conference on,* 2011, pp. 196-203.

[3] T. M. Jahns, "The expanding role of PM machines in direct-drive applications," in Electrical Machines and Systems (ICEMS), 2011 International Conference on, 2011, pp. 1-6.

[4] N. Bianchi, S. Bolognani and F. Luise, "Potentials and limits of high-speed PM motors," Industry Applications, IEEE Transactions on, vol. 40, pp. 1570-1578, 2004.

[5] M. A. Rahman, A. Chiba and T. Fukao, "Super high speed electrical machines - summary," in Power Engineering Society General Meeting, 2004. IEEE, 2004, pp. 1272-1275 Vol.2.

[6] G. Huth, "Permanent-magnet-excited AC servo motors in tooth-coil technology," Energy Conversion, IEEE Transactions on, vol. 20, pp. 300-307, 2005.

[7] A. M. El-Refaie, "Fractional-Slot Concentrated-Windings Synchronous Permanent Magnet Machines: Opportunities and Challenges," Industrial Electronics, IEEE Transactions on, vol. 57, pp. 107-121, 2010.

[8] J. Pyrhönen, Design of Rotating Electrical Machines. Chichester: Wiley, 2008.

[9] Z. Q. Zhu, Z. Azar and G. Ombach, "Influence of Additional Air Gaps Between Stator Segments on Cogging Torque of Permanent-Magnet Machines Having Modular Stators," Magnetics, IEEE Transactions on, vol. 48, pp. 2049-2055, 2012.

[10] P. B. Reddy, T. M. Jahns, P. J. McCleer and T. P. Bohn, "Design, analysis and fabrication of a high-performance fractional-slot concentrated winding surface PM machine," in Energy Conversion Congress and Exposition (ECCE), 2010 IEEE, 2010, pp. 1074-1081.

[11] R. Wrobel, P. Mellor and D. Holliday, "Thermal analysis of a segmented stator winding design," in Energy Conversion Congress and Exposition (ECCE), 2010 IEEE, 2010, pp. 1290-1297.

[12] Jianxin Shen, Canfei Wang, Dongmin Miao, Mengjia Jin, Dan Shi and Yunchong Wang, "Analysis and optimization of a modular stator core with segmental teeth and solid back iron for pm electric machines," in Electric Machines & Drives Conference (IEMDC), 2011 IEEE International, 2011, pp. 1270-1275.

[13] F. Fiorillo and A. Novikov, "An improved approach to power losses in magnetic laminations under nonsinusoidal induction waveform," Magnetics, IEEE Transactions on, vol. 26, pp. 2904-2910, 1990.

[14] J. Pyrhönen, V. Ruuskanen, J. Nerg, J. Puranen and H. Jussila, "Permanent-Magnet Length Effects in AC Machines," Magnetics, IEEE Transactions on, vol. 46, pp. 3783-3789, 2010.

[15] K. Atallah, Z. Q. Zhu and D. Howe, "An improved method for predicting iron losses in brushless permanent magnet DC drives," Magnetics, IEEE Transactions on, vol. 28, pp. 2997-2999, 1992.

[16] H. Domeki, Y. Ishihara, C. Kaido, Y. Kawase, S. Kitamura, T. Shimomura, N. Takahashi, T. Yamada and K. Yamazaki, "Investigation of benchmark model for estimating iron loss in rotating machine," Magnetics, IEEE Transactions on, vol. 40, pp. 794-797, 2004.

[17] 2013, Mar. [Online]. Available: http://www.sura.se/

[18] T. A. Lipo and University of Wisconsin--Madison. Wisconsin Power Electronics Research Center, Introduction to AC Machine Design. Madison, WI: Wisconsin Power Electronics Research Center, University of Wisconsin, 2011.

[19] Z. Q. Zhu, K. Ng and D. Howe, "Design and analysis of high-speed brushless permanent magnet motors," in Electrical Machines and Drives, 1997 Eighth International Conference on (Conf. Publ. no. 444), 1997, pp. 381-385.

[20] M. R. Shah and A. M. El-Refaie, "Eddy-Current Loss Minimization in Conducting Sleeves of Surface PM Machine Rotors With Fractional-Slot Concentrated Armature Windings by Optimal Axial Segmentation and Copper Cladding," Industry Applications, IEEE Transactions on, vol. 45, pp. 720-728, 2009.

[21] 2013, Mar. [Online]. Available: http://www.vacuumschmelze.com/

Publication II

Uzhegov, N., Kurvinen, E., and Pyrhönen, J.
Design limitations of 6-slot 2-pole high-speed permanent magnet synchronous machines with tooth-coil windings

Reprinted with permission from
16th European Conference on Power Electronics and Applications, EPE'14-ECCE Europe
pp. 1–7, Aug. 2014

Design Limitations of 6-slot 2-pole High-Speed Permanent Magnet Synchronous Machines with Tooth-Coil Windings

Nikita Uzhegov, Emil Kurvinen and Juha Pyrhönen
LAPPEENRANTA UNIVERSITY OF TECHNOLOGY
P.O. Box 20, FI-53851
Lappeenranta, Finland
Phone: +358 46 526-1394
Nikita.Uzhegov@lut.fi
URL: http://www.lut.fi

Keywords

<<AC machine>>, <<Permanent magnet motor>>, <<High-speed drive>>, <<Fault tolerance>>, <<Harmonics>>.

Abstract

Mechanical and electro-magnetic limitations of high-speed tooth-coil electrical machines having 6 slots and 2 poles are investigated. The paper analyses the performance of a designed high-speed Permanent Magnet Synchronous Generator with Tooth-Coil windings (TC-PMSM) with the topology mentioned. The generator nominal power is designed for 11 kW and nominal rotation speed is set to 31 200 rpm.

Introduction

High-speed electrical machines are today a mature and proven technology area. The development of such machines is constantly growing because of the need for the high-speed solution in turbochargers, mechanical turbo-compounding systems, aero engine spools, helicopter engines, racing engines and fuel pumps [1]. The reason for that is a number of advantages, for instance, high power and torque density, simplification of the system by removing a gearbox. Thereby, direct drives reduce weight, costs and improve a reliability of the system [2].

Tooth-coil (TC) windings are becoming popular in different applications. First of all, both single and double layer tooth-coil windings are cheap to manufacture and are therefore an interesting alternative also for low-power high-speed machines if the problems related to the high amount of harmonic current linkages can be solved. One of the main advantages of using TC windings in high-speed applications is the short end windings. Especially, in case of two-pole machines the traditional windings have extremely large end windings that force the rotor long and therefore easily supercritical. Using TC winding instead helps keeping the rotors short which results in higher critical speeds.

In this case the simplest possible permanent magnet (PM) rotor is used as a starting point. A diametrally magnetized cylindrical magnet forms the rotor excitation and a tubular housing around the permanent magnet creates the mechanical strength of the shaft. Such a design has its dimensional and thereby power limits that will be studied in this paper.

Losses of the electrical machine define the cooling needs and contribute the machine design limits. Since single layer TC windings create a higher amount of harmonics multilayer TC windings should be favored in higher speed applications. A comparison of different TC winding types is given in [3]. The air-gap length also has a significant impact on the harmonic content penetrating into the rotor surface. In a high-speed PMSM the air gap length should, therefore, be selected higher than in low speed machines as it is shown in [4]. Higher air gap length leads to greater cooling flow area and that decreases the temperatures in the electric machine active parts.

TC windings also provide the opportunity to pass the coolant directly through the slots between the windings and effectively cool them down. A photo of a stator prototype, using TC windings, is shown in Fig. 1.

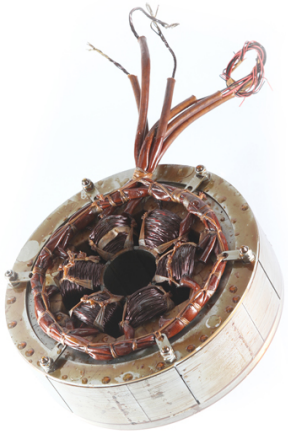

Figure 1: Six-slot two-pole prototype for a small high-speed PMSM

The electromagnetic design parameters define most of the design requirements. However, simultaneously the mechanical properties such as rotor dynamics, mechanical rigidness and manufacturability should be considered to produce a working generator. Selection of the mechanical structure has major impact for the final product lifetime, quality and price. In the following chapter permanent magnet rotor topologies are introduced and the most important mechanical phenomena are studied for the selected topology. The generator main parameters are represented in Table I.

Table I: Generator parameters

Rated speed n_n, min^{-1}	31 200
Rated power P_n, kW	11
Number of poles, p	2
Number of stator slots, Q_s	6
Rated torque, T_n, Nm	3.36
Synchronous inductance, L_s, pu	0.44
Rotor outer radius, R_o, m	0.023

The application where the developed high-speed PM generator is implemented is a micro-Organic Rankine Cycle (ORC) power plant. The target is to design an easily manufacturable and cheap construction for the active parts of the generator. Due to the manufacturability and the preferable TC winding segmented stator structure is selected.

Mechanical topologies and limitations

Several rotor topologies for permanent magnet machines are introduced. The different rotor topologies for PMSMs are shown in Fig. 2. Depending on the machine parameters correct topology should be selected. The rotor topology affects the mechanical rigidness of the machine and it should be selected not only from the machine performance point of view but should also take the mechanical limitations into account. The internal permanent magnet (IPM) rotor (Fig. 2a) has to be optimized carefully in case of the high-speed machines. The construction has to provide structural integrity and at the same time has to be thin enough and not shunt the magnet flux [5]. Nevertheless, a 2-pole electrical machine is difficult to implement with interior permanent magnet with a working design. The surface permanent magnet (SPM) construction (Fig. 2b) is a good option from the electromagnetic point of view, but it needs to have a retaining sleeve to tolerate high-speeds. The full cylinder magnet inside a retaining sleeve is the most convenient option from the mechanical rigidness point of view, however it could produce more

losses [6]. The stator of the designed high-speed Permanent Magnet Synchronous Generator (HSPMSG) is shown in Fig. 1 and the rotor of this machine has a topology illustrated in Fig. 2c.

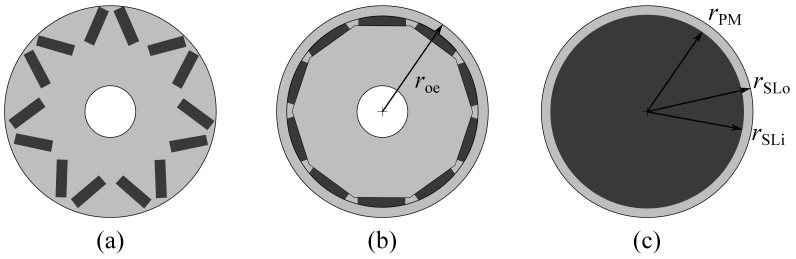

Figure 2: Permanent magnet rotor topologies. a) Multiple-pole internal permanent magnet; b) Two or multiple pole surface permanent magnet with retaining sleeve; c) Two-pole full cylindrical magnet with retaining sleeve

The high-speed machines require more complex computations compared to the low-speed machines due to the material limitations and dynamical behaviour. Mechanical limitations can be divided into three main categories. First is the maximum diameter that the rotor can have to withstand the high rotation speed and the centrifugal force caused by that. Second is the fitting to maintain the contact between the permanent magnet and sleeve during all conditions. Third is the rotor dynamics. The rotor dynamical performance varies as a function of rotation speed and due to that the rotor dynamics have a major effect to the rotor performance and durability.

The coating materials could be divided into conducting and non-conducting ones. The trade-off between these materials is explained in a way that a conducting material causes losses in the rotor, but usually can tolerate more mechanical loads. In high-speed machines with full cylindrical magnet it is necessary to use metallic sleeves, which are, therefore, conducting, to transfer the torque and to maintain rigidity [7].

The preliminary dimensions for the maximum shaft radius can be calculated as

$$r_{oe} = \sqrt{\frac{\sigma_{mec}}{C' \rho \Omega^2}}, \tag{1}$$

where σ_{mec} is the material yield strength, $C' = \frac{3+\nu}{8}$ - for the full cylindrical with retaining sleeve, ν is the Poisson's ratio, ρ is the material density, and Ω is the angular velocity of the rotor. Therefore, the maximum radius of the rotor at the desired speed is restricted by the allowed mechanical stress [4]. It should be noted that equation (1) only considers the centrifugal force and does not take into account any additional stresses such as thermal stresses due to differences in material thermal expansion coefficients, stresses due interference fit between magnet and the sleeve, stresses caused by dynamical conditions such as operating at critical speed. These additional stresses increase the total stress affecting the structure. However, the yield strength should not be exceeded in any condition. Due to that the yield strength value used in equation (1) should include the safety factor and due to that it should be below the actual yield strength. However, this gives an idea of the rotor size.

When the estimated value for the rotor radius is calculated then it is possible to calculate the length of the active part of the rotor for the particular machine to fulfill the required power and torque values. The optimization technique for the rotor volume, which also shows the high dependence on the thermal modeling is described in [8].

The next factor, that could cause the failure of PM and the rotor itself, is the elastic limitation. Magnet and sleeve should be in a contact during all possible operation conditions. In the case of SmCo magnet material and stainless steel the rotation and operation temperature cause magnet and sleeve to expand. The total expansion of the magnet and the sleeve, (u_{PM} and u_{SL}), can be calculated by considering the expansion due to the rotation speed, ($u_{PM\Omega}$ and $u_{SL\Omega}$), as well as the expansion of due to the thermal expansion, (u_{PMtemp} and u_{SLtemp}). The total expansion can be calculated as

$$\begin{aligned} u_{PM}(r) &= u_{PM\Omega} + u_{PMtemp} \\ &= \tfrac{3+\nu_{PM}}{8} \rho_{PM} \Omega^2 \tfrac{1-\nu_{PM}}{E_{PM}} r \left[{r_{PM}}^2 - \tfrac{1+\nu_{PM}}{3+\nu_{PM}} r^2 \right] + \alpha_{PM} r \Delta t \ , \\ u_{SL}(r) &= u_{SL\Omega} + u_{SLtemp} \\ &= \tfrac{3+\nu_{SL}}{8} \rho_{SL} \Omega^2 \tfrac{1-\nu_{SL}}{E_{SL}} r \left[r_{SLi}^2 + r_{SLo}^2 - \tfrac{1+\nu_{SL}}{3+\nu_{SL}} r^2 + \tfrac{1+\nu_{SL}}{1-\nu_{SL}} \tfrac{r_{SLi}^2 r_{SLo}^2}{r^2} \right] + \alpha_{SL} r \Delta t \ , \end{aligned} \tag{2}$$

where r is the radius from the center where the expansion is calculated, subscripts PM and SL refers to magnet and sleeve, ν is the Poisson's ratio of given material, ρ is the material density, Ω is the rotation speed, E is the modulus of elasticity, r_{PM} is the magnet radius, r_{SLi} is the sleeve inner radius and r_{SLo} is the sleeve outer radius, α is the thermal expansion coefficient and Δt is the temperature difference from the room temperature.

Magnet and sleeve should be fixed in a away that the produced torque is transmitted to the rotor shaft. Usually this is done by manufacturing the sleeve smaller than the magnet outer diameter and with the difference in the temperatures enables to install the sleeve over the magnet. This is called shrink fit or interference fit. The interference fit between the magnet and sleeve should be selected so that the yield strength of the magnet or the sleeve are not exceeded and the maximum temperature of the permanent magnet is not exceeded. The dynamical interference fit, λ, can be calculated by considering the total expansion calculated with equation (2) and reduce that amount from the designed static interference fit, u_{sinterf}, amount as $\lambda = u_{\mathrm{PM}} + u_{\mathrm{SL}} - u_{\mathrm{sinterf}}$. The dynamic contact pressure between the magnet and the sleeve can be calculated as

$$p_{\mathrm{c}} = \frac{\lambda r_{\mathrm{PM}} E_{\mathrm{PM}} E_{\mathrm{SL}} (r_{\mathrm{PM}}^2 - r_{\mathrm{SLo}}^2)}{\begin{array}{l}\left(\left(r_{\mathrm{PM}}^4 - r_{\mathrm{PM}}^2 r_{\mathrm{SLo}}^2\right)\nu_{\mathrm{SL}} - r_{\mathrm{PM}}^4 - r_{\mathrm{PM}}^2 r_{\mathrm{SLo}}^2\right) E_{\mathrm{PM}} + \\ \left(\left(-r_{\mathrm{PM}}^4 + r_{\mathrm{PM}}^2 r_{\mathrm{SLo}}^2\right)\nu_{\mathrm{PM}} + r_{\mathrm{PM}}^4 - r_{\mathrm{PM}}^2 r_{\mathrm{SLo}}^2\right) E_{\mathrm{SL}}\end{array}} \tag{3}$$

The stresses due to the rotation speed, thermal effect and pressure from the interference fit are highest in the contact point between magnet and sleeve. Tangential and radial stresses can be calculated as a function of r due to the contact pressure, rotation of the magnet and sleeve as

$$\begin{aligned}
\sigma_{\mathrm{rc}} &= \tfrac{r_{\mathrm{SLi}}^2 p_{\mathrm{c}} - r_{\mathrm{SLo}}^2 p_{\mathrm{o}}}{r_{\mathrm{SLo}}^2 - r_{\mathrm{SLi}}^2} - \tfrac{r_{\mathrm{SLi}}^2 r_{\mathrm{SLo}}^2 (p_{\mathrm{s}} - p_{\mathrm{o}})}{r^2 (r_{\mathrm{SLo}}^2 - r_{\mathrm{SLi}}^2)} \\
\sigma_{\mathrm{tc}} &= \tfrac{r_{\mathrm{SLi}}^2 p_{\mathrm{c}} - r_{\mathrm{SLo}}^2 p_{\mathrm{o}}}{r_{\mathrm{SLo}}^2 - r_{\mathrm{SLi}}^2} + \tfrac{r_{\mathrm{SLi}}^2 r_{\mathrm{SLo}}^2 (p_{\mathrm{s}} - p_{\mathrm{o}})}{r^2 (r_{\mathrm{SLo}}^2 - r_{\mathrm{SLi}}^2)} \\
\sigma_{\mathrm{rPM}\Omega} &= \tfrac{3+\nu_{\mathrm{PM}}}{8} \rho_{\mathrm{PM}} \Omega^2 [r_{\mathrm{PM}} - r^2] \\
\sigma_{\mathrm{tPM}\Omega} &= \tfrac{3+\nu_{\mathrm{PM}}}{8} \rho_{\mathrm{PM}} \Omega^2 [r_{\mathrm{PM}} - \tfrac{1+3\nu_{\mathrm{PM}}}{3+\nu_{\mathrm{PM}}} r^2] \\
\sigma_{\mathrm{rSL}\Omega} &= \tfrac{3+\nu_{\mathrm{SL}}}{8} \rho_{\mathrm{SL}} \Omega^2 [r_{\mathrm{SLi}}^2 + r_{\mathrm{SLo}}^2 - r^2 - \tfrac{r_{\mathrm{SLi}}^2 r_{\mathrm{SLo}}^2}{r^2}] \\
\sigma_{\mathrm{tSL}\Omega} &= \tfrac{3+\nu_{\mathrm{SL}}}{8} \rho_{\mathrm{SL}} \Omega^2 [r_{\mathrm{SLi}}^2 + r_{\mathrm{SLo}}^2 - \tfrac{1+3\nu_{\mathrm{SL}}}{3+\nu_{\mathrm{SL}}} r^2 + \tfrac{r_{\mathrm{SLi}}^2 r_{\mathrm{SLo}}^2}{r^2}]
\end{aligned} \tag{4}$$

where p_{c} contact pressure and p_{o} pressure in the electric machine (air). With the superposition theorem the radial and tangential stresses in the sleeve can be sum into one $\sigma_{\mathrm{rtot}} = \sigma_{\mathrm{rc}} + \sigma_{\mathrm{rSL}\Omega}$ and $\sigma_{\mathrm{ttot}} = \sigma_{\mathrm{tc}} + \sigma_{\mathrm{tSL}\Omega}$. The VonMises stress can be calculated then as $\sigma_{\mathrm{vmises}} = \sqrt{\sigma_{\mathrm{ttot}}^2 - \sigma_{\mathrm{ttot}}\sigma_{\mathrm{rtot}} + \sigma_{\mathrm{rtot}}^2}$. [9, 10]

Third step of the analysis is the rotor's dynamical behaviour over the operation speed. The rotor dynamics is the criterion of the reliable electrical machine operation. The rotor dynamics do not only limit the performance of the motor itself but also affects the bearings, shaft dimensioning and other environment of the installation. The natural frequencies of the rotor as well as the vibration responses caused by excitation forces, *e.g*, unbalance forces, should be determined. In order to determine the rotor dynamics accurately both analytical solution including the finite element method and experimental verification should be performed. The experimental test can be used to determine, *e.g*, the stiffness of the magnet and sleeve contact. First step is to determine the free-free vibration modes, *i.e*, non-supported modes. Three first free-free modes for the studied structure are shown in Fig. 3. The calculated results of the free-free modes are validated with a laser scanning vibrometer (LSV).

Second step is to determine the critical speeds of the rotor bearing system, *i.e*, supported structure. Stiffness of the support and gyroscopic effect varies as a function of rotation speed which affects the natural frequencies. The critical speeds occur when the natural frequencies coincides with the rotor rotation speed. The critical speeds can be determined by plotting a Campbell diagram where the natural frequencies are shown as a function of the rotation speed. Third step is to calculate steady state response where the force caused by residual unbalance shows the vibration amplitude in the critical speeds. The steady state response is used to determine the severity of the critical speeds to the rotor's dynamical behaviour. [11, 12]

Active Magnetic bearings (AMBs) are gaining popularity in high-speed applications because there is no mechanical contact between the bearings and the rotor, thereby mechanical friction losses are excluded from the system, and thus, it is possible to gain higher rotational speeds. An example of AMBs implementation in a high-speed electrical machine and its advantages are described in [13]. Thereby, the correct implementation of this technology could extend the mechanical limit of the high-speed electrical machines.

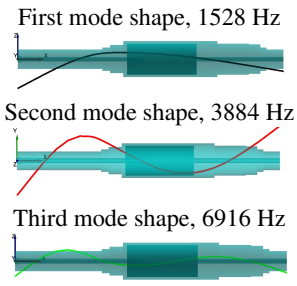

Figure 3: Free-free modes of the studied rotor structure.

Electromagnetic limitations

Losses in the electrical machine apply constraints up to the maximum possible power. The first limit is related to the maximum winding temperature rise and the second is associated to the irreversible demagnetization of the PM [6]. This chapter discusses these two aspects using as an example the design of a HSPMSG for a micro-ORC power plant project.

Copper losses are in a direct ratio to the current density in the windings. Double layer tooth-coil windings allow implementing a segmented structure of the stator. This, in turn, leads to a higher copper space factor and decreases current density. The micro-ORC installation construction together with TC windings also allows to directly remove heat from the windings surface. The micro-ORC working fluid is passing through the slots and cools the windings in an effective way.

The next way to extend the copper loss limit is by using multiphase windings. The increase of the phase number, for instance, up to six, is leading to increasing of the possible maximum machine power by dividing the energy flows in the winding into more channels and decreasing inverter power ratings per phase. This option has also drawbacks, for example, the number of components is increasing which leads to the reliability decrease. The analysis of different multiphase windings for aerospace machine has been studied, for instance, in [14]. However, this limit is a subject of a further investigation.

The rotor losses of the PM machine do not significantly decrease the overall efficiency, however, they could lead to the magnet demagnetization. In the implemented machine construction heat is removed directly from the rotor surface as in case of windings. The SmCo magnet is preferable as it can tolerate higher temperatures, however, its price is higher than NdFeB.

The rotor losses are caused by current linkage harmonics due to both slot opening and discrete current distribution. Since the rotor is moving with constant speed, these harmonics cause eddy-currents in the sleeve and PM [15].

Current linkage harmonics modelled using a finite-element model (FEA) analysis are illustrated in Fig. 4. The total harmonics are obtained by analysing the air gap flux density curve at the rated operating point of the generator. The slot harmonics are received by no-load machine analysis at the rated speed.

The first harmonic is the working harmonic of the three phase 2-pole 6-slot machines and therefore it is used as a base value for per unit representation. Since TC is implemented in HSPMSG the discrete

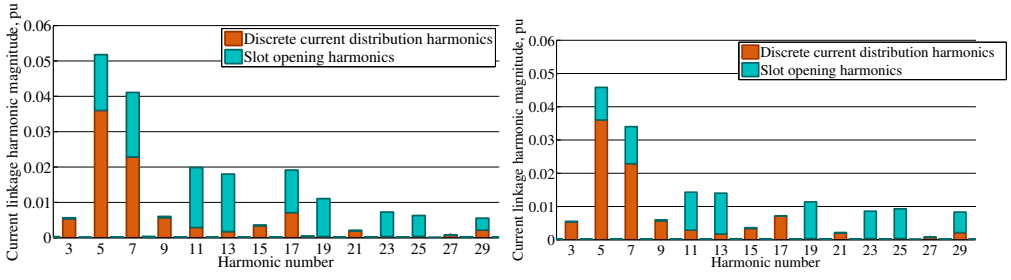

Figure 4: Current linkage harmonics of six-slot two-pole high-speed PMSM. a) Without slot wedges; b) With magnetic slot wedges

Table II: Rotor losses

	Retaining sleeve losses, W	Permanent magnet losses, W	Total rotor losses, W
Without slot wedges	49	12	61
With magnetic slot wedges	34	11	45

current distribution harmonics accounts for a sizable proportion of the total harmonic content. However, only part of these harmonics penetrate the rotor because of the increased air-gap of the electrical machine.

Tooth tips are designed in a way to decrease the harmonics due to slot openings. Nevertheless, further reduction of these harmonics is possible by installation magnetic slot wedge's between the tooth tips. The wedges relative permeability has a great impact on the slot opening harmonic content. Due to the availability limit wedges with a relative permeability equal to 3 were selected.

Fig. 4b shows the analysis of the generator with slot wedges. The total amount of slot opening harmonics is decreased by 25.5% and, for instance, 17^{th} harmonic is eliminated. Due to the air-gap harmonics reduction total rotor losses are decreased, too. Table II shows the amount of losses in the permanent magnet and conducting sleeve before and after the slot wedges installation. The total rotor losses decreased from 61 W to 45 W and therefore the magnet demagnetization risk is decreased.

The final machine configuration involves the reduction of the sleeve to the minimum allowed value, i.e. 2.5 mm, inclusion of magnetic wedges with a relative permeability of 3 between the tooth tips, and an increase in the air-gap by reducing the lamination by up to 3.4 mm.

The number of methods for reducing retaining sleeve losses could be found in [16]. The one way to decrease the magnet losses is to divide the magnet into smaller pieces, therefore, the PM eddy-current losses will reduce.

In case of the SPM with the retaining sleeve the rotor loss shares are similar. For instance, paper [17] describes a technique to estimate rotor magnets and sleeve eddy-current losses in HSPMSM. The final distribution of the rotor losses is 25% in the magnets and 75% is in the sleeve which is close to the results obtained with the 2D FEA for the HSPMSG for a micro-ORC installation.

Conclusion

The implemented machine structure could be used in high-speed applications due to the mechanical rigidness of the rotor and usage of tooth-coil windings. Rotor topology limits the maximum speed of the electrical machine. This limit could be extended by using Active Magnetic Bearings. In case of full cylindrical magnet usage of retaining sleeve leads to the trade offs between rigidness, price and losses. The optimum amount of shrinkage could be found for the existing geometry parameters of the rotor. Double layer TC windings could lead to the copper losses decrease due to the high copper space factor and shorter end windings in comparing with distributed windings. Air-gap length increase cuts the amount of harmonics, which reach the rotor. The installation of the slot wedges between tooth tips leads to the significant reduction of the slot opening harmonic content. Therefore, rotor losses decrease and together with correct selection of the magnet ensure the demagnetization risk absence. A number of ways to extend the design limits of the HSPMSM were proposed. Designing a high-speed electric generator has several requirements and the final solution has several compromises in order to have suitable manufacturing costs. The prototype is build and preliminary runs are made.

References

[1] D. Gerada, A. Mebarki, N. Brown, C. Gerada, A. Cavagnino, and A. Boglietti, "High speed electrical machines;technologies, trends and developments," pp. 1–1, 2013.

[2] A. Tenconi, S. Vaschetto, and A. Vigliani, "Electrical machines for high-speed applications: Design considerations and trade-offs," pp. 1–1, 2013.

[3] L. Alberti and N. Bianchi, "Theory and design of fractional-slot multilayer windings," *Industry Applications, IEEE Transactions on*, vol. 49, no. 2, pp. 841–849, 2013.

[4] J. Pyrhönen, T. Jokinen, and V. Hrabovcova, *Design of Rotating Electrical Machines*. Chichester, UK: John Wiley & Sons, 2008.

[5] A. EL-Refaie, R. Manzke, and T. Jahns, "Application of bi-state magnetic material to automotive offset-coupled ipm starter/alternator machine," *Industry Applications, IEEE Transactions on*, vol. 40, no. 3, pp. 717–725, 2004.

[6] N. Bianchi, S. Bolognani, and F. Luise, "Potentials and limits of high-speed pm motors," *Industry Applications, IEEE Transactions on*, vol. 40, no. 6, pp. 1570–1578, 2004.

[7] Z. Zhu, K. Ng, N. Schofield, and D. Howe, "Improved analytical modelling of rotor eddy current loss in brushless machines equipped with surface-mounted permanent magnets," *Electric Power Applications, IEE Proceedings* -, vol. 151, no. 6, pp. 641–650, 2004.

[8] N. Bernard, F. Martin, and M. El-Hadi Zaim, "Design methodology of a permanent magnet synchronous machine for a screwdriver application," *Energy Conversion, IEEE Transactions on*, vol. 27, no. 3, pp. 624–633, 2012.

[9] A. P. Boresi, R. J. Schmidt, and O. M. Sidebottom, *Advanced mechanics of materials*. Wiley New York, 1993, vol. 5.

[10] A. Borisavljevic, *Limits, modeling and design of high-speed permanent magnet machines*. Springer, 2012.

[11] A. Borisavljevic, H. Polinder, and B. Ferreira, "Overcoming limits of high-speed pm machines," in *Electrical Machines, 2008. ICEM 2008. 18th International Conference on*, 2008, pp. 1–6.

[12] E. H. Maslen and G. Schweitzer, *Magnetic Bearings: Theory, Design, and Application to Rotating Machinery*. Springer, 2009.

[13] A. Smirnov, R. Jastrzebski, K. Hynynen, and O. Pyrhönen, "Comparison of suboptimal control methods in magnetic levitation system," in *Power Electronics and Applications (EPE), 2013 15th European Conference on*, 2013, pp. 1–10.

[14] A. Thomas, Z. Zhu, R. Owen, G. Jewell, and D. Howe, "Multiphase flux-switching permanent-magnet brushless machine for aerospace application," *Industry Applications, IEEE Transactions on*, vol. 45, no. 6, pp. 1971–1981, 2009.

[15] E. Fornasiero, N. Bianchi, and S. Bolognani, "Slot harmonic impact on rotor losses in fractional-slot permanent-magnet machines," *Industrial Electronics, IEEE Transactions on*, vol. 59, no. 6, pp. 2557–2564, 2012.

[16] A. EL-Refaie, "Fractional-slot concentrated-windings synchronous permanent magnet machines: Opportunities and challenges," *Industrial Electronics, IEEE Transactions on*, vol. 57, no. 1, pp. 107–121, 2010.

[17] N. Boubaker, D. Matt, P. Enrici, T. Martire, and F. Nierlich, "Estimation of rotor eddy-current losses for high speed spmsm," in *Power Electronics and Applications (EPE), 2013 15th European Conference on*, 2013, pp. 1–6.

Publication III

Uzhegov, N., Nerg, J., and Pyrhönen, J.
Design of 6-slot 2-pole High-Speed Permanent Magnet Synchronous Machines with Tooth-Coil Windings

Reprinted with permission from
XXI International Conference on Electrical Machines (ICEM),
pp. 2537–2542, Sept. 2014

Design of 6-slot 2-pole High-Speed Permanent Magnet Synchronous Machines with Tooth-Coil Windings

Nikita Uzhegov, Janne Nerg and Juha Pyrhönen

***Abstract*—This paper investigates the advantages and drawbacks of High-Speed Permanent Magnet Synchronous Machines (HSPMSM) having a special topology. The analysis is made by using 3.5 kW and 11 kW machines prototypes. The machines under consideration have 6 slots and 2 poles. The rotor is manufactured as a full cylindrical magnet inside a retaining sleeve. Non-overlapping Tooth-Coil (TC) windings were implemented to improve the manufacturing process. The similarities and differences of the prototypes are discussed. Machines' performances are verified by test measurements.**

I. Introduction

High-speed electrical machines are used in many industrial applications where high power density, small physical size as well as high efficiency are required. Such applications include, for example, gas compression applications, air blowers, and high-speed energy conversion units where high-speed machine is placed on the same shaft with turbine and compressor units [1]–[4]. In all the aforementioned applications one of the main benefits of using high-speed electrical machine technology is the high level of integration which, in turn, gives advantages in terms of total space saving.

In high-speed machinery the number of pole pairs is usually minimized in order to avoid the costs due to the increase of the inverter switching frequency. If we consider a machine with the number of pole pairs $p = 1$, the axial length required normal integral-slot winding end-windings could easily be more than the axial length of the active stator stack. This problem is quite evident in low power machines having traditional integral slot wound stator. To minimize the space needed by the end-windings, tooth-coils can be utilized in the stator instead of traditional windings.

In this paper a three-phase, high-speed permanent magnet synchronous machine topology having six stator slots and two poles is presented. The rotor structure consists of diametrically magnetized permanent magnet and metallic retaining sleeve. The stator winding consists of six tooth coils, and the winding scheme is equivalent of a traditional slot winding having a short pitching of 1/3. Two high-speed machines were designed and manufactured. The first machine was designed for a gas blower application. The power of the first machine is 3.5 kW and its nominal speed is 45 000 rpm. The machine utilizes active magnetic bearings (AMBs) [5], [6]. The second machine was designed as a generator in a micro Organic Rankine Cycle (ORC) power plant. Its nominal power and speed are 11 kW and 32 000 rpm, respectively. The second machine has a segmented stator structure to facilitate easy winding manufacturing.

The paper is organized as follows. First the design and the main parameters of both the machines are presented. The calculation results obtained by Finite element analysis (FEA) are presented. The measurement results of the 11 kW machine are given and the calculation results obtained from FEA are compared with the measurements.

II. Design and Loss Distribution

The topologies of both 3.5 kW and 11 kW high-speed machines are similar. Each machine has 6 slots and 2 poles. The rotor consist of the diametrically magnetized full cylindrical magnets inside the retaining sleeves. The retaining sleeves transfer the torque to the shaft. Both machines have tooth-coil windings. Semi-magnetic wedges are installed between the tooth tips. However, 3.5 kW machine topology utilizes open stator slots because the coils are wound separately in a jig and then plugged into the stator. This reduces winding work costs. 11 kW machine topology uses semi-closed slots to decrease iron losses and reduce harmonic content.

High-speed machine design raise the materials requirements. The stator iron losses are highly frequency dependent. Thereby, to minimize the stator iron losses SURA NO10 steel with 0.1 mm thickness was selected as a stator lamination material for the 3.5 kW machine. This material has low per unit losses even at high frequencies. For the 11 kW machine the M-270-35A stator lamination material with 0.35 mm thickness was selected. This material has a higher value of specific losses, however the geometry optimization was performed to obtain minimum possible stator iron losses. In both cases the lamination sheets were laser cut.

Table I compares the main parameters of the machines under consideration. The rated speed of the 3.5 kW machine is 45 krpm, which is 45 % more than the rated speed of the 11 kW

TABLE I. Designed motors main parameters

Machine parameter	3.5 kW PMSM	11 kW PMSM
Rated speed n_n, min^{-1}	45000	31200
Number of stator slots Q_s	6	6
Number of poles p	2	2
Rated torque T_n, Nm	0.74	3.36
Rated phase back-EMF E_PM, pu	0.91	0.87
Rotor outer diameter D_o, m	0.039	0.046
Air-gap diameter D_i, m	0.043	0.052
External diameter D_e, m	0.140	0.242
Active length l, m	0.022	0.060
Permanent magnet length l_PM, m	0.032	0.070
Permanent magnet remanence B_r, T	1.10	1.12

Nikita Uzhegov, Janne Nerg and Juha Pyrhönen are with LUT-Energy, Lappeenranta University of Technology, P.O. Box 20, 53851 Lappeenranta, Finland (e-mail: nikita.uzhegov@lut.fi, janne.nerg@lut.fi, juha.pyrhonen@lut.fi).

978-1-4799-4389-0/14/$31.00 ©2014 IEEE

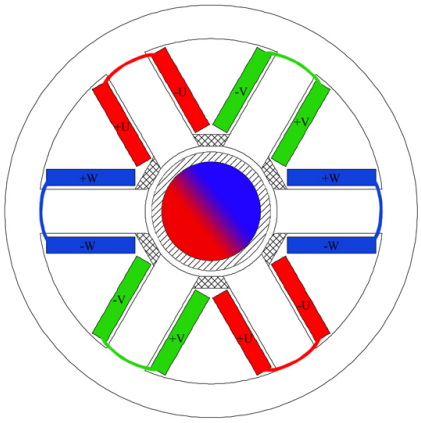

Fig. 1. 3.5 kW High-Speed Permanent Magnet Synchronous Motor geometry enabling tooth coils to be inserted as prefabricated on the teeth

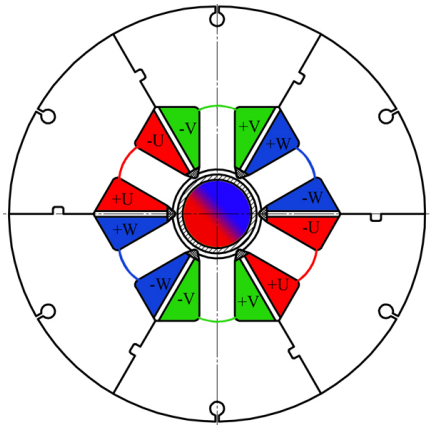

Fig. 2. 11 kW High-Speed Permanent Magnet Synchronous Generator geometry with segmented stator enabling easy manufacturing of the windings despite semi-closed slots

machine. The outer diameters of both rotors are in the same range. That leads to the more strict mechanical limitations of the 45 krpm machine, where the retaining sleeve carries higher centrifugal stresses.

The air-gap flux density defines the machine‘s volume usage. Therefore, it is important to have a high value of the permanent magnet remanence B_r in a high-speed machine. The next factor which defines the magnet selection is the maximum working temperature. Samarium Cobalt (SmCo) magnets can tolerate higher working temperature than the Neodymium Iron Boron (NdFeB) ones, however the SmCo magnet price is higher. To avoid demagnetization problem and to ensure high value of the air-gap flux density SmCo permanent magnets with B_r = 1.1 T and B_r = 1.12 T were selected for the 3.5 kW and 11 kW machine respectively.

Fig. 1 shows the cross-section of the 3.5 kW machine. The machine has straight teeth without any widening in the tooth tip area. It simplifies the winding process enabling prefabricated windings to be inserted on the teeth. Fig. 2 illustrates the cross-section of the 11 kW generator. By comparing the machines' geometries it is possible to notice that the 11 kW high-speed machine in Fig. 2 has an exceptional stator yoke thickness, which is feasible as the application does not limit the diameter. The stator outer diameter was found by an analytical optimization procedure and verified by Finite Elements Method (FEM) analysis. The selected diameter value allows reducing the stator yoke iron losses by reducing the yoke flux density.

The machines under consideration have magnetic wedges between tooth tips. The main purpose of the wedges is to reduce the effects of slot harmonics. In PMSM with 3.5 kW rated power the wedges material Spindurol is used and in 11 kW PM generator Magnoval 2067 wedges are used. Therefore, the cogging torque and rotor eddy-current losses have been decreased in both machines.

In both machines the rotor permanent magnets are 10 mm longer than the active stator length. The PM current linkage stops where the permanent magnet ends. To fully utilize the armature, permanent magnets should be extended, at least one air gap from each machine's side end [7].

The retaining sleeve around the rotor has an important impact on the overall machine design. First of all, in both prototypes conducting material was used for the sleeve. The 3.5 kW machine uses titanium and the 11 kW generator uses stainless steel. Implemented materials were selected because of their mechanical rigidness and ability to transfer the torque from the shaft to the magnet. However, the material's high conductivity leads to eddy-current rotor losses. The analytical approach of calculating eddy-current losses in the conducting sleeves and factors which are influence these losses in Fractional-Slot Concentrated Windings (FSCW) machines are described in [8]. The retaining sleeve material and its conductivity impact on the rotor sleeve losses is studied in [9].

The sleeve thickness and, thereby, its cross-sectional area influence the conductive retaining sleeve losses. Titanium sleeve thickness in 3.5 kW machine is equal to 3 mm to sustain the mechanical stresses. In case of the 11 kW PMSM sleeve the thickness was reduced from 3 mm to 2.5 mm. That decreased the sleeve eddy-current loss by 28 %. Although further thickness reduction should have been possible from the mechanical rigidness point of view, the manufacturability limit was set as 2.5 mm. The retaining sleeve thickness reduction also causes the permanent magnet eddy-current losses to increase because a higher amount of harmonics started to penetrate into the magnet surface. However, the permanent magnet eddy-current loss increased by only 1.5 %.

Fig. 3 shows a photo the one stator segment. In case of the double-layer TC windings stator segmentation simplifies the motor manufacturing. Moreover, assembling the stator after the winding process leads to a higher copper space factor. Therefore, the current density in the stator windings decreased, that cause the reduction of the stator copper losses.

In Fig. 3 each winding turn is divided into several parallel wires. It is done to avoid skin-effect in the windings. Classical

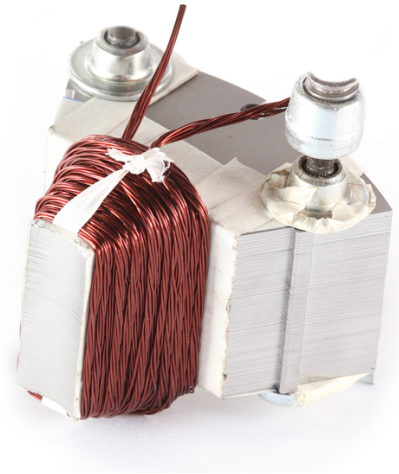

Fig. 3. One segment of the 11 kW High-Speed Permanent Magnet Synchronous Generator prototype

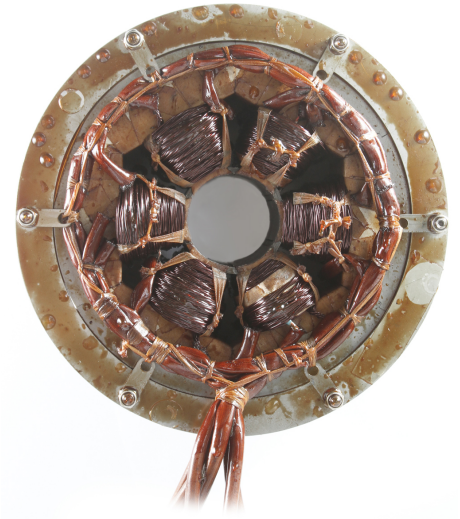

Fig. 4. 11 kW prototype for a small high-speed PMSM

Fig. 5. 3.5 kW High-Speed Permanent Magnet Synchronous Machine stator

penetration depth formula for the conductor suspended in air is

$$\delta_{\mathrm{p}} = \sqrt{\frac{2}{\pi f \mu \sigma}}, \tag{1}$$

where δ_{p} is the penetration depth or skin depth, f is the frequency, μ is the material permeability and σ is the conductivity of the conductor material. To avoid skin effect in the conductor the wire diameter must be less than the skin depth. Thereby, the diameter of each conductor in the 11 kW generator was selected as 1 mm. Also the wires are twisted to avoid the proximity effect and circulating currents.

One of the advantages of the TC windings is the machine fault tolerance. It is achieved due to the simplicity of the end windings. The assembled and impregnated stators in Fig. 4, 5 demonstrate, that the end windings are well separated in the proposed electrical machines. In comparison with the distributed windings machine TC windings do not require phase insulation of the end windings.

Although both PMSM have similar structures the implementation purpose is different, which adds extra features to each machine. For instance, 3.5 kW motor uses Active Magnetic Bearings, which cuts the mechanical losses. The 11 kW generator is designed for a micro ORC power plant. This gave an opportunity to pass the cooling fluid inside the stator slots and remove heat directly from the windings.

Table II shows the loss distribution in the designed electrical machines. In both machines the ratio between the stator iron and copper losses is approaching 0.5. Due to the stator

TABLE II. MACHINES TOTAL LOSSES

Losses Type	3.5 kW PMSM Losses, W	11 kW PMSM Losses, W
Copper loss	104	88
Stator Iron loss	121	100
Rotor Sleeve loss	70	34
Rotor Magnet loss	4	11
Additional loss	17	22
Mechanical loss	125	456
Total losses	441	711

segmentation and as a consequence higher copper space factor, in the 11 kW the current density is lower. Therefore, copper losses of the 11 kW HSPMSG for micro-ORC are 15 % less.

One of the key boundary conditions for the 11 kW prototype design was the loss minimization inside the machine. Because of that the outer diameter of the stator was increased to decrease the stator yoke iron losses. As a result the total iron losses are 17 % higher in the 3.5 kW machine, in spite of the material difference. The other reason for that iron losses difference is the higher working frequency of the 3.5 kW machine.

The rotor losses in the permanent magnet motors are important not only from the efficiency point of view. It is difficult to take away heat from the rotor. It could lead to a high permanent magnet temperature and its irreversible demagnetization. That will cause a full rotor replacement and high costs. Hence, the sleeve eddy-current losses minimization is of high importance as it could compose up to 95 % of the losses of the full cylindrical permanent magnet rotor.

To minimize the rotor sleeve losses in the micro-ORC generator not only the retaining sleeve thickness was cut down but also the magnetic wedge relative permeability and physical air gap length were considered as optimization variables. By varying these three parameters the stainless steel sleeve losses were reduced and draw up only 50 % of the titanium sleeve losses of the 3.5 kW.

The most of the slot harmonics do not penetrate into the magnet and the permanent magnet eddy-current losses are low compared with the conducting sleeve losses.

Due to AMBs implementation in the 3.5 kW machine the mechanical losses consist only of windage losses. In spite of higher nominal rotational speed the mechanical losses are 72 % less in the 3.5 kW machine compared with the 11 kW machine loss. The mechanical losses are important in high-speed machines, for instance, these losses' share of the 11 kW is higher than the total losses of the 3.5 kW machine with AMBs.

The combination of the loss minimization features implemented in 11 kW generator with the AMBs and the materials with low per unit losses will increase the efficiency of the machine with the proposed geometry.

III. Finite Element Analysis

One of the main advantages of the suggested machine topology is the sinusoidal back-EMF waveform. Figs. 6 and 7 show the back-EMFs for the machines under consideration. Due to the sinusoidal waveform the air-gap flux linkage is also close to sinusoidal. Also, the cogging torques of the machines with considered topologies are low. The total torques fluctuations of the 3.5 kW machine is below 0.5 % and in case of the 11 kW generator this parameter is below 0.1 %. The calculated back-EMF RMS voltages were 210.2 V for the 3.5 kW motor and 200.9 V for the 11 kW generator.

The harmonic contents of the back-EMF curves are also presented in Figs. 6 and 7. The seventh harmonic has the largest amplitude for the 3.5 kW machines and composes 0.06 %. For the 11 kW machine the fifth harmonic has the largest amplitude and composes 0.12 %. The total amount of harmonics is equal to 1.16 % of the main harmonic for 3.5 kW PMSM. In case of the 11 kW PMSM this value is equal to 1.82 %.

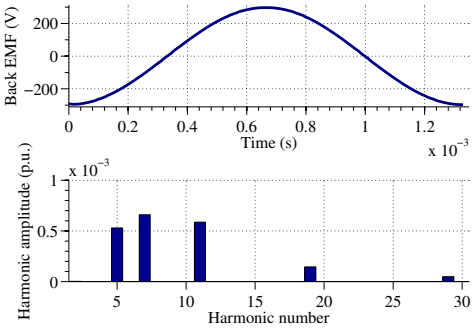

Fig. 6. Back EMF curve and its harmonics of the 3.5 kW PMSM

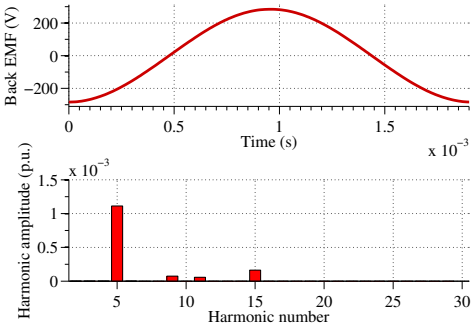

Fig. 7. Back EMF curve and its harmonics of the 11 kW PMSM

IV. Experiments

During PMSM measurements machines were working in the motor mode. Fig. 8 shows the measurement equipment connection scheme. Frequency converter is controlled by PC. It feeds the terminals of the PMSM whilst the current and voltage are measured with Yokogawa PZ–4000 to define the

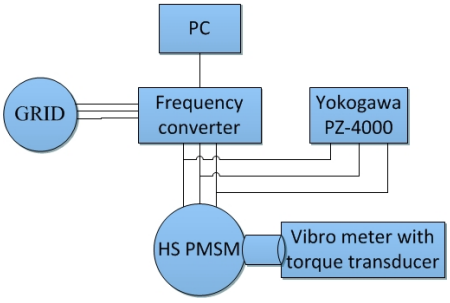

Fig. 8. Equipment connection scheme for the PMSMs measurements

TABLE III. 11 KW PMSM CALCULATED AND MEASURED NO-LOAD LOSSES

Rotational speed, rpm	Calculated mechanical losses, W	Calculated iron losses, W	Total calculated no-load losses, W	Measured no-load losses, W	Calculated and measured losses difference, W
15000	105,5	44	149,5	252	102,5
20000	187,5	55	242,5	346	103,5

input power. The multiplication of torque and speed measured by Vibro-Meter gives the output power.

Fig. 9 shows the assembled measurement installation. The 11 kW PMSG is put inside the casing and connected to an eddy-current brake through a coupling. The eddy-current break is capable to measure the shaft rotational speed up to 50 krpm and cooled by water. Bearings in the measurements installation differs from the analyzed fluid bearings.

PMSM no-load losses are consisting of the iron and mechanical losses. Iron losses were modelled using FEM analysis of the HS PMSM and mechanical losses were calculated by [10]:

$$P_\rho = k_\rho D_\mathrm{r}(l_\mathrm{r} + 0.6\tau_\mathrm{p})v_\mathrm{r}^2, \quad (2)$$

where $k_\rho = 15$ is an experimental factor, D_r the rotor diameter, l_r the rotor length, τ_p the pole pitch, v_r the rotor surface speed.

Table III shows the calculated and measured no-load losses of 11 kW HS PMSG at different speed. The mechanical losses are increasing dramatically with the rotational speed increase.

The difference between calculated and measured no-load losses is about 100 W. This difference could be explained by the additional losses in the coupling between the Vibro-Meter and HS PMSG. These losses were not taken into account in the mechanical losses calculation. The bearings utilized in the test were poorer in performance compared to the fluid bearings used in the final installation.

A precise mechanical loss measurement were possible only without PMs in the rotor.

V. CONCLUSION

The discussed structure of the Permanent Magnet machine has a number of advantages. The tooth-coil windings allow to decrease the total length of the 2-pole machine and increase its reliability. The manufacturing process can be simplified in comparison with the conventional machines with distributed windings. The losses of the considered machines could be reduced by implementing the various described design features. The machines' back-EMFs have a low harmonic content due to the rotor structure and the magnetic wedges installation. As a result torque ripples are negligible in these machines.

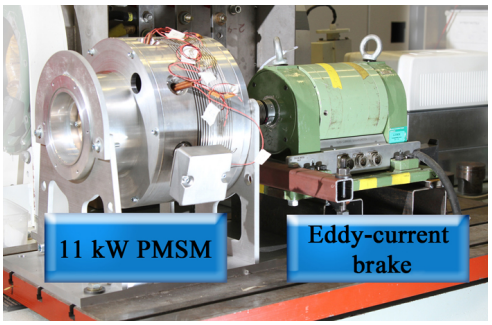

Fig. 9. Test setup. 11 kW PMSM connected to the eddy-current brake

However, the proposed design structure has also several weak points, for instance, high current linkage harmonic content and high conducting sleeve losses. Thereby, the magnet demagnetization risk should be studied in case of NdFeB magnets usage.

The calculation results were checked with the measurements and the measurement results of the 11 kW machine prototype were discussed.

REFERENCES

[1] J. Pyrhonen, J. Nerg, P. Kurronen, and U. Lauber, "High-speed high-output solid-rotor induction-motor technology for gas compression," *Industrial Electronics, IEEE Transactions on*, vol. 57, no. 1, pp. 272–280, Jan 2010.

[2] D. Gerada, A. Mebarki, N. Brown, C. Gerada, A. Cavagnino, and A. Boglietti, "High-speed electrical machines: Technologies, trends, and developments," *Industrial Electronics, IEEE Transactions on*, vol. 61, no. 6, pp. 2946–2959, June 2014.

[3] F. Crescimbini, A. Lidozzi, G. Lo Calzo, and L. Solero, "High-speed electric drive for exhaust gas energy recovery applications," *Industrial Electronics, IEEE Transactions on*, vol. 61, no. 6, pp. 2998–3011, June 2014.

[4] A. Tenconi, S. Vaschetto, and A. Vigliani, "Electrical machines for high-speed applications: Design considerations and tradeoffs," *Industrial Electronics, IEEE Transactions on*, vol. 61, no. 6, pp. 3022–3029, June 2014.

[5] R. Jastrzebski, A. Smirnov, K. Hynynen, J. Nerg, J. Sopanen, T. Lindh, J. Heikkinen, and O. Pyrhonen, "Comissioning and control of the amb supported 3 kw laboratory gas blower prototype," vol. 198, pp. 451–456, 2013.

[6] R. Jastrzebski, A. Smirnov, J. Nerg, A. Jaatinen-Varri, P. Jaatinen, T. Lindh, O. Pyrhonen, J. Sopanen, and J. Backman, "Laboratory testing of an active magnetic bearing supported permanent magnet 3.5 kw blower prototype," in *Power Electronics and Applications (EPE), 2013 15th European Conference on*, Sept 2013, pp. 1–9.

[7] J. Pyrhonen, V. Ruuskanen, J. Nerg, J. Puranen, and H. Jussila, "Permanent-magnet length effects in ac machines," *Magnetics, IEEE Transactions on*, vol. 46, no. 10, pp. 3783–3789, Oct 2010.

[8] A. EL-Refaie, M. Shah, R. Qu, and J. Kern, "Effect of number of phases on losses in conducting sleeves of surface pm machine rotors equipped with fractional-slot concentrated windings," *Industry Applications, IEEE Transactions on*, vol. 44, no. 5, pp. 1522–1532, Sept 2008.

[9] N. Bianchi, S. Bolognani, and F. Luise, "Potentials and limits of high-speed pm motors," *Industry Applications, IEEE Transactions on*, vol. 40, no. 6, pp. 1570–1578, Nov 2004.

[10] J. Pyrhonen, T. Jokinen, and V. Hrabovcova, *Design of Rotating Electrical Machines*. Chichester, UK: John Wiley & Sons, 2008.

BIOGRAPHIES

Nikita Uzhegov (M'14) received the B.Sc. degree from Moscow Power Engineering Institute (MPEI), Moscow, Russia, in 2010 and the M.Sc. degree in electrical engineering from Lappeenranta University of Technology (LUT), Lappeenranta, Finland, in 2012.

He is currently a Doctoral Student in the Department of Electrical Engineering, LUT. His research mainly concerns

electrical machines and drives, particularly high-speed machines.

Janne Nerg (M'99–SM'12) received the M.Sc. degree in electrical engineering, the Licentiate of Science (Technology) degree, and the D.Sc. (Technology) degree from Lappeenranta University of Technology (LUT), Lappeenranta, Finland, in 1996, 1998, and 2000, respectively.

He is currently an Associate Professor with the Department of Electrical Engineering, LUT. His research interests are in the fields of electrical machines and drives, particularly electromagnetic and thermal modeling and design of electromagnetic devices.

Juha Pyrhönen (M'06) received the M.Sc. degree in electrical engineering, the Licentiate of Science (Technology) degree, and the D.Sc. (Technology) degree from Lappeenranta University of Technology (LUT), Lappeenranta, Finland, in 1982, 1989, and 1991, respectively.

He has served as Associate Professor in Electric Engineering at LUT starting 1993 and has been appointed Professor in Electrical Machines and Drives in 1997. He worked as the Head of the Department of Electrical Engineering from 1998 to 2006 and again after 2008. He is active in the research on and development of electric motors and electric drives.

Publication IV

Uzhegov, N., Nerg, J., and Pyrhönen, J.
An Analysis of the 6-Slot 2-Pole High-Speed Permanent Magnet Synchronous Machines with Tooth-Coil Windings

Reprinted with permission from
41st Annual Conference of the IEEE Industrial Electronics Society, IECON 2015,
pp. 1867–1872, Nov. 2015

IECON2015-Yokohama
November 9-12, 2015

An Analysis of the 6-Slot 2-Pole High-Speed Permanent Magnet Synchronous Machines with Tooth-Coil Windings

Nikita Uzhegov, *Member, IEEE*, Janne Nerg, *Senior Member, IEEE*, and Juha Pyrhönen, *Member, IEEE*
Electrical Engineering Department
Lappeenranta University of Technology
Lappeenranta, Finland
Nikita.Uzhegov@lut.fi, Janne.Nerg@lut.fi, Juha.Pyrhonen@lut.fi

***Abstract*—Two low-power High-Speed Permanent Magnet Synchronous Machines (HS PMSM) are reviewed. The powers and speeds of the machines are 3.5 kW at 45 000 rpm and 11 kW at 31 200 rpm. Both machines under consideration have 6 slots and 2 poles and they are both using Tooth-Coil (TC) windings also known as non-overlapping concentrated windings. The rotors of the discussed machines consist of the diametrically magnetized full cylindrical Permanent Magnet (PM) inside a retaining sleeve. The similarities and differences between these two machines are described and explained. The analysis of the air gap flux density, its harmonic content, and loss distribution in comparison with a Distributed Windings (DW) solution is presented with the example of an 11 kW machine. The analytical and numerical calculations are verified by the experimental data. Based on this analysis, conclusions will be drawn regarding the suitability of the implemented topology for a high-speed machinery.**

Keywords*—AC machine; High-speed drive; Permanent magnet machines; Tooth-Coil windings; Finite element analysis; Loss measurement; harmonics.

I. Introduction

High-Speed (HS) rotating electrical machines are already used in industry for several decades. The applications of the HS machinery include, but not limited to, microturbines, automotive, power generation, flywheel, spindle drives, gas compressor and turbomolecular pumps [1]. These machines have several advantages compared to the conventional drive with a gearbox solution, for instance, gearbox elimination, mass reduction, higher system efficiency, and, in some cases, maintenance reduction [2].

The development process of the HS machines differs from the conventional ones because of the strict mechanical and thermal limitations. The new HS drives topologies enable a desirable compromise between the electromagnetic performance, mechanical rigidness, and temperature distribution of the system.

This paper proposes a special topology for the High-Speed Permanent Magnet Synchronous Machines (HS PMSM). This topology is utilized in two manufactured prototypes. The machines under consideration have 2 poles, 6 stator slots, and Tooth-Coil (TC) windings. The performance of these machines, their design solutions, and manufacturing features are presented.

The first developed prototype is a 3.5 kW, 45 000 rpm HS PMSM for a gas blower application. This machine has the prefabricated coils and its active length is just 22 mm. The second machine is an 11 kW, 31 200 rpm HS synchronous generator working in micro-Organic Rankine Cycle (ORC) power plant on the same shaft with the turbine. This machine has segmented stator and semi-closed slots. Both prototypes are built and the results of the measurements are presented and discussed.

II. Design

The design of an electrical machine begins with the general structural considerations and sizing equations, while the analysis of each design option starts with the analytical electromagnetic calculations, followed by the thermal and structural analyses. The next step is a verification of the gathered analytical results by Finite Element Method (FEM) analysis. The design process of an electrical machine is iterative and the number of steps depends on a number of restrictions to be met simultaneously. The number of these limitations is higher in a HS machinery compared to the conventional electrical machines.

Before the actual analytical calculations the structure of the machine must be defined during the feasibility study. The boundary conditions must be taken into account during this study. According to the shareholders, the costs of the machines under consideration should be minimal, whereas the electrical efficiency should remain high. In principal, the lowest possible amount of the stator slots enables the stator manufacturing cost reduction. The 3-slot PM motor with TC windings has high unbalance forces and higher rotor losses compared to the 6-slot PM motor [3]. Consequently, the 6-slot stator was selected for both developed HS machines. The 2-pole rotor was selected for the developed machines because it enables the lowest possible iron losses compared to the higher number of poles. The selection of the winding solution was executed according to the following overall competitive analysis.

A. Comparison of the DW and TC Winding Solutions

The machines with TC windings have several advantages, especially, short end windings turns, high copper space factor, low cogging torque, and, in some cases, a good fault tolerance [4]. The disadvantages of the TC windings, e.g., low winding

978-1-4799-1762-4/15/$31.00 ©2015 IEEE

TABLE I. LOSS DISTRIBUTION COMPARISON OF THE 11 KW MACHINE WITH DW AND TC WINDINGS

Losses Type	DW PMSM Losses, W	TC PMSM Losses, W
Copper losses	44	88
Stator Iron losses	78	100
Rotor Sleeve losses	15	34
Rotor Magnet losses	3	11
Additional losses	22	22
Mechanical losses	456	456
Total losses	618	711

factor, are of high significance in HS machines. The comparison of the DW with TC windings using multi-objective design method is presented, for instance, in [5]. To compare the winding solutions in this study two 11 kW PMSMs were designed with DW and TC windings while keeping the same rated power and rotational speed in the same volume. The number of slots per pole and phase in the DW machine, q, is equal to 2.

Table I shows the losses of the 11 kW PMSM with the DW and TC configurations, calculated using FEM. Both machines have the same rated output power and the rotational speed, therefore, the mechanical and the additional losses are identical.

The key difference between these two winding configurations in the considered machines is in the copper losses. For a TC solution the winding factor of the fundamental harmonic, k_{w1}, is just 0.5. It leads to the higher number of turns to produce the same current linkage as in the DW machine. The fundamental harmonic winding factor in the considered DW PMSM due to the short pitching is equal to 0.97. The end windings are significantly shorter in the TC type of windings. Moreover, by selecting the TC configuration, it is possible to implement the modular stator, which leads to a higher possible copper space factor. Taking into account all these considerations the analytical calculation of the winding resistance for both TC and DW topologies was made. As a result the stator phase resistance is higher in the TC winding machine compared to the DW machine. Consequently, the copper losses are 100 % higher with the TC winding topology as it is shown in Table I.

The next significant loss difference is in the rotors of the 11 kW machines. Both sleeve and magnet losses are higher in the TC winding machine because of the different harmonic content. The great impact of the slot harmonics on the rotor losses is shown in [6]. Normal flux density distributions in the air gap of the 11 kW PMSMs with DW and TC windings are shown in Fig. 1 and Fig. 2, respectively. In case of the TC configuration a 5^{th} and a 7^{th} harmonics are higher than the other harmonics. In case of the DW configuration an 11^{th} and a 13^{th} harmonics are higher than the other harmonics, which could be explained by the different number of stator slots, Q. In the TC solution Q is equal to 6 and in the DW machine $Q = 12$. The 5^{th} and the 7^{th} harmonics contribute more in the rotor losses due to their higher amplitude and lower number compared to the 11^{th} and the 13^{th} harmonics.

In spite of the significant difference in some loss components their share in the total loss distribution is low. As a result the total losses of the TC winding machine are just

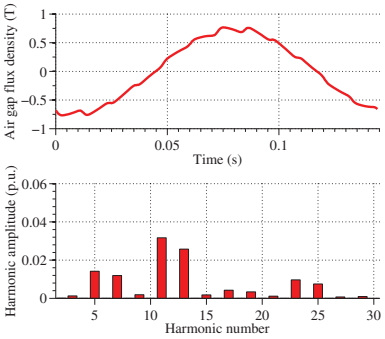

Fig. 1. Air gap normal flux density distribution and its harmonic content in the 11 kW DW PMSM.

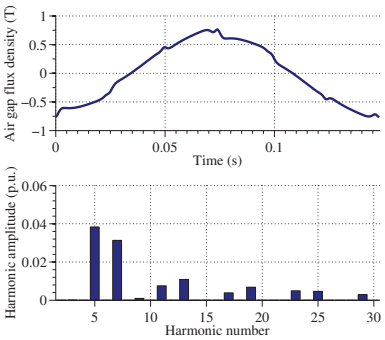

Fig. 2. Air gap normal flux density distribution and its harmonic content in the 11 kW TC PMSM.

15 % higher compared to the DW configuration. Here the advantages of the TC windings step forward. These machines offer shorter overall length of the system. Due to the shorter end winding's axial protrusion length, especially in a 2-pole machine, the 11 kW TC PMSM is 45.6 % shorter than the DW machine as it was shown in the previous study of this machine [7]. This significantly reduces the total rotor length, which, in turn, increases the natural frequencies and leads to the higher critical speeds of the TC machine. In the other words, the shorter rotor enables higher possible rotational speed in the undercritical operational mode.

The 11 kW machine is designed to work as a generator and it is installed on the same shaft with the turbine. The part of the working fluid flow, which runs through a turbine is also passing through the machine's stator slots, cooling down the windings directly. This cooling solution together with the low cost segmented stator was only possible with the TC winding configuration. Since the design of a HS machine is defined not solely by the electromagnetic performance, but the mechanics and the temperature distribution are playing the significant part, it was decided to use TC windings in both 3.5 kW and 11 kW

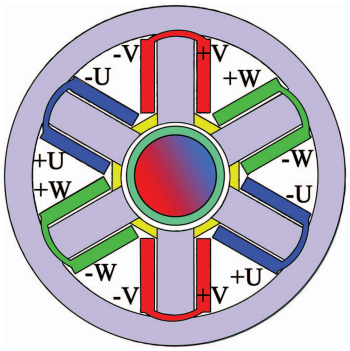

Fig. 3. 3.5 kW High-Speed Permanent Magnet Synchronous Motor geometry and TC winding configuration. The cylindrical PM is magnetized diametrically

machines.

B. The 3.5 kW and the 11 kW HS PMSMs Comparison

The developed prototypes have the similar topology. Fig. 3 shows the geometry and the winding configuration of the 3.5 kW machine. It is important to remember that in 2-pole PMSM the opposed TC windings have to be connected according to the scheme shown in Fig. 3 for the proper machine operation. Fig. 4 illustrates the flux density distribution and flux lines at the rated load in the 11 kW machine. The TC winding configuration of this machine is similar to the one, represented in Fig. 3.

The rotors of both machines consist of the full cylindrical permanent magnet, which is magnetized diametrically, and the magnet retaining sleeve. The PM is inserted inside the retaining sleeve by using a shrink-fitting technology. The interference fit between the PM and the sleeve is achieved by the materials relative size change after the assemblage. Before the assembly the retaining sleeve is heated and the PM is cooled. The temperature of the magnet will grow after the installation due to the heat exchange with the hot retaining sleeve. The condition of the magnet right after the assembly must be calculated and compared to the J, H-chart of the PM material to control the magnet irreversible demagnetization risk. To avoid this risk during the assembly, the retaining sleeve has been surrounded by the ferromagnetic material to provide the path for a PM flux and increase the load line angle. The magnet is made of the one piece to simplify the assembly process.

The key parameters of the designed machines are shown in Table II. The PM material is SmCo in both developed machines. The key reason for the selection of SmCo PM is dictated by the eddy-current losses in the magnet's retaining sleeve. SmCo can tolerate higher temperatures and, as a consequence, the machine has a higher possible working operating temperature without a risk of the irreversible demagnetization. Moreover, the PM demagnetization risk during the PM installation is minimal. Permanent magnet remanence is high in both machines which enables the high air gap flux density. The drawback of this material is the higher cost compared to NdFeB permanent magnet material.

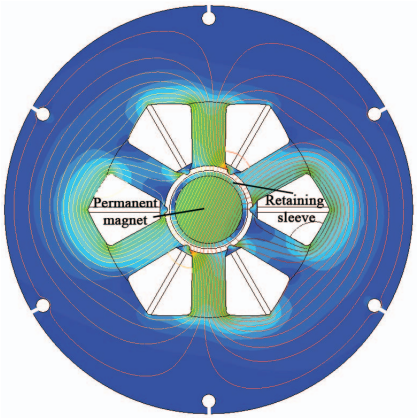

Fig. 4. 11 kW High-Speed Permanent Magnet Synchronous Machine flux density distribution and flux lines at the rated operational point

In spite of a similar topology, winding scheme, and SmCo magnet in the both examined machines, some components are made of different materials. The rotors of these machines have a hollow shaft, therefore, all the torque from the PMSM is transmitted to the shaft through the retaining sleeve. Moreover, the magnet's retaining sleeve must tolerate the stresses from the centrifugal forces and must keep the boundary contact with the magnet at all possible operation temperatures [8]. The selection of the retaining sleeve material is critical for the HS machine. The material has to have high resistivity, high yield strength and good thermal conductivity. The comparison of the different retaining sleeve materials for the HS machines is presented in [9], [10].

In case of the electrically conductive sleeve material the air gap flux density harmonics (Fig. 2) will cause the eddy-current losses in the retaining sleeve. These losses do not lead to the efficiency drop as it will be shown further, however the magnet is heated directly from the sleeve, which could cause the irreversible PM demagnetization.

The titanium retaining sleeve was selected for the 3.5 kW machine and the stainless steel sleeve was used in the 11 kW PMSM. The titanium has much higher yield strength and lower conductivity compared to the stainless steel and both materials have good thermal conductivity. The drawback of the titanium is the higher price compared to the stainless steel.

The materials selection influences the losses of the machine and to reduce them the geometry optimization is required. High permanent magnet remanence allowed to select air gap length equal to 5 mm and 5.5 mm in the 3.5 kW and in the 11 kW machines respectively. Such increased magnetic air gap length limits the air gap flux density variations due to both slot and current linkage harmonics and reduces eddy-current losses in the sleeves [11].

The laser cut stator stack lamination material NO10 was selected for the 3.5 kW machine due to its low per unit losses and thickness equal to 0.1 mm. These two factors enable low

TABLE II. DESIGNED MACHINES MAIN PARAMETERS

Machine parameter	3.5 kW PMSM	11 kW PMSM
Rated speed n_n, min^{-1}	45 000	31 200
Number of poles p	2	2
Number of stator slots Q_s	6	6
Rated torque T_n, Nm	0.74	3.36
Rotor outer diameter D_o, m	0.039	0.046
Physical air-gap legth δ, m	0.002	0.003
External diameter D_e, m	0.140	0.242
Active length l, m	0.022	0.060
Permanent magnet material	SmCo	SmCo
Permanent magnet remanence B_r, T	1.10	1.12
Retaining sleeve material	Titanium	Stainless steel
Stator stack lamination material	NO10	M-270-35A
Magnetic wedges material	Spindurol	Magnoval 2067
Bearing type	Magnetic bearing	Ball bearing

iron losses in the 3.5 kW machine. The drawbacks of the NO10 material are the high price and low stack fill factor. The lamination for stator stack of the 11 kW machine was also laser cut because of the complex geometry and the material for this machine is M-270-35A. During the FEM analysis this 0.35 mm thick material has shown an acceptable loss level at 520 Hz, which is the 11 kW machine's rated frequency. This material is easily available and has lower price compared to NO10.

The installation of the magnetic wedges between the tooth tips in both machines decreases the slot harmonics in the air gap, which, in turn, reduces the rotor eddy-current losses. Both utilized materials Spindurol and Magnoval 2067 have the relative permeability about 2.5 at 0.7 T because of the iron powder in their composition. The detailed analysis of the rotor loss reduction due to the magnetic wedges installation in the developed 11 kW PMSM could be found in [12].

The stator prototype of the 3.5 kW HS PMSM is shown in Fig. 5 (a). This machine is made open slot to allow the utilization of the prefabricated windings. The copper space factor is low in this machine as very few turns are needed and the copper losses are not dominant in this case.

Several modifications of the HS machine topology were made in the 11 kW machine compared to 3.5 kW PMSM. The photo of the 11 kW HS PMSM stator is shown in Fig. 5 (b). First of all, the analysis of the similar HS machine with 6 slots and 2 poles has shown, that the eddy-current losses are getting lower according to the increasing of the tooth tip width [13]. Therefore, the semi-closed slots were selected in the 11 kW prototype. To simplify the winding work and manufacturing process the stator is made segmented. This kind of stator together with TC windings allows to prepare prefabricated segments where the phase windings are isolated both electrically and magnetically which increase the fault tolerance of the machine [14].

The second distinction of the 11 kW PMSM is the exceptionally thick stator yoke. This is done to reduce the total iron losses in the machine. The detailed optimization procedure is described in [7]. To avoid the extra eddy-current losses in the stack fixation end plates they were implemented as the rings on the outer diameter of the stator stack. The fixation of the stator segment's teeth part is done by the slot insulation covered by the impregnated tooth coils.

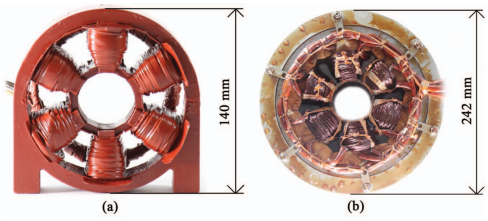

Fig. 5. Stator prototypes of the 3.5 kW HS PMSM (a), and the 11 kW HS PMSM (b). The copper space factor is low in both machines as very few turns are needed in the 3.5 kW machine and to provide the space for the cooling fluid in the 11 kW machine.

III. LOSS ANALYSIS

The precise loss calculations are very important in the HS machines with the permanent magnets. The rotor loss distribution affects the PM demagnetization risk during the machine operation. Because of the limited volume the stator losses have to be calculated accurately to design the efficient and effective cooling system which will allow a safe machine operation.

A. Copper Losses

The copper losses in an electrical machine may be increased due to the combination of the following phenomena: skin effect, proximity effect, and eddy-currents inside the conductors due to the rotating magnetic field of PM [15]. These effects are especially significant at the high-speed, when the frequency is high. To minimize above mentioned phenomena a number of arrangements is implemented in the designed HS PMSMs.

The diameter of the single round wire must be equal or smaller than the skin depth at the machine's operating frequency. The single conductor diameter is equal to 1 mm in the designed machines, which is lower than the calculated skin depths at the rated frequencies. This prevents an increase of the stator winding resistance due to the skin effect.

However, the total magnetic field in the slot is larger than the one single conductor field, especially, close to the slot opening. Hence, the proximity effect dominates over the skin effect in the HS machines. A well-known technique to reduce the copper losses is to transpose the coils along the slot. For example, Litz-wires could be utilized to minimize the proximity effect. Nevertheless, this type of windings is an expensive solution. Another, cheaper option is the twisted bundles. This solution was implemented for the 11 kW PMSM to reduce the copper losses due to the proximity effect. According to [16], the single 360 degrees twist per stack length is sufficient.

The installation of the magnetic wedges between the tooth tips is shielding the windings and reduces the conductors eddy-currents due to the rotating PM magnetic field.

To sum up, the magnetic wedges installation, single conductor diameter limitation and the twisted bundles tend to

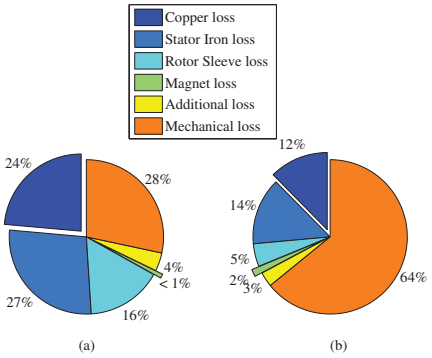

Fig. 6. Loss distribution of the 3.5 kW PMSM (a), and the 11 kW PMSG (b)

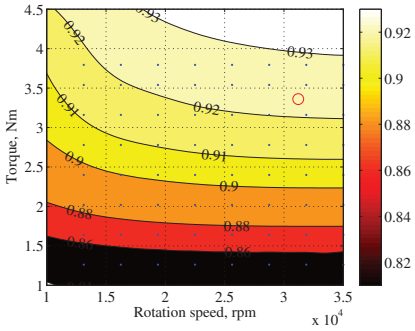

Fig. 7. Calculated efficiency map of the 11 kW HS PMSM

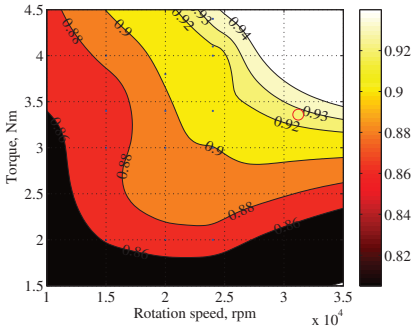

Fig. 8. Measured efficiency map of the 11 kW HS PMSM

decrease the AC resistance increase phenomena and reduce the extra copper losses in the designed machines.

B. Prototypes Loss Distribution Comparison

Fig. 6 shows the pie charts of the loss distribution at the rated operational point in the 3.5 kW and the 11 kW machines. In both developed machines the ratio between the iron and copper losses is close to 1, which is the rule of thumb in the design of an electrical drive system. The rotor losses form about 17 % of the total losses in the 3.5 kW PMSM, whereas the 11 kW PMSM rotor losses form just 7 % of the total losses. The 11 kW PMSM tooth tip zone optimization, for instance, the usage of the semi-closed slots together with the sleeve thickness decrease, significantly reduces the rotor losses even with the stainless steel PM retaining sleeve.

In a HS machine the mechanical losses dissipated by the bearings usually form the greatest share [17]. In Fig. 6 (b) it is clearly seen that the mechanical losses are dominant in the 11 kW machine. Whilst in the 3.5 kW machine copper, iron, mechanical and rotor losses are about equal. The significant mechanical loss reduction in the 3.5 kW PMSM is achieved by implementing the Active Magnetic Bearings (AMBs). The extra losses in the AMBs are not taken into account in Fig. 6 (a).

C. Calculated Efficiency Map

During the analysis of the 11 kW machine the efficiency map was calculated. Fig. 7 shows the calculated efficiency map, based on the FEM model of the machine. There are 100 calculation points, which cover the rotational speeds, n, from 10 to 35 krpm with the load torque, T, from 1 to 4.5 Nm. The machine's rated operating point is at $n = 31\,200$ rpm and $T = 3.36$ Nm.

The copper losses are proportional to the phase current and, consequently, to the load torque. Hence, the circuit with the current sources was implemented in the FEM model to ensure the steady magnetic state. The copper losses were calculated using the phase resistance, which was verified by the stator winding resistance measurements.

The eddy-current rotor losses were calculated separately for the sleeve and for the PM. To evaluate the amount of losses in FEM software the PM and sleeve were represented as the solid conductors and connected in parallel to the large resistors to simulate the short circuit.

The iron losses were calculated using FEM software. To implement the methods utilized in the software, it is necessary to know the coefficient of the magnetic losses by hysteresis k_{h} and the coefficient of the magnetic losses in excess k_{e}. These coefficients are frequency dependent and were acquired for the every calculated frequency by analysing the lamination manufacturer's data. The mechanical losses were calculated analytically by following the method described in [18].

IV. Experiments

The measurements of the developed 11 kW machine were not possible in the final micro-ORC turbine installation. Thereby, a separate measurement setup was assembled. This setup includes the 11 kW PMSM with forced air cooling, a water cooled eddy-current brake and a coupling between them.

During the measurements the machine was working as a motor and was supplied by the frequency converter. The input power was measured by the power analyzer and the output power was measured by the eddy-current brake.

The difference between the input and output power formed the efficiency map which is shown in Fig. 8. The actual losses in the low speed area are higher than the calculated ones as it is seen in Fig. 7. The extra losses in the coupling could explain this difference, as these losses were not included in the calculations. This assumption is supported by the significant calculated and measured loss difference at the no-load.

In the high-speed area the measurement and calculation results are relatively equal. For example, at the rated operating point, which is marked with the circle, the efficiency difference is below 1 %. Thereby, the tooth tip zone optimization, utilization of the magnetic wedges, and the wingding arrangements are successfully limit the losses of the 11 kW machine.

The overall efficiency of the designed machine at the rated point is about 92 % in the test setup. The utilization of the other type of bearings in the final installation should significantly increase the overall efficiency as the mechanical losses form 64 % of the total losses.

V. Conclusion

This paper describes a low-cost topology for the high-speed low-power machines. This topology includes a 2-pole rotor with the diametrically magnetized PM inside the retaining sleeve, a 6-slot stator with the Tooth-Coil windings. The motivation for the selection of the implemented rotor and stator structures and the TC winding configuration is given.

The comparison of the winding solutions has shown that the total losses are higher with the TC winding configuration compared to the DW machine. However, in many HS applications the TC winding selection is beneficial because of the shorter overall length of the rotor.

The proposed topology is tested with the two manufactured prototypes. The key parameters of the machines are presented and their similarities and differences are discussed. The different approaches to the loss minimization of the topology under consideration are studied. Better materials were used in the 3.5 kW HS PMSM, whereas the alternative geometry optimization was performed in the 11 kW machine. The benefits and drawbacks of these approaches are discussed.

The winding arrangements that enable to limit the AC resistance increase in the developed prototypes are described. The reduction of the different loss components due to the magnetic wedges installation is highlighted.

The design considerations and the calculation methods are verified by the prototype testing. According to the test results the PMSM with a full cylindrical magnet rotor and the TC windings are suitable for the HS machinery in case of the precise electromagnetic, mechanical and thermal design and its further optimization.

References

[1] D. Gerada, A. Mebarki, N. Brown, C. Gerada, A. Cavagnino, and A. Boglietti, "High-speed electrical machines: Technologies, trends, and developments," *Industrial Electronics, IEEE Transactions on*, vol. 61, no. 6, pp. 2946–2959, June 2014.

[2] A. Tenconi, S. Vaschetto, and A. Vigliani, "Electrical machines for high-speed applications: Design considerations and tradeoffs," *Industrial Electronics, IEEE Transactions on*, vol. 61, no. 6, pp. 3022–3029, June 2014.

[3] T. Noguchi, Y. Takata, Y. Yamashita, Y. Komatsu, and S. Ibaraki, "220,000-r/min 2-kW PM motor drive for turbocharger," *Industrial Applications, IEEJ Transactions on*, vol. 125, no. 9, pp. 854–861, Sept 2005.

[4] A. EL-Refaie, "Fractional-slot concentrated-windings synchronous permanent magnet machines: Opportunities and challenges," *Industrial Electronics, IEEE Transactions on*, vol. 57, no. 1, pp. 107–121, Jan 2010.

[5] Y. Duan, R. Harley, and T. Habetler, "Method for multi-objective optimized designs of surface mount permanent magnet motors with concentrated or distributed stator windings," in *Electric Machines and Drives Conference. IEMDC. IEEE International*, 2009, pp. 323–328.

[6] E. Fornasiero, N. Bianchi, and S. Bolognani, "Slot harmonic impact on rotor losses in fractional-slot permanent-magnet machines," *Industrial Electronics, IEEE Transactions on*, vol. 59, no. 6, pp. 2557–2564, June 2012.

[7] N. Uzhegov, J. Pyrhönen, and S. Shirinskii, "Loss minimization in high-speed permanent magnet synchronous machines with tooth-coil windings," in *Industrial Electronics Society, IECON 2013 - 39th Annual Conference of the IEEE*, Nov 2013, pp. 2960–2965.

[8] A. Borisavljevic, H. Polinder, and J. Ferreira, "On the speed limits of permanent-magnet machines," *Industrial Electronics, IEEE Transactions on*, vol. 57, no. 1, pp. 220–227, Jan 2010.

[9] W. Li, H. Qiu, X. Zhang, J. Cao, and R. Yi, "Analyses on electromagnetic and temperature fields of superhigh-speed permanent-magnet generator with different sleeve materials," *Industrial Electronics, IEEE Transactions on*, vol. 61, no. 6, pp. 3056–3063, June 2014.

[10] W. Li, H. Qiu, X. Zhang, J. Cao, S. Zhang, and R. Yi, "Influence of rotor-sleeve electromagnetic characteristics on high-speed permanent-magnet generator," *Industrial Electronics, IEEE Transactions on*, vol. 61, no. 6, pp. 3030–3037, June 2014.

[11] P.-D. Pfister and Y. Perriard, "Very-high-speed slotless permanent-magnet motors: Analytical modeling, optimization, design, and torque measurement methods," *Industrial Electronics, IEEE Transactions on*, vol. 57, no. 1, pp. 296–303, Jan 2010.

[12] N. Uzhegov, E. Kurvinen, and J. Pyrhönen, "Design limitations of 6-slot 2-pole high-speed permanent magnet synchronous machines with tooth-coil windings," in *Power Electronics and Applications (EPE'14-ECCE Europe), 2014 16th European Conference on*, 2014, pp. 1–7.

[13] K. Shigematsu, J. Oyama, T. Higuchi, T. Abe, and Y. Ueno, "The study of eddy current in rotor and circuit coupling analysis for small size and ultra-high speed motor," in *Power Electronics and Motion Control Conference, 2004. IPEMC 2004. The 4th International*, vol. 1, 2004, pp. 275–279.

[14] F. Magnussen and H. Lendenmann, "Parasitic effects in PM machines with concentrated windings," *Industrial Applications, IEEE Transactions on*, vol. 43, no. 5, pp. 1223–1232, Sept 2007.

[15] R. Wojda and M. Kazimierczuk, "Analytical optimization of solid-round-wire windings," *Industrial Electronics, IEEE Transactions on*, vol. 60, no. 3, pp. 1033–1041, March 2013.

[16] M. van der Geest, H. Polinder, J. Ferreira, and D. Zeilstra, "Current sharing analysis of parallel strands in low-voltage high-speed machines," *Industrial Electronics, IEEE Transactions on*, vol. 61, no. 6, pp. 3064–3070, June 2014.

[17] T. Noguchi and M. Kano, "Development of 150000 r/min, 1.5 kW permanent-magnet motor for automotive supercharger," in *Power Electronics and Drive Systems, 2007. PEDS '07. 7th International Conference on*, Nov 2007, pp. 183–188.

[18] J. Pyrhönen, T. Jokinen, and V. Hrabovcova, *Design of Rotating Electrical Machines*. Chichester, UK: John Wiley & Sons, 2008.

Publication V

Uzhegov, N., Kurvinen E., Nerg, J., Pyrhönen, J., Sopanen, J., and Shirinskii, S.
Multidisciplinary Design Process of a 6-Slot 2-Pole High-Speed Permanent Magnet Synchronous Machine

Reprinted with permission from
IEEE Transactions on Industrial Electronics,
vol. 63, no. 2, pp. 784–795, Feb. 2016

Multidisciplinary Design Process of a 6-Slot 2-Pole High-Speed Permanent-Magnet Synchronous Machine

Nikita Uzhegov, *Member, IEEE*, Emil Kurvinen, Janne Nerg, *Senior Member, IEEE*, Juha Pyrhönen, *Member, IEEE*, Jussi T. Sopanen, *Member, IEEE*, and Sergey Shirinskii, *Member, IEEE*

***Abstract*—High-speed permanent-magnet synchronous machines (HS PMSMs) are a popular topology among modern electrical machines. Suitable applications for such machines are low-power vacuum pumps, compressors, and chillers. This paper describes a systematic design methodology for an HS PMSM using two case studies. The design process for such high-speed (HS) machines is multidisciplinary and highly iterative due to the complex interaction of the many design variables involved. Consequently, no single optimum solution exists, and multiple possible solutions can meet the customer requirements. Practical solutions should be within acceptable thermal limits, should be energy-efficient, and should be rigid enough to withstand the forces exerted during operation. The proposed design flow is divided into steps that are presented in this paper in the form of a flowchart with emphasis on mechanical aspects. Each step represents a task for a thermal, mechanical, or electrical engineer. The features of each step and the prerequisites for moving to the next step are discussed. The described methodology was implemented in the design of two HS PMSMs. The output performance results of the design flow are compared with measured results of the prototypes. The design process described in this paper provides a straightforward procedure for the multidisciplinary design of HS permanent magnet electrical machines.**

***Index Terms*—AC machine, electrical design, high-speed (HS) drive, mechanical design, permanent-magnet (PM) machines, rotating machines.**

Manuscript received April 16, 2015; revised June 16, 2015; accepted August 9, 2015. Date of publication September 10, 2015; date of current version January 8, 2016.

N. Uzhegov, J. Nerg, and J. Pyrhönen are with the Department of Electrical Engineering, LUT Energy, School of Energy Systems, Lappeenranta University of Technology, 53851 Lappeenranta, Finland (e-mail: nikita.uzhegov@lut.fi; janne.nerg@lut.fi; juha.pyrhonen@lut.fi).

E. Kurvinen and J. T. Sopanen are with the Department of Mechanical Engineering, School of Energy Systems, Lappeenranta University of Technology, 53851 Lappeenranta, Finland (e-mail: emil.kurvinen@lut.fi; jussi.sopanen@lut.fi).

S. Shirinskii is with the Institute of Electrical Engineering, Moscow Power Engineering Institute, 111250 Moscow, Russia (e-mail: shirinskiisv@gmail.com).

Color versions of one or more of the figures in this paper are available online at http://ieeexplore.ieee.org.

Digital Object Identifier 10.1109/TIE.2015.2477797

I. Introduction

HIGH-SPEED (HS) electrical machines represent well-established technology and are used in a number of common industrial applications. HS machines provide benefits such as high power density, small footprint, and high overall system efficiency. One reason for these advantages is that HS technology enables direct coupling between the HS electrical machine and the working machine, which makes it possible to avoid the requirement for a gearbox. The benefits inherent to such machines have attracted the attention of manufacturers producing, for example, gas compression appliances, turbines, air blowers, vacuum pumps, machine tools, and spindle drives [1], [2], and the market for HS machinery has shown exceptional growth over the last decade. This active interest in HS machinery has led to a rise in the number of joint projects between academia and industry [3].

From the design point of view, HS technology is challenging, and a lot of research is ongoing regarding efficient and effective solution development [4]. Successful design and operation of an HS machine require that multiple design issues be reviewed simultaneously [5]. In many applications, mechanical stresses limit the performance of the HS electrical machine, and thus, HS topologies are sometimes defined by the mechanical and thermal limitations.

It is not generally possible to use a standard structure, and each machine needs to be designed according to the specific requirements of the application. Consequently, the design process of an HS machine involves several steps prior to construction of the first prototype. Arkkio *et al.* [6] proposed a design methodology for HS induction machines (HSIMs) and HS permanent-magnet synchronous machines (HS PMSMs). However, the methodology did not include rotordynamics analysis. An improved design methodology was implemented in [7] to define the maximum power and speed limits for an HS PMSM. Ranft [8] proposed a design methodology chart for HSIM but did not include thermal analysis in the methodology. Cheng *et al.* [9] proposed a design flowchart for HS PMSM with the full cylindrical magnet in the rotor. However, the flowchart included only electrical and mechanical designs, and the thermal analysis was done separately. Bernard *et al.* [10] proposed a design flow and analytical optimization for PMSM with a gearbox. The design flow was for a screwdriver application with infinite stiff

supports, which limits its implementation for HS machinery. Although several design methodologies are presented in the literature, none of them proposes a comprehensive multidisciplinary design process for HS applications that includes electrical, mechanical, and thermal analyses.

To limit the number of possible options, the design methodology presented in this paper was developed for a specific type of HS electrical machine. The machines under consideration have six stator slots and two poles, which, in a three-phase machine, result in the number of slots per pole and phase $(q = 1)$. The machines utilize tooth-coil (TC) windings to have the shortest possible overall length of a two-pole machine. This naturally leads to a shorter rotor total length, which, in turn, expands the mechanical boundaries with respect to critical speeds. With a shorter rotor, the lowest flexible natural frequencies of the rotor will be higher, and as a result, the machine operates below critical speed, enabling still higher operational speeds.

The design process is explained and applied to two machines. The developed prototypes use different approaches within the scope of the presented design methodology. The first machine under consideration is a 3.5-kW 45 000-r/min PMSM for a gas blower application. In this machine, expensive materials are selected to reduce losses and ensure mechanical rigidity and acceptable temperatures. The second machine is a PM generator with a rated operating point of 11 kW at 31 200 r/min. The machine works as a generator in a micro-organic Rankine cycle power plant. The machine has the same topology as the first machine but utilizes inexpensive materials. To reduce high losses, alternative geometry optimization solutions are implemented in the second machine.

The developed prototypes are built and tested. The machines' performance calculation results are compared to the test results, and conclusion is drawn regarding the suitability of the design methodology for other types of HS electrical machines.

The main contribution of this paper is to propose a multidisciplinary design process for a PMSM consisting of six stator slots and two poles as well as a diametrically magnetized PM and a TC wound stator in HS applications. Even though the proposed design procedure is intended for the aforementioned PMSM type, it can be applied, with slight modifications, to other electrical machine types.

II. Design Process

The design process of an HS machine involves several steps prior to construction of the first prototype. Fig. 1 shows a general design flowchart for an HS PMSM. The design process is divided into nine steps. These steps are tasks for engineers and all have input and output design variables. Each of the steps should yield results that satisfy the design requirements (step 1). The flowchart has six decision points where the fulfillment of the requirement list is verified. If the requirements are not met, then a new iteration round is required. Each step creates additional information and introduces further requirements, e.g., in step 2, a maximum shaft diameter can be evaluated from the initial requirements. If all of the requirements are fulfilled, the process can proceed to the next step; otherwise, the design should be changed until satisfactory results are achieved. In Fig. 1, the proposed actions to satisfy the additional requirements are shown at the right side. When all of the steps are completed and the design requirements are fulfilled, the first prototype can be built.

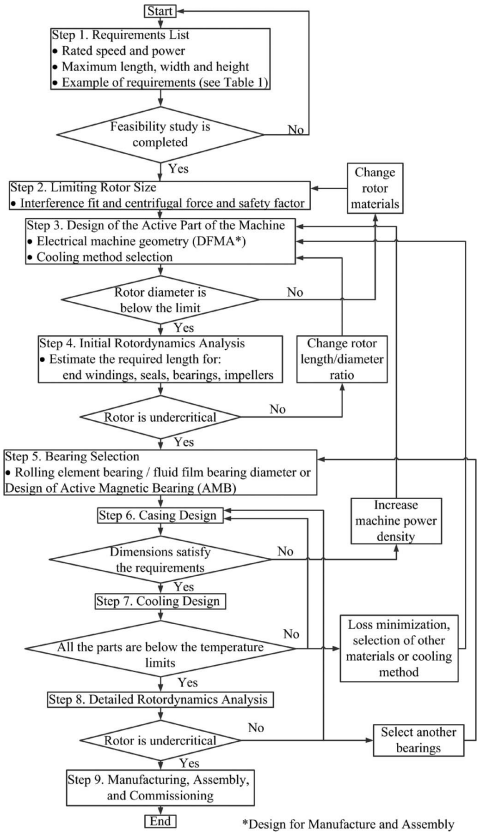

Fig. 1. Design flowchart for an HS PMSM.

The design process of an electric machine is thus a highly iterative process, and for that reason, many concepts need to be analyzed before the final solution is found. The required calculations can first be done with analytical electromagnetic, thermal, and structural analyses in order to constrain the dimensions. The constrained dimensions can then be used as a starting point in subsequent steps. Finite-element method (FEM) analysis can be used in the verification or to study the structure in more detail.

The proposed design process is specially developed and tested for an HS PMSM having six slots and two poles. The decision to consider a specific type of machine was made in order to limit the machine topology design variations, simplify the initial design stage, and concentrate on the special features

of the proposed machine topology. The selected electrical machine topology is justified with the following reasons.

First, one of the boundary conditions of the design was reasonable manufacturing costs. This was taken into account in the design flow. The topology with the lowest possible slot number allows, in principle, cost effectiveness in manufacturing. Noguchi *et al.* [11] compared a three-slot motor to a six-slot motor with TC windings for an HS application. According to their results, a three-slot motor has high unbalanced forces and higher rotor losses compared to a six-slot motor. Consequently, a six-slot stator was selected for both HS machines developed in this work. Second, the machines have two poles, and thereby, the iron losses are lower compared to solutions with a higher number of poles at the considered operational frequencies. Finally, TC windings were selected to achieve a reasonable solution for short end winding axial protrusion length.

TC windings may be criticized in this kind of application because the fundamental winding factor is greatly reduced by the very narrow winding step. The winding factor is only $k_{w1} = 0.5$, while in the case of a full pitch $q = 1$ winding, it is $k_{w1} = 1$. However, in HS machines, the number of winding turns is often so low that doubling them does not significantly harm machine performance. Indeed, the amount of copper can be about the same in TC windings and full pitch windings as the full pitch winding ends are so long compared to the compact end windings in the case of TC windings. However, even if copper losses increase due to the higher number of turns, their share in the total loss distribution is negligible compared to other losses, as will be shown later. Iron and rotor losses are increased with TC windings due to the higher air gap harmonic content compared to distributed windings (DWs). An alternative solution which enables short end winding axial protrusion length is Gramme ring windings [12].

The nine design steps (see Fig. 1) are explained in detail in the following sections.

A. Step 1. Requirement List

The requirement list contains all of the requirements and wishes that the final product should and could fulfill. At the beginning of the design process, several parameters and values need to be defined in order to achieve fluent design flow. The requirement list can be updated after each step, e.g., when the maximum rotor diameter has been defined. Table I shows an example of a requirement list. In addition to the electrical, mechanical, and thermal information of the type shown in Table I, the requirement list should include other information such as sealing information and requirements originating from applicable industrial standards, e.g., the required degree of protection against intrusions in the casing.

After the design engineers have studied the requirement list, they have to prepare the specifications. The specifications must be based on a system feasibility study. In the specifications, extra technical information regarding the system may be added. When the feasibility study has been completed, it is possible to move to step 2.

TABLE I
EXAMPLE OF REQUIREMENT LIST

Requirement/Wishes	Requirement	Wish
Rated speed	31 200 rpm	-
Nominal power	11 kW	-
Efficiency at nominal point	> 90 %	> 95 %
Axial length	< 150 mm	< 130 mm
Bearing type	Ball bearing	-
Mechanical safety factor	2.0	-
Thermal class	155	120
Cooling method	Liquid	-
Rotor material	Austenitic steel	-
Rotordynamics	Undercritical	-
IP class	IP55	-
Manufacturing price per unit	$< 25\,000$ EUR	$< 15\,000$ EUR
Maintenance period	2 years	-

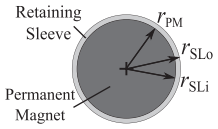

Fig. 2. Rotor structure with the dimensions used in the shrink fit calculation.

It should be noted that the magnet material was not defined in the requirement list for the prototypes in this study. Information about the PM material is required to set the maximum shaft diameter in step 2. If the magnet material is not defined in the requirement list, the next step could be evaluation with commonly used neodymium (NdFeB)- and samarium-cobalt (SmCo) magnets. Furthermore, in step 3, the required thermal class directly affects the magnet material selection.

B. Step 2. Limiting Rotor Size

The aim of the second step is to determine the limits on rotor size for rotation at the nominal speed with a required safety factor. As the rotation speed increases, the centrifugal force creates greater stresses on the structure, and the maximum diameter can be determined based on the properties of the used material. In the proposed design process, a rotor structure with a full cylindrical magnet and a retaining sleeve is implemented. Fig. 2 illustrates the cross section of the rotor structure.

In most cases, the sleeve material used should be austenitic steel or another nonmagnetic material to avoid PM flux leakage and additional eddy-current losses. Contact between the magnet and sleeve should be maintained at all times. In practice, this means that the interference fit should be maintained for all operation conditions while simultaneously ensuring a large enough safety margin relative to the yield strength of the material.

The PM material is affected by the expansion of the centrifugal forces and, in the case of the SmCo material, the temperature increase. The NdFeB PM material has a negative thermal expansion coefficient perpendicular to the magnetization direction, which causes magnet contraction as the rotor

temperature rises. The sleeve is affected by the expansion due to the centrifugal forces and increasing temperature [13].

The total expansion of the magnet and the sleeve ($\varepsilon_{\mathrm{PM}}$ and $\varepsilon_{\mathrm{SL}}$) can be calculated by considering the expansion due to rotation speed ($\varepsilon_{\mathrm{PM}\Omega}$ and $\varepsilon_{\mathrm{SL}\Omega}$) together with the expansion due to thermal expansion ($\varepsilon_{\mathrm{PMtemp}}$ and $\varepsilon_{\mathrm{SLtemp}}$) as

$$\begin{aligned}\varepsilon_{\mathrm{PM}}(r) &= \varepsilon_{\mathrm{PM}\Omega} + \varepsilon_{\mathrm{PMtemp}} \\ &= \frac{3+\nu_{\mathrm{PM}}}{8}\rho_{\mathrm{PM}}\Omega^2\frac{1-\nu_{\mathrm{PM}}}{E_{\mathrm{PM}}}r\left[{r_{\mathrm{PM}}}^2 - \frac{1+\nu_{\mathrm{PM}}}{3+\nu_{\mathrm{PM}}}r^2\right] \\ &\quad + \alpha_{\mathrm{PM}} r \Delta T \\ \varepsilon_{\mathrm{SL}}(r) &= \varepsilon_{\mathrm{SL}\Omega} + \varepsilon_{\mathrm{SLtemp}} \\ &= \frac{3+\nu_{\mathrm{SL}}}{8}\rho_{\mathrm{SL}}\Omega^2\frac{1-\nu_{\mathrm{SL}}}{E_{\mathrm{SL}}}r \\ &\quad \times \left[r_{\mathrm{SLi}}^2 + r_{\mathrm{SLo}}^2 - \frac{1+\nu_{\mathrm{SL}}}{3+\nu_{\mathrm{SL}}}r^2 + \frac{1+\nu_{\mathrm{SL}}}{1-\nu_{\mathrm{SL}}}\frac{r_{\mathrm{SLi}}^2 r_{\mathrm{SLo}}^2}{r^2}\right] \\ &\quad + \alpha_{\mathrm{SL}} r \Delta T \end{aligned} \tag{1}$$

where r is the radius from the center from which the expansion is calculated, subscripts PM and SL refer to the magnet and sleeve, respectively, ν is the Poisson's ratio of the given material, ρ is the material density, Ω is the rotation speed, E is the modulus of elasticity, r_{PM} is the magnet radius, r_{SLi} is the sleeve inner radius and r_{SLo} is the sleeve outer radius, α is the thermal expansion coefficient, and ΔT is the temperature difference from room temperature. The temperature value is selected close to the PM material operation limit to ensure reliable operation at critical conditions. The temperature is updated after the detailed thermal analysis is performed in step 7 and the next design iteration begins. The dimensions are shown in Fig. 2.

In an HS PMSM, the magnet and sleeve should be fixed in a way that the produced torque is transmitted to the rotor shaft. This is usually done by manufacturing the sleeve smaller than the magnet outer diameter and utilizing the temperature difference to install the sleeve over the magnet, the so-called shrink fit or interference fit. The interference fit between the magnet and sleeve should be selected so that neither the yield strength of the magnet nor the sleeve is exceeded, nor the maximum temperature of the PM. The dynamical interference fit λ can be calculated by considering the total expansion calculated in (1) and reducing that amount from the designed static interference fit $\varepsilon_{\mathrm{sinterf}}$ amount as $\lambda = \varepsilon_{\mathrm{PM}} + \varepsilon_{\mathrm{SL}} - \varepsilon_{\mathrm{sinterf}}$. The dynamic contact pressure between the magnet and the sleeve p_c can be calculated as (2), shown at the bottom of the page.

The stresses due to the rotation speed, thermal effect, and pressure from the interference fit are highest at the contact point between the magnet and the sleeve. Tangential (t) and radial (r) stresses can be calculated as a function of r based on the contact pressure, rotation of the magnet and sleeve as

$$\begin{aligned}\sigma_{\mathrm{rc}} &= \frac{r_{\mathrm{SLi}}^2 p_c - r_{\mathrm{SLo}}^2 p_o}{r_{\mathrm{SLo}}^2 - r_{\mathrm{SLi}}^2} - \frac{r_{\mathrm{SLi}}^2 r_{\mathrm{SLo}}^2 (p_s - p_o)}{r^2\left(r_{\mathrm{SLo}}^2 - r_{\mathrm{SLi}}^2\right)} \\ \sigma_{\mathrm{tc}} &= \frac{r_{\mathrm{SLi}}^2 p_c - r_{\mathrm{SLo}}^2 p_o}{r_{\mathrm{SLo}}^2 - r_{\mathrm{SLi}}^2} + \frac{r_{\mathrm{SLi}}^2 r_{\mathrm{SLo}}^2 (p_s - p_o)}{r^2\left(r_{\mathrm{SLo}}^2 - r_{\mathrm{SLi}}^2\right)} \\ \sigma_{\mathrm{rPM}\Omega} &= \frac{3+\nu_{\mathrm{PM}}}{8}\rho_{\mathrm{PM}}\Omega^2[r_{\mathrm{PM}} - r^2] \\ \sigma_{\mathrm{tPM}\Omega} &= \frac{3+\nu_{\mathrm{PM}}}{8}\rho_{\mathrm{PM}}\Omega^2\left[r_{\mathrm{PM}} - \frac{1+3\nu_{\mathrm{PM}}}{3+\nu_{\mathrm{PM}}}r^2\right] \\ \sigma_{\mathrm{rSL}\Omega} &= \frac{3+\nu_{\mathrm{SL}}}{8}\rho_{\mathrm{SL}}\Omega^2\left[r_{\mathrm{SLi}}^2 + r_{\mathrm{SLo}}^2 - r^2 - \frac{r_{\mathrm{SLi}}^2 r_{\mathrm{SLo}}^2}{r^2}\right] \\ \sigma_{\mathrm{tSL}\Omega} &= \frac{3+\nu_{\mathrm{SL}}}{8}\rho_{\mathrm{SL}}\Omega^2\left[r_{\mathrm{SLi}}^2 + r_{\mathrm{SLo}}^2 - \frac{1+3\nu_{\mathrm{SL}}}{3+\nu_{\mathrm{SL}}}r^2 + \frac{r_{\mathrm{SLi}}^2 r_{\mathrm{SLo}}^2}{r^2}\right] \end{aligned} \tag{3}$$

where p_o is the pressure in the electrical machine (air). Using the superposition theorem, the radial and tangential stresses in the sleeve can be summed into $\sigma_{\mathrm{rtot}} = \sigma_{\mathrm{rc}} + \sigma_{\mathrm{rSL}\Omega}$ and $\sigma_{\mathrm{ttot}} = \sigma_{\mathrm{tc}} + \sigma_{\mathrm{tSL}\Omega}$, and the von Mises stress can then be calculated as $\sigma_{\mathrm{vmises}} = \sqrt{\sigma_{\mathrm{ttot}}^2 - \sigma_{\mathrm{ttot}}\sigma_{\mathrm{rtot}} + \sigma_{\mathrm{rtot}}^2}$ [14].

C. Step 3. Design of the Active Part of the Machine

Once the maximum rotor outer diameter has been defined, electromagnetic design can be commenced. Based on the requirement list and stress analysis information, the initial rotor diameter and length are calculated. The length/diameter ratio χ is a parameter that strongly affects the final machine design performance because the electrical machine rotor length influences the rotordynamics and the rotor diameter influences the mechanical losses [15].

It is important to remember at this stage that the actual rotor length in a PM machine must be selected such that it is longer than in a machine with winding-created current linkage. To utilize the armature optimally and to avoid performance drop, the PM length l_{PM} should be selected as $l_{\mathrm{PM}} \approx l + 2\delta_e$, where l is the physical length of the stator stack and δ_e is the magnetic air gap length [16]. In other words, the PM rotor length must be at least two magnetic air gaps longer than the stator core length.

The analytical electromagnetic design process follows the procedure described in [13]. The different optimization techniques for PMSMs can be found in [17]. During the machine electromagnetic design, the stator and the rotor are calculated simultaneously. The stator part itself is not critical in the further rotordynamics analysis. However, the end winding axial protrusion length will affect the total rotor length and the rotordynamics.

$$p_c = \frac{\lambda r_{\mathrm{PM}} E_{\mathrm{PM}} E_{\mathrm{SL}}\left(r_{\mathrm{PM}}^2 - r_{\mathrm{SLo}}^2\right)}{\left(\left(r_{\mathrm{PM}}^4 - r_{\mathrm{PM}}^2 r_{\mathrm{SLo}}^2\right)\nu_{\mathrm{SL}} - r_{\mathrm{PM}}^4 - r_{\mathrm{PM}}^2 r_{\mathrm{SLo}}^2\right)E_{\mathrm{PM}} + \left(\left(-r_{\mathrm{PM}}^4 + r_{\mathrm{PM}}^2 r_{\mathrm{SLo}}^2\right)\nu_{\mathrm{PM}} + r_{\mathrm{PM}}^4 - r_{\mathrm{PM}}^2 r_{\mathrm{SLo}}^2\right)E_{\mathrm{SL}}} \tag{2}$$

The materials are defined at this stage. The selection of the materials is closely connected to the electrical machine design. The influence of the material selection on the design process is shown with the examples of the developed prototypes in Section III-A. The materials can be changed to meet the requirements, as shown in Fig. 1.

After the machine electromagnetic design has been verified by FEM, the machine parameters are grouped and are sent to the relevant steps for further design and analysis. The stator dimension and material selections are transferred to step 6 for the casing design. The information about the rotor materials and dimensions is sent to the next step, step 4, for simulation of the dynamic behavior of the full rotor.

A preliminary decision about the cooling method is made during the electromagnetic design. The calculated machine losses are then sent to step 7 for detailed cooling analysis.

Manufacturing and assembly limitations must be taken into account during the electromagnetic design to avoid extra iteration steps. These limitations are, for example, fixtures on the outer diameter of the stator.

Once the electromagnetic design of an HS machine is ready, it must be verified that the rotor diameter is below the given limit. If it is not possible to design the electrical machine within the limitation calculated in step 2, other rotor materials must be selected. In this case, steps 2 and 3 must be repeated.

D. Step 4. Initial Rotordynamics Analysis

The aim of the initial rotordynamics analysis is to determine the feasibility of the proposed structure. At this point, the maximum diameter and length of the rotor of the electrical machine are known. The length and diameter of the other parts of the rotor, such as end windings, seals, bearings, and attachments to the rotor, e.g., impellers, should be approximated. The added mass and inertia of the impellers or couplings as well as the connection method should be known to enable accurate prediction of the dynamic behavior. When the conceptual rotor is known, the model can then be built and analyzed. The operational speed of the electrical machine is known from the requirement list, so rotor performance in that speed region can be evaluated. As a rule of thumb, the critical speeds should be $\pm 15\%$ from the operational speed to guarantee good performance [18]. If the results are unsatisfactory, for example, the rotor is above the first critical frequency at the operational point, the length/diameter ratio can be modified, and steps 2 and 3 can be repeated. It is also possible to operate above the critical frequencies, but greater demands are then placed on the bearings in order to pass the critical frequency.

The developed prototypes utilize a TC winding configuration. Fig. 3 shows the effect of TC windings and DWs on the rotor structure. The top part of Fig. 3 shows the original structure used in the critical speed map analysis shown in Fig. 4. This rotor design is possible when TC windings are implemented, due to the shorter end winding protrusion length in two-pole machines.

The bottom part of Fig. 3 shows the 50% longer center part structure used in the critical speed map analysis shown in Fig. 4. This longer rotor structure is an excessive result of utilizing conventional DW. The end winding axial protrusion length is about 50% greater than that with TC windings as shown in [19]. Moreover, with DW, there is uncertainty in the final end winding protrusion length because of manufacturing aspects. The longer rotor represents the case where the end windings require more space than assumed in the initial analysis. Practically, the longer the rotor, the lower are the critical speeds. A rotor that requires high critical speeds has to be short. A short design also leads to a smaller and lighter machine, which is usually a desired feature.

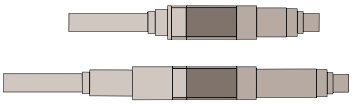

Fig. 3. Rotor structure for TC winding machine (top) and 50% longer middle part for a full pitch DW machine (bottom).

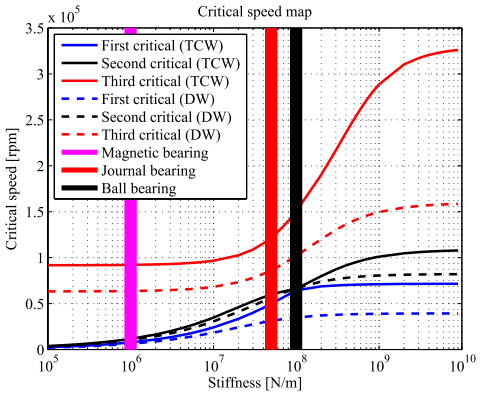

Fig. 4. Critical speeds with TC winding structure (solid lines) and with the 50% longer DW structure (dashed lines).

A critical speed map for the example structures in Fig. 3 is shown in Fig. 4. Use of a critical speed map is a clear way to see the relationship of the support stiffness to the critical speeds. The horizontal axis in the figure gives the support stiffness, and the vertical axis shows the critical speeds. The supports in the rotors are usually bearings, and selection of the bearing topology enables a specific stiffness to be achieved. The critical speed map is calculated without damping at zero rotation speed, and thus, it does not consider the gyroscopic effect. Knowledge of the approximated critical speed permits the general rotor-support behavior to be determined. The solid lines refer to the TC structure, and the dashed lines refer to the structure in which the largest diameter part of the shaft is 50% longer. The vertical lines represent typical bearing stiffnesses with different bearing topologies. Magnetic bearings have a stiffness value of $1 \cdot 10^6$ N/m, journal bearings $5 \cdot 10^7$ N/m, and ball bearings $1 \cdot 10^8$ N/m. The bearing stiffness margin in Fig. 4 is $\pm 10\%$, and the given values are in the radial direction.

Fig. 4 shows that increasing the length of the rotor leads to lower critical speeds. For example, with ball bearings, the achievable stiffnesses are in the range of $1 \cdot 10^8$ N/m. With TC windings, the first critical speed is 70 000 r/min, the second is 72 000 r/min, and the third is 145 000 r/min. If the active part length is increased by 50% because of the DWs, the first critical speed drops to 35 000 r/min, the second to 71 000 r/min, and the third to 100 000 r/min. In this case, the first and third critical speeds have the biggest change when the length is increased as the second critical speed is almost the same with both models. By extension of the active part length, the first critical speed is reduced to half that of the original structure. For undercritical operation with 20% safety margin, the machine with TC windings could be driven at the rated speed of 56 000 r/min, and the machine with DW at the rated speed of 28 000 r/min.

E. Step 5. Bearing Selection

The bearing selection step is related to the previous step in which the feasibility of the rotordynamics was determined. The most commonly used bearing types are explained here, and special parameters related to such bearings are determined.

The most commonly used bearing type is rolling element bearings such as ball and spherical roller bearings. This type of bearing is used in low- and medium-speed rotating machines. These bearings have the highest stiffness, as can be seen in Fig. 4 (black vertical line). As the rotation speed increases, the centrifugal forces push the rolling elements to the outer ring, and the stiffness at the center of the bearing consequently decreases [20]. With HS operations, this topology requires special design, and lightweight rolling elements should be used, e.g., ceramic silicon nitride balls. Ceramic balls offer the additional benefit of prevention of bearing currents. Rolling element bearings are a passive type of bearing, and variation in the bearing properties depends on the installation process.

Fluid film bearings are used when higher damping and higher rotation speed are required. Very high rotation speeds can be achieved with this type of bearing due to the discontinuity between the pads. Tilted bearing pads can be used to give better damping. The stiffness achieved with this type of bearing is lower than that with ball bearings, which affects the operational range, as can be seen in Fig. 4 [21].

Active magnetic bearings (AMBs) generally have lower stiffness values than ball or journal bearings. However, they enable active control of the stiffness and damping values. Because there is no mechanical contact between the rotor and the bearing, this type of bearing can be used in HS applications. The maximum speed is limited by the stress on the electrical lamination sheets that are required on the shaft at the radial bearing location or by the bandwidth of the control system. Very HS solutions with AMBs have been reported in [22] and [23].

Despite the many advantages of AMBs, such as low friction, cleanliness, possibility of actively controlling the rotordynamics, etc., these bearings bring also significant design challenges as they need extra length and add to the mass of the rotor causing, therefore, easily exacerbating problems with rotordynamics. AMBs may allow supercritical speeds, but naturally, the control challenges are then emphasized. AMBs, in principle, allow the highest speeds but require the longest rotor. Shorter rotors permit higher critical speeds and can be made with traditional ball bearings but do not allow HSs. Fluid film bearings are widely used. The space needed for these bearings is fairly low, but the bearings generate high losses, and naturally, the lubricating system needed increases the complexity of the fluid bearing systems.

F. Step 6. Casing Design

The casing provides support for the rotating part and protects the inner part of the machine from the environment. All of the requirements given in step 1, such as cooling concept, electrical connections, and measurement connections (temperature, pressure, etc.), should be met in the casing design step.

In step 4, the initial rotordynamics analysis is performed with an assumption of rigid support as it has not been defined at that point. When the casing is known, its stiffness can be calculated with structural FEM software. A study by Nicholas and Barrett [24] shows that the casing stiffness influences the rotor's dynamical performance by lowering the critical speeds. Thus, a rotordynamic model that includes bearing support stiffness will predict the actual critical speeds more accurately.

The clearance required for the seals between the different parts should be considered for the operating temperature range. However, as the cooling is not yet fixed, a couple of design loops exists between the casing design (step 6) and the cooling design (step 7).

The casing dimensions must be below the values specified in the requirements. If the outer dimensions exceed the limits, the power density of the machine must be increased in step 3. Any power density increase must be taken into account from the cooling system design point of view.

G. Step 7. Cooling Design

The results from the previous steps are utilized in the cooling design to ensure that the machine operating temperature remains low enough for safe operation. The main input parameters of the cooling design are the dimensions of the machine and the materials used, including information about the shrink fits, rotation speed, losses (electromagnetic and mechanical losses), and allowed temperature rise. The most common cooling method in HS electrical machinery is forced air cooling, where an additional blower or a shaft-mounted blower is utilized to create sufficient cooling air flow to remove heat from the interior parts of the machine. In addition to forced air cooling, liquid cooling solutions are also widely used in industrial applications. In its simplest form, liquid cooling involves the machining of cooling channels into the frame tube above the stator stack. The heat is transferred mostly by thermal conduction from the inner parts of the machine to the liquid-cooled frame tube in the radial direction through the stator iron. Combinations of forced air and liquid cooling methods also exist [25]. A comprehensive state-of-the-art survey of cooling solutions for HS electrical machines can be found, e.g., in [26].

In order to select the most cost-efficient cooling method, thermal analysis of the electrical machine is needed. The result of the thermal analysis is the temperature distribution of the machine structure at a given volumetric cooling fluid flow rate. The volumetric cooling fluid flow rate needed and the total pressure drop in the cooling channel constitute the basis of the blower or pump selection.

Thermal analysis can be done utilizing lumped parameters, FEM, or computation fluid dynamics. In most cases, lumped-parameter-based thermal analysis is accurate enough, and in terms of required computational time, it is the best option for practical design purposes [27], [28]. The results of the lumped-parameter-based analysis are the maximum and average values of the temperature in the stator windings, stator core, PM, and rotor sleeve, which will then be compared with the acceptable values. The pressure drop within the cooling fluid flow passages can be analytically calculated by utilizing the calculated cooling fluid flow rate and the dimensions of the cooling fluid flow passages.

If at this step the calculated temperatures are higher than the selected materials can tolerate, changes are required at the electromagnetic design stage (step 3). This problem can be approached in several ways: an alternative cooling method capable of dissipating more heat could be proposed, or the machine type or topology could be changed. A less radical solution might be via loss minimization, which can usually be achieved through the use of different materials, by implementing structural changes, or via geometry optimization.

H. Step 8. Detailed Rotordynamics Analysis

The conceptual rotordynamics was calculated in step 4, and the conceptual suitability was determined. In step 4, the support was assumed to be attached to rigid ground. At this point, more details can be implemented to the rotordynamic analysis, e.g., a more detailed casing stiffness (initially considered in step 6) can be included in the analysis.

Cooling design requirements and tolerances for the seals can be included in the rotordynamics analysis. In step 4, the seals were conceptual. Additional features that require modifications to the shaft should also be included in the detailed rotordynamics analysis, e.g., shoulders for the sensors, fixture holes, and shoulders for the seals (e.g., labyrinth seals). The dynamic behavior of the rotor can be studied as it grows or shrink during operation (sensitivity analysis). This is essential if the rotor is very long and also if seals are used.

I. Step 9. Manufacturing, Assembly, and Commissioning

At this point, many design constraints have already been set, and the structure can be considered as fulfilling the requirement list. The design details now need to be transferred to the manufacturing drawings. In this step, it would be beneficial to know what tools are available in the manufacturing workshop in order to avoid special machining (which is usually more costly). Some parts such as the casing should be separated into sections so that they can be manufactured and assembled easily [29].

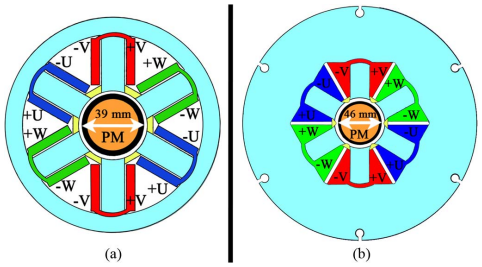

Fig. 5. (a) 3.5-kW HS PM synchronous motor geometry. (b) 11-kW HS PM synchronous generator geometry.

The aim is to use as many stock-sized parts as possible as they are reasonably priced and do not require long machining times.

At the manufacturing stage, the devices required are detailed, and arrangements and reservations are made for their use. Any special tools that might be required should be designed at this point. Examples of such tools are different kinds of jigs to temporarily hold parts in place until the final attachment is completed. The required sensors and controls can also be ordered (and designed) at the beginning of the prototype manufacturing process.

One of the first activities in the commissioning step is to check the requirement list in step 1 for special tests that might be needed. In every case, however, the cooling method, rotor, and electric machine should be tested to ensure that they fulfill the design requirements and have the required performance. The rotor can be tested before assembly with experimental modal analysis (EMA). EMA reveals the free–free natural frequencies, which can be compared to the rotordynamics model used in the analyses. The model can then be modified to agree more accurately with the actual rotor performance. It should be noted that, in HS rotors, there is always a variation in the natural frequencies of each rotor due to manufacturing imperfections and differences in fittings and tolerances of the complete rotor assembly.

III. Case Studies

All of the steps of the design flow (see Fig. 1) were applied to two HS PMSMs. The features of the designed electrical machines that affect the design flow are described in this section.

The designed prototypes under examination have similar electrical machine topologies. Fig. 5 illustrates the topology of the 3.5- and 11-kW PMSMs. In both cases, the rotor consists of a full cylindrical magnet, which is diametrically magnetized.

The PM is inserted inside the retaining sleeve using a shrink fit method in which the sleeve is heated and the cold magnet inserted inside. The magnet is made of one piece, and the retaining sleeve materials in both machines are nonmagnetic; therefore, no additional forces affect the PM during the installation into the sleeve.

Sintered PM materials are well suited for this kind of installation as they have high pressure tolerance. It must, however,

TABLE II
DESIGNED MACHINE MECHANICAL STRESSES

Machine parameter	3.5 kW PMSM	11 kW PMSM
Shrink fit λ, mm	0.014	0.017
Temperature T, °C	120	120
Maximum stresses at contact boundary		
Radial stress σ_r, MPa	-21	-4
Tangential σ_t, MPa	162	70
von Mises σ_{vmises}, MPa	174	72
Safety factor to yield strength	5.0 (880 MPa)	2.8 (205 MPa)

be borne in mind that the temperatures in the magnet material must remain low enough during the rotor assembly not to affect the material magnetization. Without special arrangements, the magnet is, in principle, in air during this work, and its flux density is therefore very low. This may be critical if the sleeve temperature is high and heat is transferred to the magnet material after sliding it into the sleeve. This installation phase must be studied by FEA and the stresses caused compared to the J, H-chart of the PM material. As a remedy, this phase can also be realized inside a ferromagnetic special steel tube tool to enable a higher flux density before cooling the rotor.

A. Materials

Although the two machines under consideration have similar topologies, the parts are made of different materials. The material selection of the retaining sleeve affects the overall HS machine design, especially with hollow shaft constructions. The sleeve has to tolerate stresses from the centrifugal forces, and the boundary surface contact between the PM and the sleeve must exist throughout the machine operation [30]. In addition, in configurations with hollow shaft, the torque is transferred through the retaining sleeve only.

In both machines in this study, the magnet retaining sleeves are made of an electrically conductive material, and rotor losses due to eddy-currents will therefore exist. With skillful design, these losses do not usually lead to a significant efficiency drop [31]. Nevertheless, if heat dissipation from the rotor is poor, the sleeve eddy-current losses could cause irreversible demagnetization of the PM because of direct heating of the magnet. Thus, material electromagnetic properties place some restrictions on selection of the material of the magnet retaining sleeve. Study of different sleeve materials for HS applications can be found, for instance, in [32].

A titanium retaining sleeve was selected for the 3.5-kW PMSM. Titanium, for example Ti-6AL-4 V, has exceptional mechanical properties, and its conductivity is equal to $5.8 \cdot 10^5$ S/m, which is 70% lower than stainless steel conductivity. Austenitic stainless steel AISI 316L was selected as the retaining sleeve material for the 11-kW generator. This material has higher conductivity and 77% less yield strength than Ti-6AL-4 V. However, the price of the material is lower, and it is widely available.

The mechanical stresses exerted in the rotor at the magnet–sleeve area are presented in Table II. The highest stresses occur between the boundary of the magnet and sleeve.

TABLE III
MAIN PARAMETERS OF THE DESIGNED MACHINES

Machine parameter	3.5 kW PMSM	11 kW PMSM
Rated speed n_n, min^{-1}	45000	31200
Number of poles p	2	2
Number of stator slots Q_s	6	6
Rated torque T_n, Nm	0.74	3.36
Rotor outer diameter D_o, m	0.039	0.046
Physical air-gap length δ, m	0.002	0.003
External diameter D_e, m	0.140	0.242
Active length l, m	0.022	0.060
Permanent magnet material	SmCo	SmCo
Permanent magnet remanence B_r, T	1.10	1.12
Stator stack lamination material	NO10	M-270-35A
Retaining sleeve material	Titanium	Stainless steel
Magnetic wedges material	Spindurol	Magnoval 2067
Bearing type	Magnetic bearing	Ball bearing

Maximum interference is utilized in the analysis. The sleeve is required to be under compression (negative value) to the magnet in order to transfer the produced torque. The stresses were studied at the rated speed.

The PM material is SmCo in both prototypes. The key reasons for selection of a SmCo PM were the eddy-current losses in the magnet retaining sleeve and the compact design of the whole system. The impeller works close to the PM, and its working temperature is above 260 °C. SmCo can tolerate higher temperatures than other PM materials, and as a consequence, the machine has a higher possible operating temperature without the risk of an irreversible demagnetization. The drawback of this material is the higher cost.

The key parameters of the designed machines are given in Table III. The stack lamination material is NO10 for the 3.5-kW machine. This material has low per unit losses, and its thickness is 0.1 mm. These factors reduce the iron losses, but the stack space factor is only 0.93. M-270-35 A steel was selected for the 11-kW PMSM stator stack. Compared to NO10, it has higher per unit losses at high frequencies, and the thickness is equal to 0.35 mm, which together increase the iron losses. The benefits of the material are its easy availability and low price with respect to the NO10. In both machines, the lamination sheets were laser cut.

Magnetic wedges were inserted between the tooth tips in both machines. Utilization of magnetic wedges decreases the slot harmonics in the air gap, which, in turn, reduces rotor eddy-current losses. Spindurol, which was used for the 3.5-kW machine, has a relative permeability of 2.4 at 0.7 T. The 11-kW generator has Magnoval 2067 wedges between the tooth tips. This material has a relative permeability of 2.9 at 0.7 T. Rotor loss reduction in the 11-kW PMSM due to the magnetic wedges is presented in [33].

B. Geometry

Geometry optimization is required to minimize losses. The designed machines have different loss minimization

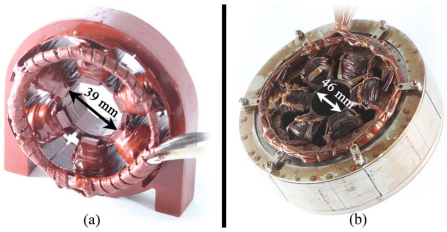

Fig. 6. (a) 3.5-kW HS PM synchronous motor stator. (b) 11-kW HS PM synchronous generator stator.

approaches, and therefore, $\chi = 0.55$ in the 3.5-kW machine, and $\chi = 1.3$ in the 11-kW machine. The length/diameter ratio dictates the proportion of active (in slots) and passive (end windings) copper in the stator.

The increased magnetic air gap limits the flux density variations due to both slot and current linkage harmonics [34], [35]. With the nonmagnetic sleeves used, the magnetic air gap lengths are 5 and 5.5 mm in the 3.5- and 11-kW machines, respectively.

The majority of the losses in the conductive sleeves occur on the outer diameter of the sleeve [31]; thus, to further reduce the rotor losses, the actual physical air gap length should be increased [36]. Following the temperature analysis in step 7, the stainless steel sleeve thickness in the 11-kW PMSM was consequently reduced. New rotor parameters were transferred to step 2 for the structural analysis. A new design iteration of the active part was done in step 3, and the new loss values were used in step 7 for the thermal analysis. Retaining sleeve thickness equal to 2.5 mm was found to be optimum from the mechanical and thermal points of view. This sleeve thickness is the minimum achievable without special machining.

Fig. 6(a) shows a photograph of the 3.5-kW PMSM stator prototype. The machine was made open slot to allow the TCs to be inserted as prefabricated on the teeth. However, analysis of a similar HS machine with six slots and two poles has shown that the eddy-current distribution gets smaller with increasing tooth tip width [37]. In the 11-kW machine, the teeth were made semiclosed. The winding work is more complicated, the copper space factor is lower with a semiclosed slot, and a segmented stator structure was therefore implemented.

The segmented stator structure makes it possible to capitalize on the TC windings. Because of the TC winding selection, both machines under consideration have electrically and magnetically isolated phase windings, and their fault tolerance is higher [38], [39]. For the 11-kW machine, the prefabricated segmented stator subassemblies enable low-cost high-volume manufacturing, despite the semiclosed slots.

Fig. 6(b) shows a photograph of the 11-kW HS PMSM stator prototype. Geometry optimization was done, taking into consideration the selection of lamination with higher per unit losses and greater thickness. The stator yoke was made exceptionally thick to reduce flux density and hence decrease iron losses. The optimization procedure is described in detail in [19].

IV. Loss Analysis

The losses are calculated in step 3 of the design flow. The loss distribution is of great importance in an HS PMSM. Due to the limited volume, the total losses and their particular components have to be calculated accurately to enable accurate cooling system design (step 7) and ensure reliable machine operation.

The mechanical losses can be estimated from bearing friction torque with an empirical approach proposed by Palmgren [40]. The total friction torque consists of the viscous friction torque and the load-dependent friction torque. Depending on the application, axial load and rubbing seals might also require examination. The total friction can be estimated by summing the different torque components as

$$T_{\text{friction}} = T_1 + T_2 \tag{4}$$

where T_1 is the viscous friction torque and T_2 is the load-dependent friction torque. Viscous friction torque can be calculated as

$$T_1 = 10^{-7} f_0 (\nu n)^{\frac{2}{3}} d_M^3 \tag{5}$$

where f_0 is an index for the bearing and lubrication type. For deep-groove ball bearings, the range is 0.7 (light series) to 2.0 (heavy series) when grease lubrication is used. Values can be found from literature, e.g., Brändlein *et al.* [41]. ν is the operating viscosity (cSt), n is the bearing speed (r/min), and d_M is the mean diameter of the bearing inner and outer diameters or the so-called pitch circle (mm). The load-dependent friction torque can be calculated as

$$T_2 = f_1 F_{\text{mean}} d_M^3 \tag{6}$$

where f_1 is a factor for the load. For a radial bearing with a cage, the values range from 0.0002 (light series) to 0.0004 (heavy series) [41]. F_{mean} is the mean load acting on the bearings.

The power can then be calculated by

$$P_{\rho,\text{bearing}} = T_{\text{friction}} \Omega. \tag{7}$$

AST 7005 AC bearings were used in the experimental setup of the 11-kW machine. The power losses associated with the resisting drag torque of the rotating cylinder are

$$P_{\rho,w1} = \frac{1}{32} k C_M \pi \rho \Omega^3 D_r^4 l_r \tag{8}$$

where k is a roughness coefficient (for a smooth surface $k = 1$, usually $k = 1 - 1.4$), C_M is the torque coefficient, ρ is the density of the coolant, D_r is the rotor diameter, and l_r is the rotor length. The torque coefficient C_M depends on the Couette Reynolds number Re_δ. Implementation of magnetic wedges makes the air gap homogeneous and reduces the roughness coefficient.

The end surface power losses are

$$P_{\rho,w2} = \frac{1}{64} C_M \rho \Omega^3 \left(D_r^5 - D_{\text{ri}}^5 \right) \tag{9}$$

TABLE IV
LOSS DISTRIBUTION OF THE 3.5- AND 11-kW MACHINES

Losses Type	3.5 kW PMSM	11 kW PMSM
Copper losses, W	104	88
Stator Iron losses, W	121	100
Rotor Sleeve losses, W	25	34
Rotor Magnet losses, W	4	11
Additional losses, W	17	22
Mechanical losses, W	125	456
Total losses, W	396	711

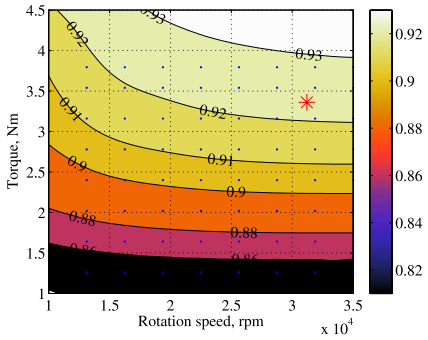

Fig. 7. Calculated efficiency map of the 11-kW HS PMSM. Rated point is marked with an asterisk.

where D_{ri} is the shaft outer diameter and the torque coefficient C_M depends now on the tip Reynolds number Re_r [13].

The total calculated mechanical losses P_{mech} consist of the windage and bearing losses and are the sum of (7)–(9).

The iron, copper, and rotor eddy-current losses were calculated using FEM in step 3. The calculated loss distributions of both machines under consideration at the rated operational point are shown in Table IV.

In the 11-kW PMSM, the mechanical losses are the major components of the total losses. Even with copper loss increase due to the lower winding factor or iron and rotor loss increase due to the higher harmonic content of TC windings, the mechanical losses are dominant. With the 3.5-kW PMSM, the copper, iron, and mechanical loss shares are balanced. The reduction of the mechanical losses was possible due to implementation of AMBs.

The result of the loss calculations for the 11-kW PMSM at different speeds and loads is shown in the efficiency map in Fig. 7.

V. MEASUREMENTS

Test planning and execution during the commissioning (step 9) vary depending on the customer's requirements, the machine's operating environment, and the manufacturer's facilities.

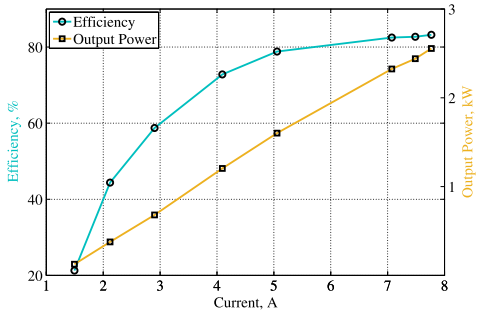

Fig. 8. Measured efficiency and output power of the 3.5-kW PMSM as a function of the phase current at 25 000 r/min.

Back EMF measurements of the 3.5-kW PMSM showed a very good agreement with FEM simulations. The difference between the simulated value of 209.9 V and the measured value of 211.7 V is below 1%.

The efficiency measurements of this machine were limited by the converter performance and coupling problems between the AMB-supported test machine and the eddy-current brake. For the aforementioned reasons, the maximum operational speed during the tests was only 25 000 r/min. The measurement results are shown in Fig. 8. The calculated rated point efficiency at 45 000 r/min was 88%, whereas the measured efficiency at 25 000 r/min was 83%.

A special measurement installation was manufactured to test the developed 11-kW PMSM separately from the final product system. The installation comprised the electrical machine in a protective case with a forced air cooling system, an eddy-current brake with water cooling, and a joint coupling between them. The designed 11-kW PMSM worked in the motor mode, and the input power from the frequency converter was measured with a Yokogawa PZ-4000 power analyzer. The output power was calculated by multiplication of the torque and speed measured by the eddy-current brake. More detailed information about the test setup can be found in [42]. No-load and load tests were conducted to verify the design methodology and loss calculations.

Fig. 9 shows the measured efficiency map of the 11-kW PMSM. A comparison with the calculated efficiency map, illustrated in Fig. 7, shows that, in the low-speed region, the actual losses are higher than the calculated ones. This may be partly explained by the extra losses in the joint coupling, which were not included in calculation of the losses. This hypothesis is supported by the significant difference in the calculated and measured losses at no load.

At HS, however, there is a good agreement between the calculated and measured results. For instance, at the rated point $n = 31\,200$ r/min and $T = 3.36$ Nm, the efficiency difference is below 1%. This result indicates that the loss calculations discussed in Section IV are fairly reliable. A good agreement of the measured and calculated results indicates the high accuracy of the proposed design methodology for the studied HS PMSMs.

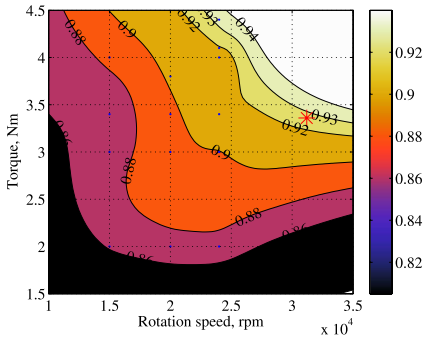

Fig. 9. Measured efficiency map of the 11-kW HS PMSM. Rated operating point is marked with an asterisk.

The overall efficiency of the designed machine at the rated point is about 92%. The electrical efficiency of the machine is above 97%, since the mechanical losses form about two thirds of the total machine losses. The selected machine topology is very well suitable for HS operation due to the rather high efficiency, robust mechanical design, and reduced manufacturing costs.

VI. Conclusion

This paper has presented a design methodology for HS PMSMs. By following the proposed design flow, the design process becomes systematic and straightforward. The outcome leads to shorter design time due to a reduction in the number of iterations and mistakes. Additionally, unnecessary parallel working is avoided. The proposed design methodology divides the tasks between different engineering disciplines clearly. Every step of the design flow is described. Critical design issues regarding electromagnetics, mechanical stresses, rotordynamics, thermal analysis, manufacturing, and assembly are highlighted.

The design methodology is applied to two HS PMSMs having the same electric machine topology. The designed machines have different loss minimization approaches. The influence of the utilization of TC windings in a two-pole machine on rotordynamics is demonstrated by showing the reduced winding space effect on the critical speeds.

The 11-kW machine measurement results are in good agreement with the results calculated using the presented design methodology, which verifies that the methodology is suitable for HS PMSM design and fairly accurate. The high measured electrical efficiency of the six-slot two-pole HS PMSM with TC windings confirms that this topology selection for an HS operation is well reasoned.

In future work, this design methodology can be refined so that it can be adapted to other HS electrical machine topologies while following the same process at the conceptual level.

References

[1] A. Tenconi, S. Vaschetto, and A. Vigliani, "Electrical machines for high-speed applications: Design considerations and tradeoffs," *IEEE Trans. Ind. Electron.*, vol. 61, no. 6, pp. 3022–3029, Jun. 2014.

[2] R. R. Moghaddam, "High speed operation of electrical machines, a review on technology, benefits and challenges," in *Proc. IEEE ECCE*, 2014, pp. 5539–5546.

[3] D. Gerada *et al.*, "High-speed electrical machines: Technologies, trends, and developments," *IEEE Trans. Ind. Electron.*, vol. 61, no. 6, pp. 2946–2959, Jun. 2014.

[4] J. Pyrhönen, J. Nerg, P. Kurronen, and U. Lauber, "High-speed high-output solid-rotor induction-motor technology for gas compression," *IEEE Trans. Ind. Electron.*, vol. 57, no. 1, pp. 272–280, Jan. 2010.

[5] S. Li, Y. Li, W. Choi, and B. Sarlioglu, "High speed electric machines—Challenges and design considerations," in *Proc. 21st ICEM*, Sep. 2014, pp. 2549–2555.

[6] A. Arkkio, T. Jokinen, and E. Lantto, "Induction and permanent-magnet synchronous machines for high-speed applications," in *Proc. IEEE ICEMS*, 2005, vol. 2, pp. 871–876.

[7] Z. Kolondzovski, A. Arkkio, J. Larjola, and P. Sallinen, "Power limits of high-speed permanent-magnet electrical machines for compressor applications," *IEEE Trans. Energy Convers.*, vol. 26, no. 1, pp. 73–82, Mar. 2011.

[8] C. J. G. Ranft, "Mechanical Design and Manufacturing of a High Speed Induction Machine Rotor," Ph.D. dissertation, School Elect., Electron. Comput. Eng., North-West Univ., Mahikeng, South Africa, 2010.

[9] F. Cheng, H. Xu, and S. Xue, "Study on the design method of high speed permanent magnet synchronous machine," in *Proc. IEEE ICEMS*, 2011, pp. 1–6.

[10] N. Bernard, F. Martin, and M. El-Hadi Zaim, "Design methodology of a permanent magnet synchronous machine for a screwdriver application," *IEEE Trans. Energy Convers.*, vol. 27, no. 3, pp.624–633, Sep. 2012.

[11] T. Noguchi, Y. Takata, Y. Yamashita, Y. Komatsu, and S. Ibaraki, "220,000-r/min 2-kW PM motor drive for turbocharger," *IEEJ Trans. Appl. Ind.*, vol. 125, no. 9, pp. 854–861, Sep. 2005.

[12] J. Dong *et al.*, "Electromagnetic and thermal analysis of open-circuit air cooled high-speed permanent magnet machines with Gramme ring windings," *IEEE Trans. Magn.*, vol. 50, no. 11, pp. 1–4, Nov. 2014.

[13] J. Pyrhönen, T. Jokinen, and V. Hrabovcova, *Design of Rotating Electrical Machines*. Chichester, U.K.: Wiley, 2008.

[14] A. Borisavljevic, *Limits, Modeling and Design of High-Speed Permanent Magnet Machines*. Berlin, Germany: Springer-Verlag, 2012.

[15] B. Riemer, M. Lessmann, and K. Hameyer, "Rotor design of a high-speed permanent magnet synchronous machine rating 100,000 rpm at 10 kw," in *Proc. IEEE ECCE*, Sep. 2010, pp. 3978–3985.

[16] J. Pyrhönen, V. Ruuskanen, J. Nerg, J. Puranen, and H. Jussila, "Permanent-magnet length effects in ac machines," *IEEE Trans. Magn.*, vol. 46, no. 10, pp. 3783–3789, Oct. 2010.

[17] Y. Duan and D. Ionel, "A review of recent developments in electrical machine design optimization methods with a permanent-magnet synchronous motor benchmark study," *IEEE Trans. Ind. Appl.*, vol. 49, no. 3, pp. 1268–1275, May/Jun. 2013.

[18] S. Y. Yoon, Z. Lin, and P. E. Allaire, *Control of Surge in Centrifugal Compressors by Active Magnetic Bearings: Theory and Implementation*, 1st ed. London, U.K.: Springer-Verlag, 2013.

[19] N. Uzhegov, J. Pyrhönen, and S. Shirinskii, "Loss minimization in high-speed permanent magnet synchronous machines with tooth-coil windings," in *Proc. IEEE IECON*, Nov. 2013, pp. 2960–2965.

[20] E. Kurvinen, J. Sopanen, and A. Mikkola, "Ball bearing model performance on various sized rotors with and without centrifugal and gyroscopic forces," *Mech. Mach. Theory*, vol. 90, pp. 240–260, Aug. 2015.

[21] E. Logan Jr., *Handbook of Turbomachinery*, 2nd ed. New York, NY, USA: Marcel Dekker, 2003.

[22] S. Silber *et al.*, "High-speed drive for textile rotor spinning applications," *IEEE Trans. Ind. Electron.*, vol. 61, no. 6, pp. 2990–2997, Jun. 2014.

[23] T. Baumgartner, R. Burkart, and J. Kolar, "Analysis and design of a 300-W 500 000-r/min slotless self-bearing permanent-magnet motor," *IEEE Trans. Ind. Electron.*, vol. 61, no. 8, pp. 4326–4336, Aug. 2014.

[24] J. Nicholas and L. Barrett, "The effect of bearing support flexibility on critical speed prediction," *Tribol. Trans.*, vol. 29, no. 3, pp. 329–338, 1986.

[25] W. Jiang and T. Jahns, "Coupled electromagnetic-thermal analysis of electric machines including transient operation based on finite-element techniques," *IEEE Trans. Ind. Appl.*, vol. 51, no. 2, pp. 1880–1889, Mar./Apr. 2015.

[26] A. Boglietti *et al.*, "Evolution and modern approaches for thermal analysis of electrical machines," *IEEE Trans. Ind. Electron.*, vol. 56, no. 3, pp. 871–882, Mar. 2009.
[27] J. Nerg, M. Rilla, and J. Pyrhönen, "Thermal analysis of radial-flux electrical machines with a high power density," *IEEE Trans. Ind. Electron.*, vol. 55, no. 10, pp. 3543–3554, Oct. 2008.
[28] J. Nerg and V. Ruuskanen, "Lumped-parameter-based thermal analysis of a doubly radial forced-air-cooled direct-driven permanent magnet wind generator," *Math. Comput. Simul.*, vol. 90, pp. 218–229, Apr. 2013.
[29] G. Boothroyd, W. Knight, and P. Dewhurst, *Product Design for Manufacture & Assembly Revised & Expanded*. New York, NY, USA: Taylor & Francis e-Library, 2009.
[30] A. Borisavljevic, H. Polinder, and J. Ferreira, "On the speed limits of permanent-magnet machines," *IEEE Trans. Ind. Electron.*, vol. 57, no. 1, pp. 220–227, Jan. 2010.
[31] W. Li, H. Qiu, X. Zhang, J. Cao, and R. Yi, "Analyses on electromagnetic and temperature fields of superhigh-speed permanent-magnet generator with different sleeve materials," *IEEE Trans. Ind. Electron.*, vol. 61, no. 6, pp. 3056–3063, Jun. 2014.
[32] W. Li *et al.*, "Influence of rotor-sleeve electromagnetic characteristics on high-speed permanent-magnet generator," *IEEE Trans. Ind. Electron.*, vol. 61, no. 6, pp. 3030–3037, Jun. 2014.
[33] N. Uzhegov, E. Kurvinen, and J. Pyrhonen, "Design limitations of 6-slot 2-pole high-speed permanent magnet synchronous machines with tooth-coil windings," in *Proc. IEEE ECCE*, 2014, pp. 1–7.
[34] N. Bianchi, S. Bolognani, and F. Luise, "High speed drive using a slotless PM motor," *IEEE Trans. Power Electron.*, vol. 21, no. 4, pp. 1083–1090, Jul. 2006.
[35] P.-D. Pfister and Y. Perriard, "Very-high-speed slotless permanent-magnet motors: Analytical modeling, optimization, design, and torque measurement methods," *IEEE Trans. Ind. Electron.*, vol. 57, no. 1, pp. 296–303, Jan. 2010.
[36] N. Bianchi, D. Durello, and A. Fasolo, "Relationship between rotor losses and size of permanent magnet machines," in *Proc. IEEE SDEMPED*, Sep. 2011, pp. 251–257.
[37] K. Shigematsu, J. Oyama, T. Higuchi, T. Abe, and Y. Ueno, "The study of eddy current in rotor and circuit coupling analysis for small size and ultra-high speed motor," in *Proc. IEEE IPEMC*, 2004, vol. 1, pp. 275–279.
[38] F. Magnussen and H. Lendenmann, "Parasitic effects in PM machines with concentrated windings," *IEEE Trans. Ind. Appl.*, vol. 43, no. 5, pp. 1223–1232, Sep./Oct. 2007.
[39] J. Ede, K. Atallah, G. Jewell, J. Wang, and D. Howe, "Effect of axial segmentation of permanent magnets on rotor loss in modular permanent-magnet brushless machines," *IEEE Trans. Ind. Appl.*, vol. 43, no. 5, pp. 1207–1213, Sep./Oct. 2007.
[40] A. Palmgren, *Ball and Roller Bearing Engineering*. Philadelphia, PA, USA: SKF Industries Inc., 1959.
[41] J. Brändlein, P. Eschmann, L. Hasbargen, and K. Weigand, *Ball and Roller Bearings: Theory, Design, and Application*. Chichester, U.K.: Wiley, 1999.
[42] N. Uzhegov, J. Nerg, and J. Pyrhonen, "Design of 6-slot 2-pole high-speed permanent magnet synchronous machines with tooth-coil windings," in *Proc. 21st ICEM*, Sep. 2014, pp. 2537–2542.

Nikita Uzhegov (M'15) received the B.Sc. degree from Moscow Power Engineering Institute, Moscow, Russia, in 2010 and the M.Sc. degree in electrical engineering from Lappeenranta University of Technology, Lappeenranta, Finland, in 2012, where he is currently working toward the Ph.D. degree in the Department of Electrical Engineering.

His research mainly concerns electrical machines and drives, particularly high-speed machines.

Emil Kurvinen was born in Ristiina, Finland, on September 15, 1988. He received the B.Sc. and M.Sc. (Tech.) degrees from the Department of Mechanical Engineering, Lappeenranta University of Technology, Lappeenranta, Finland, in 2011 and 2012, respectively, where he is currently working toward the Ph.D. degree.

His current research interests include rotordynamics and magnetic bearings in high-speed electric machines.

Janne Nerg (SM'12) received the M.Sc. degree in electrical engineering, the Licentiate of Science (Technology) degree, and the D.Sc. (Technology) degree from Lappeenranta University of Technology (LUT), Lappeenranta, Finland, in 1996, 1998, and 2000, respectively.

He is currently an Associate Professor with the Department of Electrical Engineering, LUT. His research interests are in the field of electrical machines and drives, in particular, electromagnetic and thermal modeling and design of electromagnetic devices.

Juha Pyrhönen (M'06) was born in Kuusankoski, Finland, in 1957. He received the D.Sc. degree from Lappeenranta University of Technology (LUT), Lappeenranta, Finland, in 1991.

He became an Associate Professor of electrical engineering at LUT in 1993 and a Professor of electrical machines and drives in 1997. He is engaged in research and development of electric motors and power-electronic-controlled drives. He has wide experience in the research and development of special electric drives for distributed power production, traction drives, and high-speed applications. Permanent-magnet materials and applying them in machines have an important role in his research. He is also currently researching new carbon-based materials for electrical machines.

Jussi T. Sopanen (M'14) was born in Enonkoski, Finland, in 1974. He received the M.Sc. degree in mechanical engineering and the D.Sc. (Technology) degree from Lappeenranta University of Technology (LUT), Lappeenranta, Finland, in 1999 and 2004, respectively.

He was a Researcher with the Department of Mechanical Engineering, LUT, in 1999–2006. He was also a Product Development Engineer with the electric machine manufacturer Rotatek Finland Ltd., in 2004–2005. During 2006–2012, he was a Principal Lecturer of mechanical engineering and the Research Manager of the Faculty of Technology, Saimaa University of Applied Sciences, Lappeenranta. He is currently a Professor of machined dynamics with LUT. His research interests are rotor dynamics, multibody dynamics, and mechanical design of electrical machines.

Sergey Shirinskii (M'12) received the Ph.D. degree from Moscow Power Engineering Institute (MPEI), Moscow, Russia, in 1993. His Ph.D. thesis concerned simulation of the motor generator of an autonomous flywheel power storage.

After his Ph.D. studies, he worked at MPEI, where he is currently an Associate Professor with the Department of Electromechanics. His research fields are numerical analysis of magnetic fields and development of tooth contour method for simulation of electric machines.

Publication VI

Uzhegov, N., Pihlajamäki, A., Nerg, J., and Pyrhönen, J.
Magnetic Wedges in a Steam-resistant Electrical Machine Insulation System

Reprinted with permission from
IEEE Transactions on Dielectrics and Electrical Insulation,
vol. 22, issue 6, pp. 3153–3162, Dec. 2015

Magnetic Wedges in a Steam-resistant Electrical Machine Insulation System

Nikita Uzhegov, Arto Pihlajamäki, Janne Nerg and **Juha Pyrhönen**
Lappeenranta University of Technology
Skinnarilankatu 34
53850, Lappeenranta, Finland

ABSTRACT

The overall system efficiency of small turbogenerators and compressors can be significantly increased by using high-speed electrical machines. These machines enable a high level of system integration and compactness. In the studied turbogenerator application the turbine leakage steam is in direct contact with the electrical machine and therefore all the components of the machine insulation system, including magnetic wedges, must tolerate the process environment. The magnetic wedges improve the electrical machine performance. The effects of the superheated steam on several wedge materials with different coatings were studied by experimental accelerated aging tests. A test installation was developed to test the simultaneous influence of the temperature and moisture on the wedge aging. According to the data obtained from the visual inspection, microscope, Fourier Transform Infrared spectrum analysis, and dimension measurement analyses, different wedges absorb various amounts of water in a steam atmosphere. The effects of the coating layer damage during the wedge installation into the electrical machine, are observed.

Index Terms - **Wedges, aging, AC generators, rotating machine insulation testing, life estimation, thermal factors, environmental factors, infrared spectroscopy.**

1 INTRODUCTION

THE industry's constant need to increase the efficiency of the power supply is pushing the technology boundaries. The modern trends in the field of electrical machines aim at reducing the amount of wasted energy. One of the ways to achieve this goal is the high-speed (HS) electrical machines. They are already proven technology used in a number of industrial applications. The key benefits of these machines are their high power density, small footprint, high system overall efficiency and, especially high material efficiency. These advantages are attracting the manufacturers producing, for instance, gas compression applications, turbines, air blowers, vacuum pumps, and machine tool spindle drives [1, 2].

HS electrical machine allows connection of the working tool directly to the machine's rotor shaft without a mechanical gearbox. The small overall size of the system and high power density are achieved by installing the electrical machine into the same casing for example with a compressor or a turbine.

The aim of a project is to design and manufacture an integrated hermetic turbogenerator capable of producing 500 kW – 1 MW of electricity. The electrical generator to be implemented in this system is an HS induction machine (IM) positioned on the same shaft with the turbine. Due to the hermetic structure, the cooling system must be very efficient to remove the heat from the electrical machine. The cooling solution includes directly water cooled stator windings and direct water cooling in the rotor, which remove most of the heat load from the interior parts of the generator.

Steam leakage from the turbine influences the material selection of the electrical machine. The leakage of the turbine is slightly superheated steam with a high temperature and about 1 bar pressure. This steam is passing through the air gap of the machine and, therefore, all the materials implemented in the machine must tolerate it. Therefore, the rotor core is made of X20Cr13 ferromagnetic stainless steel to avoid corrosion.

The influence of the environmental and temperature factors on the electrical machine's insulation system is very well studied. The impacts of humidity on the stator insulation of large rotating electrical machines are discussed e.g. in [3]. Cable degradation during the high temperature accelerated aging is studied in [4]. The effects of voltage and temperature variations together with moisture on the epoxy resin are described in [5], [6].

Tanaka et al. [7] have presented the effect of water absorption on the aging of polymers and composites. Water

Manuscript received on 15 June 2015, in final form 13 August 2015, accepted 5 September 2015.

DOI 10.1109/TDEI.2015.005457

absorption decreases the mechanical strength and toughness of epoxy [8] and its glass transition temperature [9], and increases the permittivity and loss tangent of the insulation [10], [11]. A steam-resistant insulating system for a sealed turbogenerator was proposed and tested in [12].

Because the water cooled stator windings are used in the high-speed induction machine (HSIM) open stator slots are needed to enable the winding installation. The slot wedges are placed between the teeth. The magnetic wedges are part of the rotating electrical machine insulation system and are acting as the stator slot keys, providing mechanical support for the stator windings. The magnetic wedges in HS electrical machines also allow to decrease torque ripple, reduce the rotor surface losses, and increase the machine efficiency [13]. This also leads to a lower machine temperature [14]. The performance of the designed electrical machine with and without magnetic wedges is simulated and compared. However, the ability of the magnetic wedges to tolerate steam has not been investigated earlier.

In the designed generator, the steam passing through the air gap is in a direct contact with the magnetic wedges. The wedge manufacturers provide their products with different properties, for instance, with different thermal classes and relative permeabilities, but they have not been capable of verifying the steam resistance of their products.

The aim of this study is to find suitable wedge materials and their coatings, which are qualified to be a reliable part of the steam-resistant insulating system of a hermetic turbogenerator operating in a steam atmosphere. Several magnetic wedge materials are studied. This paper describes the analyses of the samples before and after the tests. Lifetime estimation tests of the samples are presented. The accelerated aging test equipment that was built to produce the required temperature and humidity is illustrated. Finally, conclusions are drawn on the suitability of each tested magnetic wedge material for the steam-resistant insulation system.

2 EXPERIMENTAL METHODS

2.1 ELECTRICAL MACHINE PERFORMANCE

The utilization of the magnetic slot wedges is extremely important, especially, in open slot solid-rotor electrical machines. To compare the performance of the designed HSIM with magnetic and with non-magnetic slot wedges, a Finite Element Method (FEM) analysis was performed.

Figure 1 shows the flux lines and the flux density distribution of the machine at the rated operation point. The top part of the figure illustrates a situation where the stator slot wedge is made of a magnetic material with a relative permeability equal to 3. The bottom part of the figure shows the same time instant, but with a non-magnetic wedge.

As we can see in Figure 1, flux density distributions are similar in both cases except the field in the wedges. The flux density is higher in the magnetic wedge and the flux lines are passing through the wedge to the stator teeth. This is explained by the lower fluctuations of the air gap normal flux density. Figure 2 shows a comparison of the air gap flux density normal component and its harmonic spectrum in the case of magnetic and non-magnetic wedges. The use of magnetic wedges reduces the amplitudes of the highest harmonics, for example, the 17th, 19th, 35th, and 37th. The sum of harmonic amplitudes is 18% less with the magnetic wedges compared to the case with non-magnetic wedges.

Figure 3 shows the loss distribution of the machines under study. The largest amount of losses occur at the very surface of the rotor. The loss share of the rotor tooth tips has reduced from 61% to 37%. As a result, the total losses of the machine with magnetic wedges are 41% lower compared to the same machine but with non-magnetic wedges. Such a considerable loss difference justifies the need for magnetic wedges in the solid-rotor HSIM under consideration.

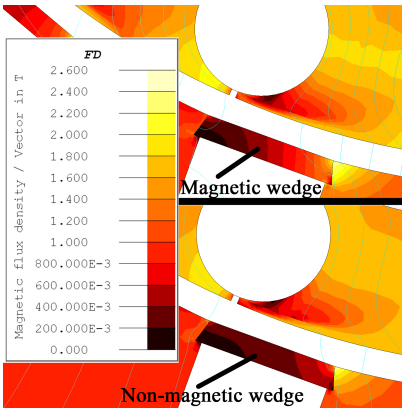

Figure 1. Flux density distribution and flux lines in the HSIM at the rated operation point with magnetic (top) and non-magnetic wedges (bottom).

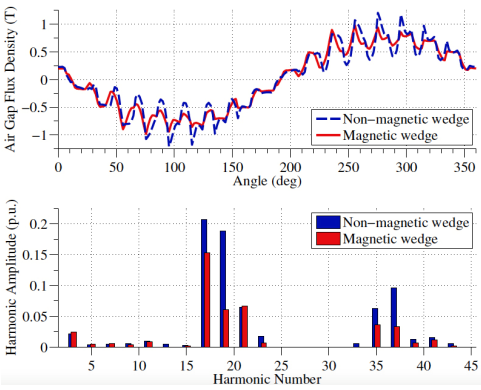

Figure 2. Normal component of the flux density in the middle of air gap with magnetic and non-magnetic wedges (top) and its harmonic component (bottom).

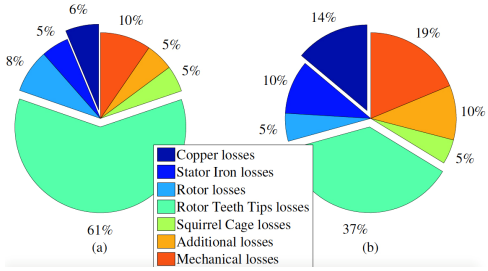

Figure 3. Loss distribution in the electrical machine with non-magnetic wedges (a) and with magnetic wedges (b).

2.2 TEST SAMPLES

Two companies provided the wedge samples and totally six different sample types were tested. Each type of sample material was provided in rectangular and designed slot wedge shapes. Figure 4 shows the samples of the two different shapes. The slot wedge shape resembles the actual magnetic wedge installed into the designed electrical machine. The only distinction is the length of the sample. The rectangular shape was selected to have more reliable measurements of the mass and linear dimensions.

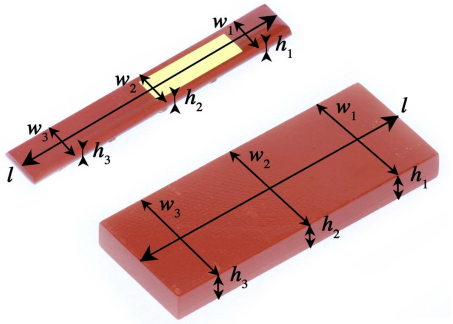

Figure 4. Covered wedge samples of the slot wedge shape (left) and the rectangular shape (right). The measurement points are shown.

Table 1. Sample description and labeling.

Sample label	Description
A 1	Rectangular, base material
B 1	Rectangular, brushed painting with alkyd lack
C 1	Rectangular, brushed painting with alkyd lack and dipped in epoxy resin 60841
D 1	Rectangular, brushed painting with alkyd lack and dipped in epoxy resin 2000/380
A 2	Slot wedge, base material
B 2	Slot wedge, brushed painting with alkyd lack
C 2	Slot wedge, brushed painting with alkyd lack and dipped in epoxy resin 60841
D 2	Slot wedge, brushed painting with alkyd lack and dipped in epoxy resin 2000/380
E 1	Rectangular, base material thermal class 155
E 2	Slot wedge, base material thermal class 155
F 1	Rectangular, base material thermal class 180
F 2	Slot wedge, base material thermal class 180

The wedges' base material composition is about 10% of glass fibre cloth, about 20% of epoxy resin and about 70% of iron powder. Because of the iron powder component, the relative permeability of the magnetic wedges ranges usually from 2 to 10 depending on the manufacturer and the applied magnetic field during the machine operation. Three types of samples have no cover and have a different base material.

To protect the base material, different types of coatings were implemented. Three types of samples were brushed with alkyd lack. Among them, two types of samples were additionally dipped in different epoxy resins. The composition of the epoxy resin 60841 is styrene 1–5%, xylene 1–5%, bisphenol-F epoxy 5–10%, 2-ethylexyl glycidyl ether 10–30%, and epoxy resin 60–100%. The second coating 2000/380 is an alkyd phenolic impregnating varnish temperature class 180. Table 1 describes the types of wedge materials used in the experiments. The letter in the sample label denotes the wedge material type and the number the shape of the sample.

Samples from A to D have the same base material. The manufacturing process of base material E uses a random glass mat reinforcement and a low pressure compression molding press to produce an isotropic material. To achieve a high thermal class, base material F is made laminated.

2.3 TEST SETUP

The test setup is a sealed column capable of tolerating high pressure and temperature. Figure 5 shows the model of the installation. The column consists of the top and bottom parts.

The top part comprises the major volume of the column, a pressure-relief valve, and input and output valves. An input valve is used to fill the column with water, and an output valve serves to empty the column after the test.

The bottom part is removable. Inside the bottom part there is an armature, which holds pressure and temperature sensors, a heater, and a matrix for the samples. The matrix has six slots for six different samples, which could be tested simultaneously in the same conditions. The matrix has small holes to let the water penetrate inside the matrix and to have a direct contact with the samples.

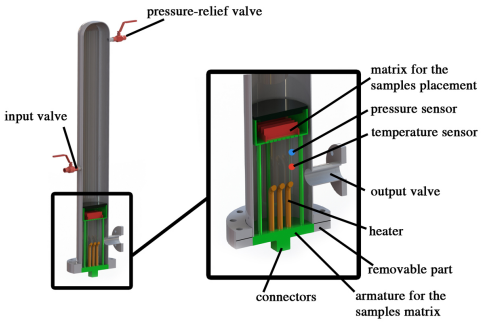

Figure 5. Model of the test setup.

Figure 6. Photo of the test column (left) and assembling of the bottom part (right).

When the samples are placed inside the matrix, the bottom part is installed and fixed with bolts. The heater is controlled by an electric current, and it is adjusted according to the reference temperature.

The total height of the column is 1.6 m, and the height of the input valve is 0.7 m. The inner diameter of the column is 219 mm. The water is pumped into the column through the input valve. The measured maximum amount of water is 24.6 litres.

Figure 6 shows the photo of the test setup. The column is thermally insulated to reduce the influence of the ambient temperature variations.

2.4 TEST CONDITIONS AND PROCEDURES

The accelerated aging tests were performed to detect possible irreversible property changes of the wedge materials. The experiment stresses are thermal and environmental (chemical) ones [15]. Multifactor aging is applied.

The final design of the turbogenerator unit is under development, and therefore, there is no exact information about the conditions of the steam passing through the air gap. The range of the steam temperature will be from 70 °C to 120 °C. It has been decided to test the wedge materials making an assumption that they have to satisfy Class 130 requirements.

To ensure the reliable operation at 120 °C insulation material accelerated aging tests are performed at temperatures from 150 °C to 200 °C. The required amount of testing time for each temperature follows the “ten degrees rule”, which states that the life of the insulation is reduced by 50 % for each ten degrees Centigrade temperature rise.

The first experimental setup was designed to tolerate the overheated steam up to 150 °C, and the first test was conducted at this temperature. The test time was 300 h. However, the minimum temperature safety margin between the operating conditions and testing temperature should be at least 40 °C. Therefore, the experimental setup was updated to tolerate steam up to 160 °C because the rated operating temperature could be up to 120 °C. The second test was conducted at the temperature of 160 °C.

As the maximum possible temperature of the experiment is 160 °C it has been decided to increase the testing time up to 500 h to ensure the reliability of the results.

During the experiment, six samples were placed in the slots of the matrix. Then, the bottom part of the column was fixed with bolts. After that, the column was filled with water through the input valve to fully cover the samples. Next, the heater was turned on, and the timing started at the moment when the temperature reached the desired level.

During the first run, adjustments were made to the control system to stabilize the temperature. After the required amount of time had passed, the heater was turned off and the temperature was allowed to decrease for several hours. When the temperature reached 50 °C, the column was emptied. To verify that the samples were fully covered with water during the whole experiment, the rest of the liquid was measured after the test.

A number of analyses were performed before and after the experiment. First, a visual analysis of every sample was made using a photo camera and microscope. Second, the physical dimensions: the length, height, width, and mass were measured. The points where the linear dimensions were made are shown in Figure 4. Based on these measurements, the volume and density of the samples were calculated.

In the electrical machine assembly process, the magnetic wedges are slid between the stator tooth tips. The stator is made of laminated steel, and there are always small burrs that could damage the coating of the wedges. Therefore, the last experiment was aimed to simulate a wedge coating damage. Two samples of every coated material were selected. In each pair, one of the samples was artificially damaged to simulate the effect of the sample installation process. All the selected samples were tested in the same conditions to observe the influence of a coating damage. Figure 7 shows the coated sample and the artificially damaged sample with the same coating.

Figure 7. Coated sample D 2 (left) and artificially damaged sample D 2 (right).

3 RESULTS AND DISCUSSION

3.1 VISUAL ANALYSIS

The appearances of every sample before and after the tests were compared. Figures 8–13 show the photos of the tested types of samples with a rectangular shape.

Finally, Fourier Transform Infrared (FTIR) spectrum analysis was performed for every sample before and after the experiments. Due to the limited amount of samples all the selected analyses were non-destructive.

The coated samples B and C (Figures 9, 10) have retained their coating, but the colour of the samples has changed. The coated sample D (Figure 11) has lost the outer epoxy coating. The epoxy layer has become brittle and has changed its colour. However, as in the case of sample B, the inner alkyd lack layer has remained on the sample surface.

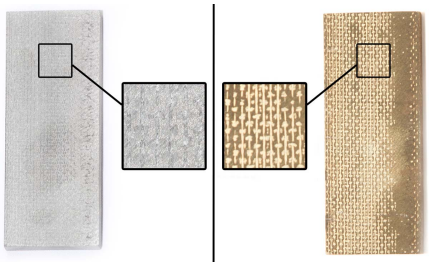

Figure 8. Sample A 1 before (left) and after the aging test (right).

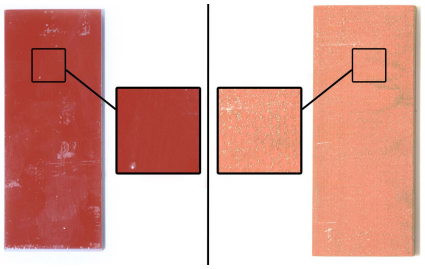

Figure 9. Sample B 1 before (left) and after the aging test (right).

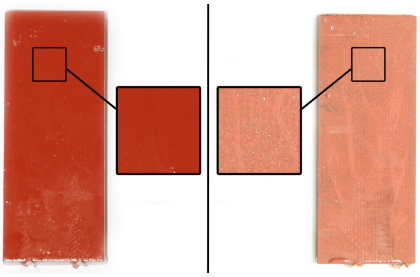

Figure 10. Sample C 1 before (left) and after the aging test (right).

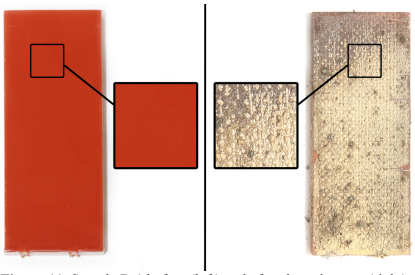

Figure 11. Sample D 1 before (left) and after the aging test (right).

Figure 12. Sample E 1 before (left) and after the aging test (right).

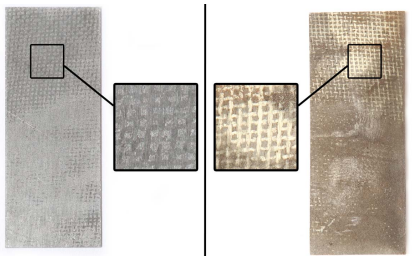

Figure 13. Sample F 1 before (left) and after the aging test (right).

On the surface of the uncoated samples, the influence of the steam after the test is well observable. In sample A (Figure 8), the glass fibre cloth structure is seen, but without any significant changes. The application of the different manufacturing process for sample E is seen in Figure 12. There is no clear sign of the glass cloth structure. Small spots appeared on sample E after the test.

Figure 13 illustrates the photos of sample F. The behaviour of the outer lamination layer is similar to sample A. Nevertheless, sample F had been delaminated already after the 150 °C test. Figure 14 shows the delamination of sample F in the rectangular and wedge shapes.

The visual analysis of the same wedge materials but with the slot wedge shape corresponds well with the rectangular wedge shape results. All slot wedge shape samples have aging signs on the surface, e.g., colour change, thinner lack layer, epoxy degradation, and small spots. Also, all samples, excluding sample F, retained their integrity.

Figure 14. Delamination of the sample F in the slot wedge shape (top) and in the rectangular shape (bottom).

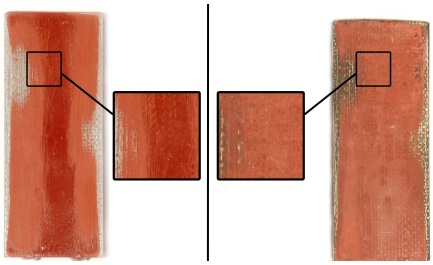

Figure 15. Artificially damaged sample C 1 before (left) and after the aging test (right).

The results of the test with the artificially damaged coatings correspond well with the above findings. Figure 15 shows the artificially damaged sample C before and after the test. In the middle of the sample before the test, the epoxy layer has been left. This layer dissolved after the 500 h test as it seen in the right-hand photo in Figure 15. The alkyd lack layer has changed its colour and become thinner. The base material of the sample shows the same colour change as sample A, whereas, no observable damage of the base material is detected.

3.2 CHANGE OF THE SAMPLE DIMENSIONS

All the samples were measured before and after the tests to observe the relative mass and volume increase. These results allow us to define the amount of absorbed water. The exact amount of absorbed water is difficult to define since some part of the coatings may be removed, and absorbed water replaces this mass.

The behavior of the rectangular wedges was similar to the behavior of the slot shape wedges. The slot shape wedge mass and the linear dimensions are comparable within the instrumental errors. To increase the accuracy of the results, only the parameters obtained from the rectangular slot wedge measurements are used in the calculations.

Figure 16 shows the relative increase in the mass and volume of the samples after the 150 °C test. Sample F is excluded from the results as it was clearly delaminated. The uncoated samples A and E absorbed water, and their mass and volume increased by more than 2 %. Because of the coating in samples B and C, their relative mass and volume change remained below 1 %, which may indicate a smaller amount of absorbed water.

The mass of sample D increased by about 2 % whereas its volume remained unchanged. This could be explained by the fact that the outer epoxy layer of sample D absorbed water and increased the mass of the sample. The epoxy layer became brittle and it was destroyed during the linear dimension measurements. Thus, no volume increase was observed.

Figure 17 shows the relative mass and volume increase of the coated and artificially damaged samples after the 500 h, 160 °C test. For every material, the differences between the coated and artificially damaged samples were insignificant.

By analyzing Figures 16 and 17 it is possible to compare the 300 h, 150 °C test to the 500 h, 160 °C test. It could be stated that after the 500 hours test, the relative mass increase of samples B and C has grown from 0.5 % to 1.5 %. In the case of sample D, this parameter has risen from 2 % to 2.5 %. The relative volume increase for all 500 h test samples is significant and varies around 3.5 %.

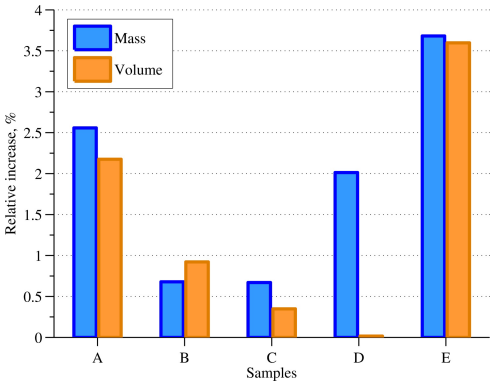

Figure 16. Relative mass and volume increase of the rectangular shape wedges.

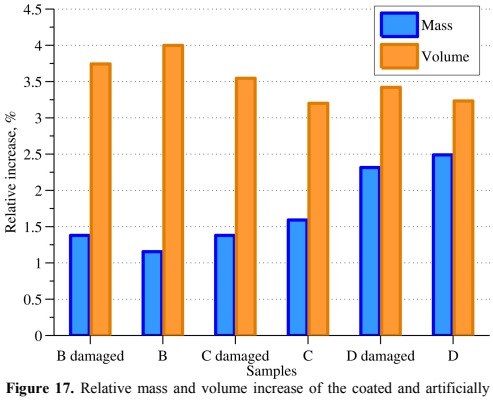

Figure 17. Relative mass and volume increase of the coated and artificially damaged samples.

The change in the sample volumes and masses indicates water absorption during the tests. To verify this assumption an FTIR analysis was performed.

3.3 FTIR ANALYSIS AND MICROSCOPE PHOTOS

FTIR spectra were recorded with a Perkin-Elmer Frontier instrument using a Spotlight 200 microscope equipped with an ATR (attenuated total reflectance) system. All spectra were averaged of 25 co-added scans with a resolution of 4 cm^{-1}. The recorded spectra were optimized with instrument software, and peaks caused by atmospheric carbon dioxide were removed. All these processes were performed simultaneously for the spectra presented in a same figure to ensure the maximum comparability. Figures 18–23 show the FTIR spectra of all tested materials before and after the tests.

Figure 18 shows the ATR-FTIR spectra of sample A. Comparing the spectra before and after the test new peaks at 987 cm^{-1} and a broad peak in the range from 3100 to 3600 cm^{-1} can be found. The existence of the broad peak at 3100-3600 cm^{-1} is due to water absorption as epoxy resin is known to absorb water from the surroundings. The base material of the samples was constructed of glass fibres with epoxy polymer. The peak at 987 cm^{-1} is due to the Si-O bond when epoxy polymer has been degraded and removed during the testing revealing the glass fibre surface.

The ATR-FTIR spectra of sample B is shown in Figure 19. New peaks can be detected at 990 cm^{-1} and at 3100-3600 cm^{-1} after the test. As with sample A, the broad peak at 3100-3600 cm^{-1} is probably due to water absorption of the epoxy polymer, and the peak at 990 cm^{-1} is due to the exposure of glass fibre. Vanishing peaks at 1718, 1256, 1114 and 1068 cm^{-1} are all associated with the alkyd lack and indicate removal of this material during the test.

The penetration depth of the IR radiation during the FTIR analysis of the epoxy samples is generally between 0.5 and 3 μm [16]. Most likely, the outer protecting layer of sample C epoxy polymer is thicker than 3 μm, and therefore, the FTIR analysis can detect only this part of the untreated sample. In Figure 20 a broad peak centred at 3460 cm^{-1} can be assigned to amine groups or phenolic groups of bisphenol-F. This peak is shifted to a somewhat lower wavenumber after the test. The broad peak centred at 3255 cm^{-1} in the spectra of after samples would hint slight water absorption into the base material as the protecting layers have mostly disappeared. This can be stated since the peaks caused by the protecting layers at 1730, 1606, 1508, 1468, 1240, 1178, 1109, 1035, 1010, and 825 cm^{-1} have decreased to a great extent.

When comparing sample C with sample A before spectra it can be noticed that all the same peaks are present in both sample spectra but the peaks are higher in the case of sample C. The most important difference is that in the sample C spectra the peak due to hydroxyl or amine groups is clearer indicating a larger amount of these groups in the sample. Again the peak at around 990 cm^{-1} appears in the spectra of after samples, which is due to revealing of the glass fibre. The situation is similar to the artificially damaged coated samples.

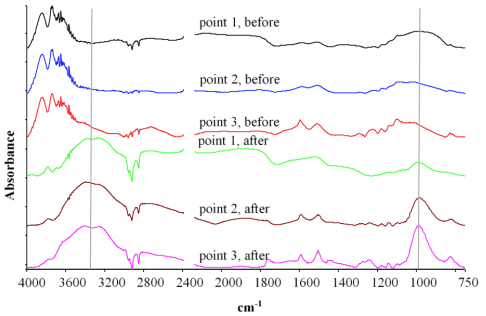

Figure 18. ATR-FTIR spectra of the sample A before and after the test on three different positions. Some interesting peaks are marked with grey bar.

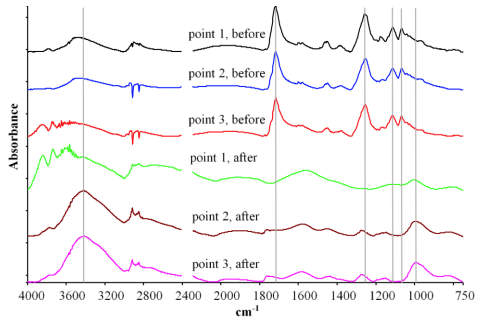

Figure 19. ATR-FTIR spectra of the sample B before and after the test on three different positions. Some interesting peaks are marked with grey bar.

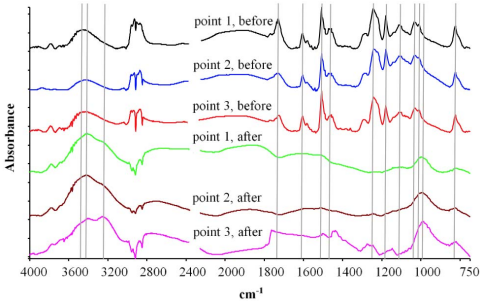

Figure 20. ATR-FTIR spectra of the sample C before and after the test on three different positions. Some interesting peaks are marked with grey bar.

Figure 21 illustrates the ATR-FTIR spectra of sample D. There are some similarities between the spectra of sample C and D, which are due to the alkyd lack used in both samples. Differences such as strong peaks at 1508 and at 1178 cm^{-1} are missing from the spectra of sample D because of different outer layer resins. When comparing sample D before and after spectra, attenuation of the peaks that can be linked to the covering resin can be observed. In addition a

broad new peak centered at 3360 cm^{-1} (absorbed water) and at 988 cm^{-1} can be seen. However, this last new peak (because of the glass fibre) can be seen only in the spectrum of point 3. This can be explained by the fact that the outer layer of sample D was dramatically damaged and the ATR crystal of the microscope has certain, rather small dimensions causing a possibility for the spectra to be recorded randomly from spots where the glass fibre is exposed and from spots where it is not.

The spectra of uncovered samples A, E, and F should be quite similar, however, especially a peak at 1725 cm^{-1} is present in the spectra of samples E and F but not in the spectrum of sample A. This peak should come from the carbonyl compound (aldehyde or carboxylic acid) but it can also be due to acid anhydride. Acid anhydride is a cyclic diketone and commonly used for the curing of epoxy resins. This peak does not fit well in the structure of epoxy resin, but in this case, it can be due to the acid anhydride. Therefore, a different curing agent must have been used in sample A epoxy. Using diamines as the curing agent would give C-N bonds between epoxy resins whereas anhydride would give C-C bonds, which are slightly stronger than the C-N bonds and would therefore result in an epoxy polymer that is, in theory, stable in somewhat higher temperatures. Again, when comparing sample E before and after spectra, new peaks can be found. A broad peak centered at 3398 cm^{-1} is likely due to water absorption, and peak at 985 cm-1 due to the exposed glass fibre. Indeed, the carbonyl peak at 1725 cm^{-1} and the peaks at 1157 and 1020 cm^{-1} in before sample spectra have disappeared almost completely indicating strong degradation of the epoxy polymer.

In Figure 23, the peaks at 1606, 1508, and 1455 cm^{-1} can be linked to structures formed in the curing reaction of the epoxy resin with acid anhydride. They are also present in the spectra of sample E before the tests, but only as somewhat weaker. All peaks at 1302, 1220, 1180, 1157, and 830 cm^{-1} can be found from both samples F and E before spectra and attributed to the skeletal structure of the general epoxy polymer. The chemistries of samples E and F seem to be very alike. Similarly as in all other samples, the peaks caused by the epoxy polymer structure are strongly reduced or disappeared here as well in the spectra of after samples indicating chemical degradation and removal of the epoxy polymer. A broad peak centered at 3256 cm^{-1} reflects water absorption and a peak at 988 cm^{-1} exposure of the glass fibre reinforcement.

In general, the interpretation of the ATR-FTIR spectra and the comparison of the samples before and after the tests reveal degradation and removal of the epoxy polymer. This process takes place even though some samples were protected with extra layers. Mailhot et al. [16] have studied the degradation of epoxy resin under elevated temperature. However, similar degradation products could not be detected in this study. This may be due to the harsher test conditions, which would have always completely removed all these smaller molecular compounds from the samples. Instead, clear water absorption could be seen in all samples with the FTIR. Degradation of epoxy insulation material was also reported by Lim and Lee in their study [17]. They concluded that carboxylic acids were formed during the experiments at elevated temperatures in contact with water as a result of the presence of oxygen. These chemicals would have then caused more polymer degradation. Most small carboxylic acid compounds would evaporate at the temperatures used in our study and could not be detected any more in the samples after the test.

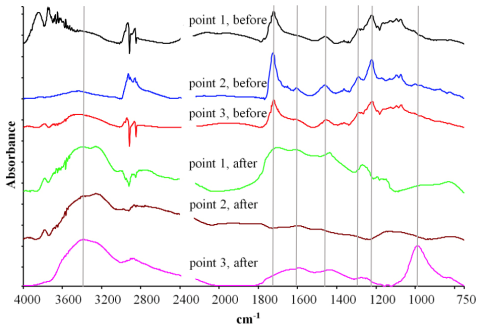

Figure 21. ATR-FTIR spectra of the sample D before and after the test on three different positions. Some interesting peaks are marked with grey bar.

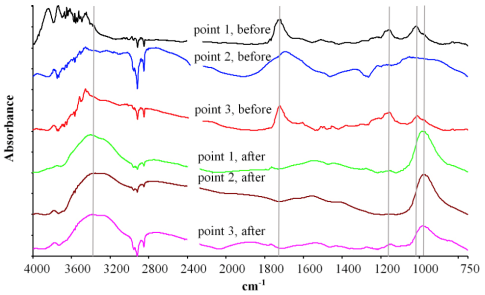

Figure 22. ATR-FTIR spectra of the sample E before and after the test on three different positions. Some interesting peaks are marked with grey bar.

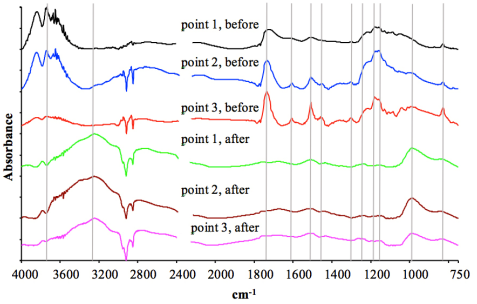

Figure 23. ATR-FTIR spectra of the sample F before and after the test on three different positions. Some interesting peaks are marked with grey bar.

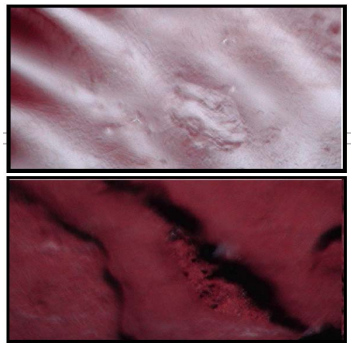

Figure 24. Microscope photo of the sample C before (top) and after the aging test (bottom).

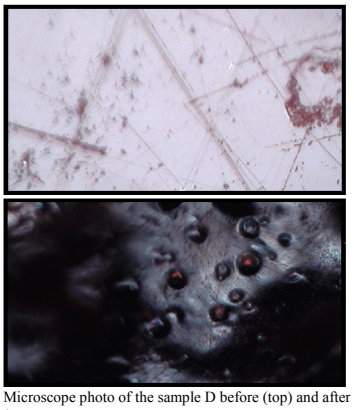

Figure 25. Microscope photo of the sample D before (top) and after the aging test (bottom).

Figures 24 and 25 show the microscope photos of samples C and D before and after the test. The photos are made in exactly the same points by the spectroscope. The large spots in the top figures are caused by the FTIR spectroscope sensor. The outer coating layer of sample C is well preserved even after the 500 h test. Figure 25 illustrates the dramatic changes of the sample D outer epoxy layer.

3.4 WEDGE SAMPLE AGING

The uncoated sample A is the base material for samples B, C, and D. After the 300 h test, the relative mass and volume increase of this material was about 2 %. The visual and FTIR analysis results verify the reliable operation of the other samples based on sample A in the case of the coating integrity breach.

Samples B and C have shown a similar behavior. The relative mass increase was lowest compared to other samples. Samples B and C changed their colour, and the coating became thinner. These samples meet the Class 130 requirements, even in the case when their coating is damaged during the installation process. Samples B and C are suitable for the long time reliable operation in the 120 °C steam atmosphere.

The outer coating layer of sample D became brittle after every test. In spite of the fact that sample D has retained its properties after the 500 h test, it is not recommended to use this type of material as the irreversible changes of the alkyd phenolic varnish may cause some damage in the machine, for instance in bearings.

The relative mass and volume increase of sample E was above 3.5 % in the 300 h test. Some signs of degradation have also appeared on its surface, which is confirmed by its ATR-FTIR spectra. It is not recommended to use this wedge material without coating in a steam atmosphere.

Sample F was delaminated after the 150 h test, and in spite of the high temperature class, it is not suitable for operation in a steam atmosphere.

To sum up, according to the test results, sample C has shown a superior performance to the other tested samples. Sample C was brush painted with alkyd lack and dipped in epoxy resin, which contains styrene, xylene, bisphenol F epoxy, and 2-ethylexyl glycidyl ether.

4 CONCLUSION

The electrical machines operating in a harsh environment, for instance, in superheated steam, require special insulation materials. In this paper, several magnetic slot wedge materials with different coatings were tested.

Laminated wedges are not suitable for the required application because of the delamination. This holds also in a case where the temperature class of the laminated wedge is higher than the steam temperature.

The alkyd lack protects the wedge base material well but dissolves in steam. Therefore, a wedge material that retained its properties and absorbed less water compared to the other materials was selected.

Utmost care must be taken when selecting the epoxy coating. Further research of the epoxy components affecting the coating degradation will be conducted.

Non-laminated wedges are capable of tolerating steam without any coating for some time. Possible coating damage during the wedge installation process will not break the wedge in superheated steam.

ACKNOWLEDGMENT

The authors wish to thank Dr. Liisa Puro and Mr. Jarkko Kuivanen for the FTIR analysis and Mr. Juha Karppinen for the test installation assembly.

REFERENCES

[1] D. Gerada, A. Mebarki, N. L. Brown, C. Gerada, A. Cavagnino, S. Member, and A. Boglietti, "High-Speed Electrical Machines : Technologies , Trends , and Developments," IEEE Trans. Ind. Electron., Vol. 61, No. 6, pp. 2946–2959, 2014.

[2] A. Tenconi, S. Vaschetto, and A. Vigliani, "Electrical Machines for High-Speed Applications: Design Considerations and Tradeoffs," IEEE Trans. Ind. Electron., Vol. 61, No. 6, pp. 3022–3029, 2014.
[3] R. Soltani, E. David, and L. Lamarre, "Impact of humidity on dielectric response of rotating machines insulation system," IEEE Trans. Dielectr. Electr. Insul., Vol. 17, No. 5, pp. 1479–1488, 2010.
[4] A. Shimada, M. Sugimoto, H. Kudoh, K. Tamura, and T. Seguchi, "Degradation mechanisms of silicone rubber (SiR) by accelerated ageing for cables of nuclear power plant," IEEE Trans. Dielectr. Electr. Insul., Vol. 21, pp. 16–23, 2014.
[5] X. Liu, T. Zhang, Y. Bai, X. Ding, and Y. Wang, "Effects of accelerated repetitive impulse voltage aging on performance of model stator insulation of wind turbine generator," IEEE Trans. Dielectr. Electr. Insul., Vol. 21, pp. 1506–1515, 2014.
[6] M. Refaey and J. Kindersberger, "Factors of influence on surface erosion of epoxy resin exposed to electrical discharges," IEEE Trans. Dielectr. Electr. Insul., Vol. 21, pp. 1198–1206, 2014.
[7] T. Tanaka, "Aging of polymeric and composite insulating materials aspects of interfacial performance in aging," IEEE Trans. Dielectr. Electr. Insul., Vol. 9, No. 5, pp. 704–716, 2002.
[8] F. Gholamian, S. Ghariban-Lavasani, M. M. Garshasbi, M. Ansari, F. Bataghv, A. Moraveji, and Z. Ranjbar, "The effects of water absorption and surface treatment on mechanical properties of epoxy nanocomposite using response surface methodology," Polym. Bull., Vol. 70, pp. 1677–1695, 2013.
[9] C. Z. C. Zou, J. C. Fothergill, and S. W. Rowe, "The effect of water absorption on the dielectric properties of epoxy nanocomposites," IEEE Trans. Dielectr. Electr. Insul., Vol. 15, pp. 106–117, 2008.
[10] A. Fukuda, H. Mitsui, Y. Inoue, and K. Goto, "The influence of water absorption on dielectric properties of cycloaliphatic epoxy resin," IEEE 5th Int'l. Conf. Prop. Appl. Dielectr. Mater., Vol. 1, pp. 58–61, 1997.
[11] T. P. Hong, O. Lesaint, and P. Gonon, "Water absorption in a glass-mica-epoxy composite - [I: Influence on Electrical Properties]," IEEE Trans. Dielectr. Electr. Insul., Vol. 16, No. 1, pp. 1–10, 2009.
[12] V. Sihvo, J. Nerg, and J. Pyrhönen, "Insulation system and thermal design of a hermetically sealed turbo-generator operating in a small-power CHP plant," IEEE Int'l Conf. Clean Electr. Pow., ICCEP, pp. 45–50, 2007.
[13] J. Kappatou, C. Gyftakis, and A. Safacas, "A Study of the Effects of the Stator slots wedges material on the Behavior of an Induction Machine," IEEE Int'l Conf. Electr. Mach., ICEM, pp. 1–6, 2008.
[14] T. R. Gaerke and D. C. Hernandez, "The temperature impact of magnetic wedges on TEFC induction motors," IEEE Trans. Ind. Appl., Vol. 49, No. 3, pp. 1228–1233, 2013.
[15] V. Sihvo, A. Pihlajamäki, J. Nerg, S. Hvidsten, O. Kvien, and L. Brenne, "Effects of raw natural gas on the aging of high-voltage electrical machine mainwall insulation," IEEE Trans. Dielectr. Electr. Insul., Vol. 19, No. 3, pp. 893–902, 2012.
[16] B. Mailhot, S. Morlat-Thérias, M. Ouahioune, and J. L. Gardette, "Study of the degradation of an epoxy/amine resin, 1 photo- and thermo-chemical mechanisms," Macromol. Chem. Phys., Vol. 206, No. 5, pp. 575–584, 2005.
[17] K. Lim and D. Lee, "Study of the Surface Degradation Mechanism of an Epoxy Insulator Exposed to Water," J. Korean Phys. Soc., Vol. 37, No. 1, pp. 49–54, 2000.

Nikita Uzhegov (S'14-M'15) received the B.Sc. degree from Moscow Power Engineering Institute (MPEI), Moscow, Russia, in 2010 and the M.Sc. degree in electrical engineering from Lappeenranta University of Technology (LUT), Lappeenranta, Finland, in 2012. He is currently a Doctoral Student in the Department of Electrical Engineering, LUT. His research mainly concerns electrical machines and drives, particularly high-speed machines.

Arto Pihlajamäki was born in Isokyrö, Finland in 1966. He graduated M.Sc. in chemical technology in 1992 from Lappeenranta University of Technology. In 1998 he received D.Sc. degree in Membrane Technology also from Lappeenranta University of Technology.
Currently he works as Researcher/Teacher in the LUT School of Engineering Science. He also holds docentship with special research area of characterization of membrane surfaces.

Janne Nerg (M'99-SM'12) received the M.Sc. degree in electrical engineering, the Licentiate of Science (Technology) degree, and the D.Sc. (Technology) degree from Lappeenranta University of Technology (LUT), Lappeenranta, Finland, in 1996, 1998, and 2000, respectively.
He is currently an Associate Professor in the Department of Electrical Engineering at LUT. His research interests are in the field of electrical machines and drives, especially electromagnetic and thermal modeling and design of electromagnetic devices.

Juha J. Pyrhönen (M'06) was born in 1957 in Kuusankoski, Finland. He received the Doctor of Science (D.Sc.) degree from Lappeenranta University of Technology (LUT), Finland in 1991. He became an Associate Professor of Electrical Engineering at LUT in 1993 and a Professor of Electrical Machines and Drives in 1997. He is engaged in research and development of electric motors and power-electronic-controlled drives. Prof. Pyrhönen has wide experience in the research and development of special electric drives for distributed power production, traction drives and high-speed applications. Permanent magnet materials and applying them in machines have an important role in his research. Currently he is also researching new carbon-based materials for electrical machines.

Publication VII

Pyrhönen, J., Ruoho, S., Nerg, J., Paju, M., Tuominen, S., Kankaanpää, H., Stern, R., Boglietti, A, and Uzhegov, N.

Hysteresis Losses in Sintered NdFeB Permanent Magnets in Rotating Electrical Machines

Reprinted with permission from
IEEE Transactions on Industrial Electronics,
vol. 62, no. 2, pp. 857–865, Feb. 2015

Hysteresis Losses in Sintered NdFeB Permanent Magnets in Rotating Electrical Machines

Juha Pyrhönen, *Member, IEEE*, Sami Ruoho, *Member, IEEE*, Janne Nerg, *Senior Member, IEEE*, Martti Paju, *Member, IEEE*, Sampo Tuominen, Harri Kankaanpää, Raivo Stern, Aldo Boglietti, *Fellow, IEEE*, and Nikita Uzhegov, *Student Member, IEEE*

***Abstract*—Permanent magnet (PM) materials are nowadays widely used in the electrical machine manufacturing industry. The eddy-current loss models of PMs used in electrical machines are frequently discussed in research papers. In magnetic steel materials we have, in addition to eddy-current losses, there are hysteresis losses when alternating current or a rotating flux travels through the material. Should a similar phenomenon be also taken into account in calculating the losses of PMs? Every now and then, authors seem to assume that some significant hysteresis losses are present in rotating machine PMs. This paper studies the mechanisms of possible hysteresis losses in PMs and their role in PMs when used in rotating electrical machines.**

***Index Terms*—Hysteresis, hysteresis in permanent magnets (PMs), PM, PM losses, PM material.**

I. Introduction

PERMANENT MAGNET (PM) materials are widely used in electrical machines. The applications where PM machines are utilized include, e.g., industrial machines, wind power generators, traction motors, linear machines, high-speed machinery, and machines used in aerospace applications [1]–[6].

The eddy-current loss models of PMs used in electrical machines are frequently discussed in research papers. Sintered PM materials have a significant macroscopic resistivity, which is in the range of 100–200 $\mu\Omega$cm, providing eddy currents with paths to run and produce losses. In some cases, when using bulky sintered magnets assembled on the rotor surface, the eddy-current losses can be very high that the polarization of the magnet material is lost because of the high operating temperature in the magnets. Magnet segmentation is suggested to limit the eddy-current losses in PM materials in the same way as they are limited in the magnetic steel cores of machines made of laminations. In practice, the resistivities of magnetic steel sheets are about half of the resistivities of sintered NdFeB magnets. This fact indicates that the eddy-current losses can be considerably high in bulky magnets if an alternating flux is traveling through the magnets. There are numerous studies about the eddy-current losses in sintered NdFeB and SmCo magnets, and the scientific community is nearly unanimous about the nature of the eddy-current losses and their calculation in PMs [7]–[10].

However, every now and then, authors claim that, besides the eddy-current losses, hysteresis losses also occur in the NdFeB PM material utilized in rotating-field PM machines without comprehensively explaining the mechanism of creating hysteresis losses in PMs. The aim of this paper is to comprehensively study the possibility of hysteresis losses in sintered NdFeB PMs used in rotating-field PM machines. This paper is organized as follows. The theoretical background of the polarization behavior of NdFeB magnets is given in Section II. Section III discusses the hysteresis behavior in NdFeB magnets. The experimental results from some extra high-accuracy measurements confirming the understanding of NdFeB magnet material hysteresis in practice are presented in Section IV. Section V discusses the role of PM material hysteresis in rotating-field PM machines utilizing a multiple-pole PM traction machine and a two-pole rotor-surface-magnet synchronous machine as examples.

The main contributions of this paper are the following. Based on the measurements, it is shown that a prerequisite for significant hysteresis losses in sintered NdFeB is the variation of the sign in the magnetic field strength acting on the PM material. In carefully designed rotating-field PM machines, the PM material operates in the second quadrant of the magnetization curve, and it could be concluded that hysteresis losses cannot play an important role in them. However, it is also shown that, in PM machines having a strong armature reaction, part of the magnets, at certain loads, operate at flux densities where hysteresis losses can be present.

II. Theoretical Background

In soft magnetic materials, polarization J varies as flux density B varies. The changing of the polarization includes

Manuscript received October 31, 2013; revised March 14, 2014, June 18, 2014, and July 21, 2014; accepted August 15, 2014. Date of publication September 4, 2014; date of current version January 7, 2015.

J. Pyrhönen, J. Nerg, and N. Uzhegov are with the Department of Electrical Engineering, LUT Energy, School of Technology, Lappeenranta University of Technology (LUT), 53851 Lappeenranta, Finland (e-mail: juha.pyrhonen@lut.fi; janne.nerg@lut.fi; nikita.uzhegov@lut.fi).

S. Ruoho is an independent researcher (e-mail: samiruoho@hotmail.com).

M. Paju and S. Tuominen are with the Magnet Technology Centre, Prizztech Oy, 28101 Pori, Finland (e-mail: martti.paju@prizz.fi; sampo.tuominen@prizz.fi).

H. Kankaanpää is with Neorem Magnets Oy, 28400 Ulvila, Finland (e-mail: harri.kankaanpaa@neorem.fi).

R. Stern is with the Department of Chemical Physics, National Institute of Chemical Physics and Biophysics, 12618 Tallinn, Estonia (e-mail: raivo.stern@kbfi.ee).

A. Boglietti is with the Department of Electrical Engineering, Politecnico di Torino, 10129 Turin, Italy (e-mail: aldo.boglietti@polito.it).

Color versions of one or more of the figures in this paper are available online at http://ieeexplore.ieee.org.

Digital Object Identifier 10.1109/TIE.2014.2354597

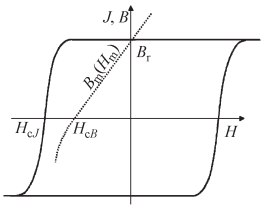

Fig. 1. Behavior of polarization $J(H)$ and the corresponding BH behavior of a modern industrial-use PM material. In positive external H-fields and in low demagnetizing H-fields, the polarization J of the magnet material remains constant. If the demagnetizing field gets a high enough value, the polarization of the PM material changes its sign.

frictionlike phenomena and, therefore, produces losses. In ideal PM materials to be used in rotating machinery, polarization J remains constant under the influence of varying, but all the time demagnetizing, external field strength H. This should leave no space for hysteresis loss.

Ideally, the polarization remains constant until the demagnetizing field reaches such a high level that the polarization of the magnet is irreversibly lost either partially or totally. If the field strength variation is extremely large and varies between high positive and negative values, the polarization curve forms a hysteresis loop similarly as in soft magnetic materials, but the loop is very wide compared with those of soft magnetic materials. Fig. 1 illustrates the principal behavior of the polarization in a PM material under a high variation in the field strength.

The traditional BH curve of the material is also given. In the second quadrant, the curve is called the demagnetization curve of the material. In an ideal case, the demagnetization curve is a straight line between the remanent flux density B_r and coercive force H_{cB}.

If the polarization remains absolutely constant, the material has exactly the same permeability as a vacuum (μ_0), and the PM material's recoil permeability is $\mu_r = 1$. However, in practical NdFeB magnets in the region of the second quadrant on the BH curve, the recoil permeability is in the range of $\mu_r = 1.04$, exhibiting some soft magnetic material behavior. It must be borne in mind that hysteresis is possible only if the relative permeability is $\mu_r > 1$.

In real PM materials (or real soft magnetic materials), full saturation is practically never attained because the small nuclei of domains or spin fluctuations persist even after the application of very high fields [11]. This means that, in real PMs, there are some soft-phase areas found in addition to the hard magnet phase, and the polarization of the material can therefore slightly change as the practical recoil permeability of the BH curve in NdFeB magnets is, for instance, 4% higher than that of vacuum ($\mu_r = 1.04$ instead of 1.00), thus allowing, at least in principle, some hysteresis for the PM material. Fig. 2 illustrates the change in the polarization because of this nonideality. Permeability μ_r is a function of H, which includes possible saturation, and μ_r can also depend on the BH history, which is shown as hysteresis.

The real polarization behaves as the following line before the irreversible loss of polarization:

$$J_m = B_r + \mu_0(\mu_r - 1)H_m. \tag{1}$$

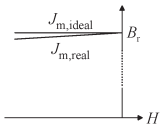

Fig. 2. Ideal and real behavior of the PM polarization in the second quadrant of the JH plane. The polarization slightly changes as a function of demagnetizing field strength H because of the remaining soft magnetic phases in the material.

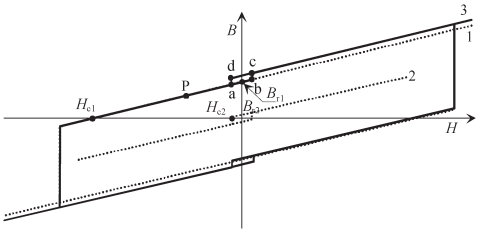

Fig. 3. Three hysteresis curves. (1) Hysteresis curve of an ideal PM material with a remanence B_{r1} and coercivity H_{c1}. (2) Hysteresis curve of a ferromagnetic material thinly scattered in space, with B_{r2} and H_{c2}. (3) Common hysteresis of an alloy mostly containing material 1 and a small proportion of material 2.

Therefore, in the second quadrant area, the incremental flux density curve that could be prone to hysteresis is

$$B_{\mathrm{PM,\,inc}} = \mu_0\,(\mu_r(H,\,\mathrm{history}) - 1)\,H. \tag{2}$$

In the case of NdFeB, $(\mu_r(H,\,\mathrm{history}) - 1) \approx 0.04$, which results in a variation in the flux density subjected to a possible hysteresis phenomenon.

To elucidate the possible hysteresis mechanism in sintered magnets, let us observe a theoretical alloy consisting of two materials having different remanent flux densities B_{r1} and B_{r2} and coercive forces H_{c1} and H_{c2}. If we simplify their hysteresis and saturation behaviors, we get the situation illustrated in Fig. 3.

In principle, curve 3 in Fig. 3 describes the behavior of a sintered NdFeB magnet. Curve 1 depicts the 100% polarized PM phase of the magnet. Curve 2 indicates the significantly softer material behavior having low remanence and coercivity. In principle, this material describes the soft phases of NdFeB magnets that have remained inside the fully polarized domains and thereby form a sparse cloud of grains inside the space of the material. Therefore, its apparent permeability is about the permeability of vacuum similarly as the permeability of the hysteresis curve 1, which represents the hard magnetic material. When the hysteresis curves of materials 1 and 2 are combined, a total hysteresis loop 3 is obtained as a result. This curve represents the behavior of the hysteresis of practical sintered NdFeB magnets in a simplified way. The normal working point in a PM machine is shown by point P. If the machine armature reaction is positive, it is possible that the operating point moves from point P toward points a and even b. If point b is reached and the positive field strength H increases further, the material will reach point c. If H will further increase, the flux density

will increase according to the permeability of the material, which is, in practice, μ_0 after saturation. When H gets smaller and goes negative again, the path will run through points c, d, and a towards P again.

The possible hysteresis loss is very sensitive to the polarization hysteresis as the field strength in PMs varies strongly, which is in the range of several hundreds of kiloamperes per meter. Therefore, even the smallest hysteresis in the polarization may result in significant hysteresis losses, particularly at slot-opening-caused permeance variation frequencies.

III. Behavior of Hysteresis in NdFeB Magnets

It should be observed that the hysteresis behavior of NdFeB PM materials is different in nonpolarized and polarized cases. In [11], the hysteresis of an NdFeB material is studied in detail. It is obvious that a demagnetized material also forms minor hysteresis loops. However, in [11], significant minor loops only emerge when the material has experienced significant demagnetization.

The hysteresis loss in PM materials is also studied in [12]. According to Fukuma *et al.*, their results show that a designer should consider not only the eddy-current loss but also the PM hysteresis loss when the frequency of the ac field produced by a slot-caused flux density ripple is of the order of several hundred hertz, which is normally the case in rotor-surface-magnet machines.

The authors refer to [13] with the test procedure. However, the procedure in [12] is questionable from the electrical machine designer point of view. The test is made in such a way that the polarized magnet is magnetically short-circuited, resulting in $H_m \approx 0$ and $B_m \approx B_r$. However, such a condition seldom takes place in electrical machines in their normal operation.

According to the test in [12], the PM hysteresis loss is even significantly larger than the eddy-current loss already at 50 Hz. The magnetic flux density, neglecting any possible hysteresis in the test, behaves as

$$B_m = B_r + \mu_0 \mu_r H_m. \tag{3}$$

In all cases, the amplitude of the ac flux density has been lower than 0.1 T, corresponding to about $H = 76.5$ kA/m and an alternating field strength amplitude of around zero.

As the magnet (Neomax44-H) in the test was magnetically short-circuited, the magnet flux density varied between B_r, i.e., ± 0.1 T. Ruoho and Arkkio [14] have also measured the hysteresis loops of PM materials. Fig. 4 shows the curves measured with a hysteresisgraph showing the recoil behavior of the partially demagnetized NdFeB magnet material.

Starting from $H = 0$, the demagnetizing field strength is first increased on the negative H-axis until partial demagnetization is found. After that, demagnetizing field strength H is decreased back to zero. Then, the negative field strength is again increased to cause more loss of polarization. It can be seen that the recoil curve is clearly bent, but what is significant from the perspective of our study is that there is no observable minor hysteresis loop on the NdFeB recoil curve. The arrows in Fig. 4 show the course of the measurement procedure.

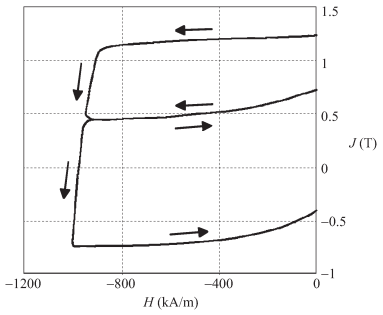

Fig. 4. Partial demagnetization of the NdFeB sample and the recoil behavior of the material in the second and third quadrants of the JH plane. No hysteresis loops are seen. This figure is reproduced by using the original measurement data in [14].

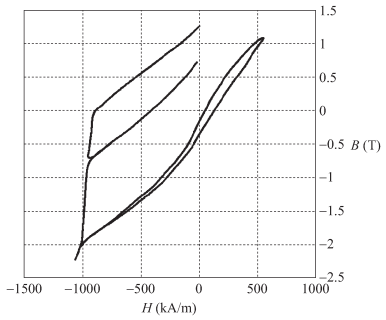

Fig. 5. Recoil curves and a minor loop of the NdFeB magnet sample. A significant minor loop is formed when the sign of the magnetic field strength changes during the recoil operation. In other cases, the possible hysteresis cannot be observed with the accuracy of the measurement. This figure is reproduced by using the original measurement data in [15].

Fig. 5 illustrates the BH behavior of the NdFeB material when the operation takes place between the first and second quadrants, meaning that the external field strength varies its polarization.

Comparing Figs. 4 and 5 convinces us that a prerequisite for significant hysteresis losses in sintered NdFeB magnets seems to be the variation of the sign in the H-field. However, we decided to perform new measurements to observe the behavior of the magnets, particularly in the second quadrant.

IV. Hysteresis Measurements

Some extra high-accuracy measurements were arranged to confirm the understanding of the NdFeB magnet material's hysteresis in practice. As the demagnetizing field strength varies in the range of several hundreds of kiloamperes per meter, even a few millitesla hysteresis in the polarization should cause a significant hysteresis loss in the PMs; therefore, a very careful analysis is needed.

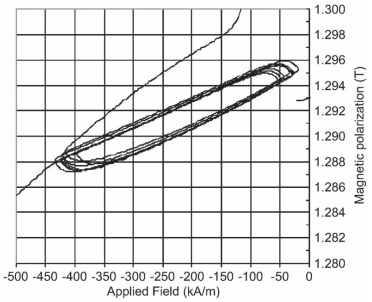

Fig. 6. Measurement result of the NdFeB sample obtained with a hysteresisgraph (Permagraph C-300 by Magnet-Physik) at Neorem Magnets Oy. A clear loop in the JH behavior of the test is found. However, this loop does not look like a hysteresis loop as the polarization changes when the direction of the H-field changes. Instead, the polarization should remain constant. The result most probably comes from the eddy currents in the sample as dH/dt is too high to avoid eddy currents. The smallest possible setting dH/dt was used in the Permagraph C-300.

The measurements of the millitesla-range changes of polarization over the stable polarization of more than 1 T are demanding and easily produce misleading results. The measurements were first performed at the Prizztech Magnet Technology Centre in Pori, Finland, and at Neorem Magnets Oy. The result with the device type Permagraph C-300 manufactured by Magnet-Physik Dr. Steingroever GmbH is shown in Fig. 6. Two different samples of NdFeB were tested.

Fig. 6 shows that there should be polarization hysteresis of about 2 mT in the sample when the external varying field stays negative for the entire time. However, considering possible hysteresis, the form of the hysteresis loop is obviously unnatural. The turning points of the loops at places where the sign of the derivative of the field strength is changed have an unnatural form from the hysteresis point of view. For example, when the field strength increases from -450 to -50 kA/m and then turns more negative again, the polarization keeps on vertically rising, whereas the field strength changes by about -50 kA/m before starting to decrease. A similar behavior is seen at the other end of the loop.

This behavior is unnatural from the hysteresis point of view and is therefore obviously not an indication of PM material hysteresis but an indication of the properties of the hysteresisgraph measurement setup itself, as a result of the eddy currents in the tested bulky material. The minimum dH/dt available by the setup was obviously too high for this measurement. The result, however, is an indication that if there is any hysteresis present, its value should be limited below 2 mT. Nevertheless, this is not a satisfactory result as 2-mT hysteresis should result in large hysteresis losses caused, for instance, by machine-slot-openings-caused permeance harmonics.

The virtual energy covered by the loop in Fig. 6 is about 400 kA/m $\times$ 2 mV $\cdot$ s/m^2 $=$ 800 J/m^3. If the magnet size is, for instance, $50 \times 100 \times 10$ mm^3 and the slotting-caused frequency is 500 Hz, the loss in the single magnet is 20 W. Such a value would be in the same range as the eddy-current loss in the same magnet in the same application. Because of this result, further confirming actions had to be taken.

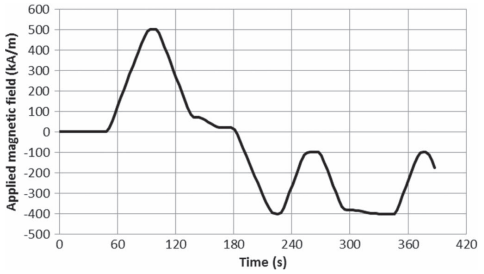

Fig. 7. Behavior of the field strength during the test in Tallinn, Estonia. The H-field very slowly varies to avoid disturbing the eddy currents in the test samples.

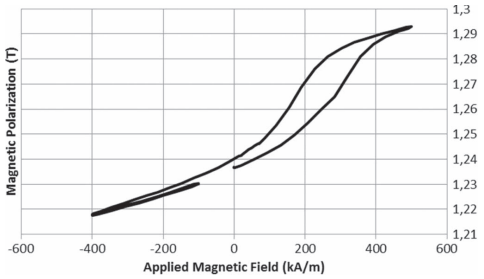

Fig. 8. Measurement result of the NdFeB sample obtained with a hysteresisgraph (the Vibrating Sample Magnetometer of the Physical Property Measurement System by Quantum Design, Inc.). In the first quadrant, we see again the hysteresislike behavior of the sample. However, in the second quadrant, no clear hysteresis is seen when the alternating H-field is applied between -400 and -100 kA/m.

Next, the same samples were sent to Tallinn to the National Institute of Chemical Physics and Biophysics to be measured in an open circuit. Fig. 7 illustrates the field strength behavior in time during the testing of the sample. The magnet material was first driven to the first quadrant by about 500 kA/m, and then, a time-varying field strength between -400 and 100 kA/m was applied.

Fig. 8 illustrates the overall behavior of the polarization in the JH plane. As it was anticipated, there is some hysteresis seen in the first quadrant area of the magnet, where it is normally not working in an electrical machine. In the second quadrant in Fig. 8, there are no visible loops of hysteresis when the alternating H-field is applied.

In Fig. 9, there is an enlarged figure of the polarization behavior; the loops seen are very small that we may conclude that there is, in practice, no hysteresis in this PM material when operated in the second quadrant.

V. Role of PM Hysteresis in Rotating-Field PM Machines

The air gap needed in practical machines results in an apparent negative field strength in the magnet. This opening of the

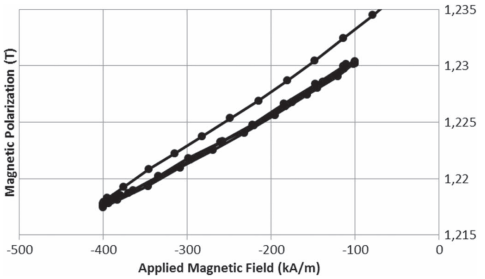

Fig. 9. Enlargement of Fig. 8 in the second quadrant area. The possible loops seen here are negligible. According to this result, there should be no practical hysteresis losses if the PM material remains under a varying H-field all the time in the second quadrant of the JH plane.

magnetic circuit moves the operating point of the magnet from B_r to P in Fig. 3. During normal use, there will be an armature reaction of the machine causing different operating points at different parts of the magnet in such a way that the operating points travel away from point P either in a positive or negative direction with respect to H.

Based on the aforementioned literature analysis and on our own experience about practical PM losses in rotating machines, it seems that there is a good opportunity to avoid PM hysteresis losses in electrical machines. The results measured in literature [12], [13] are obviously correct, but the interpretation with regard to rotating machines may not be correct.

When a PM material is used in a rotating electrical machine, the magnetic circuit is always physically opened by the machine air gap and further magnetically opened by the magnetic voltage drop in the iron circuit. Often, a slightly demagnetizing stator current component even further decreases the operating point flux density in the magnet. These conditions should guarantee that, in practice, the external H-field never passes to the positive side in the magnet external H-field.

However, the dimensioning rules and a strong armature reaction in high-torque applications may cause a risk to some areas in the magnets of experiencing flux densities close to the remanent flux density of the material. This has to be studied further.

The most efficient use of the magnet material is found at $BH_{\max}$, which corresponds to the operating point magnetic flux density of $B_m = B_r/2$. For other reasons, however, the air-gap flux density of PM machines is normally selected much higher than half of remanent flux density B_r. In the case of the wasteful use of the PM material, operating point B_m can reach even $B_m = 0.8{-}0.9\,B_r$ at no load. At no load in electrical machines, the PM flux density remains lower than B_r in all practical cases.

To observe such behavior in more detail, a finite-element analysis was performed for a 25-kW PM synchronous machine (PMSM) with pseudorotor surface magnets. The dimensions and details of the test machine are presented in [1]. Fig. 10 illustrates the machine pole geometry, and Fig. 11 presents the magnetic flux behavior under a nominal torque condition, where the armature reaction is strongly affecting the PM flux densities.

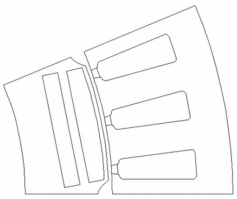

Fig. 10. Multiple-pole traction motor pole studied for hysteresis losses. Each pole carries two embedded magnets. The topmost magnet, however, behaves almost similar to a rotor surface magnet as the magnet-retaining bridge is very thin.

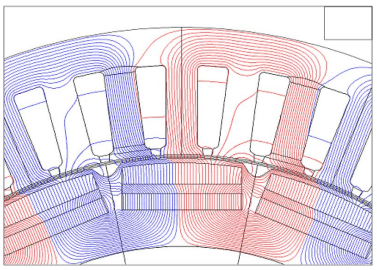

Fig. 11. Flux plot of the test machine under rated torque.

The NdFeB magnet material used in the machine has a remanent flux density of $B_r = 1.17$ T at an operating temperature of 100 °C. At no load, the upper PM flux density is about 0.8 T, which is 70% of the remanent flux density.

At the rated operating point, the armature reaction affects the upper magnet in such a way that when the torque is counterclockwise, the upper magnet's left corner gets a higher flux density, and the upper magnet's right corner gets a lower flux density similarly as in no load (see Fig. 11).

If we compare this with Fig. 3, the left-corner PM operating point moves right from point P when the machine is loaded, and the right-corner PM operating point moves left from point P. The permeance harmonics are then further modulating the flux densities in these points according to Figs. 12 and 13.

As Fig. 12 illustrates, the flux density of the upper magnet's leftmost corner varies between 0.86 and 1.07 T when the armature-reaction-intensified flux density is modulated by the slot openings.

Correspondingly, Fig. 13 illustrates how the armature reaction makes the average value of the flux density lower in the rightmost corner than in the leftmost corner. The slot-frequency-caused variation now takes place between the values 0.57 and 0.60 T.

In both of these cases, the flux density of the magnet clearly remains at lower values than remanent flux density B_r, meaning that the BH or JH operation of the magnet clearly remains in the second quadrant.

This machine, however, has quite a low magnetizing inductance, and as a result, the armature reaction is limited so that, under normal operation, no magnet operates beyond the remanent flux density. In such a case, there will be no

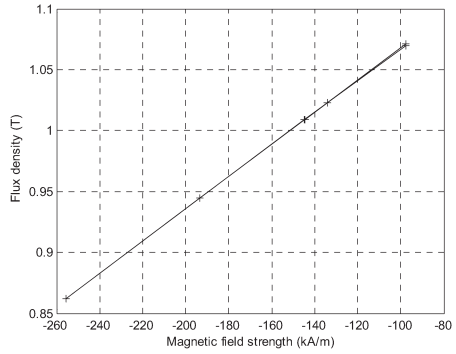

Fig. 12. Flux density variation in the leftmost corner of the upper magnet under the influence of the rated point armature reaction and the flux density modulation caused by the slot openings. The rated motoring torque is produced counterclockwise.

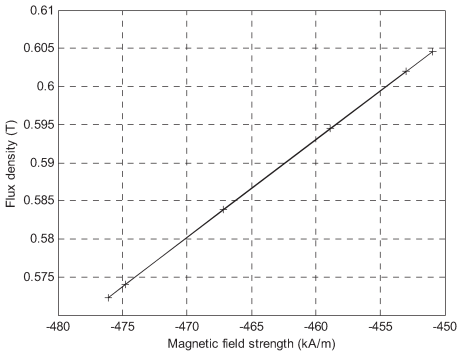

Fig. 13. Flux density variation in the rightmost corner of the upper magnet under the influence of the rated point armature reaction and the flux density modulation caused by the slot openings. The rated motoring torque is produced counterclockwise.

hysteresis losses in the magnets. We shall, however, enlarge our studies to a two-pole rotor-surface-magnet PM machine that is deliberately designed to have a high magnetizing inductance and, therefore, a high armature reaction. Fig. 14 illustrates the flux density distribution in PMs at the rated load.

The variation of flux-density-indicating colors shows the strong influence of the armature reaction in the magnets. If we observe the upper PM pole, its flux density clearly exceeds the remanent flux density of the magnet on the left, whereas a significantly reduced flux density is shown on the right. In the center of the pole, there are magnets that operate very close to the remanent flux density, and as we have used open slots in the calculation, the high permeance variations modulate the flux density in the magnets so that the operating points in the magnets travel across the B-axis; those magnets are prone to hysteresis losses. Fig. 15 illustrates the traveling of the flux density in the topmost magnet in Fig. 14.

Figs. 16 and 17 illustrate the traveling of the flux density in the leftmost and rightmost magnets in Fig. 14, respectively.

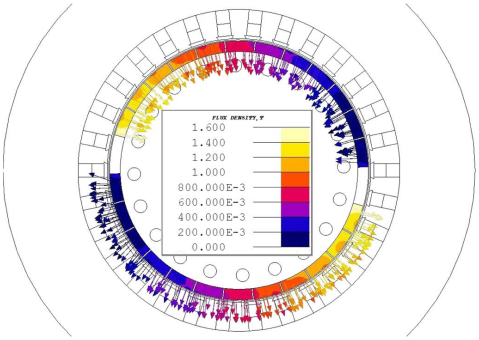

Fig. 14. Flux solution of a rotor-surface-magnet PMSM with a high armature reaction at the rated load.

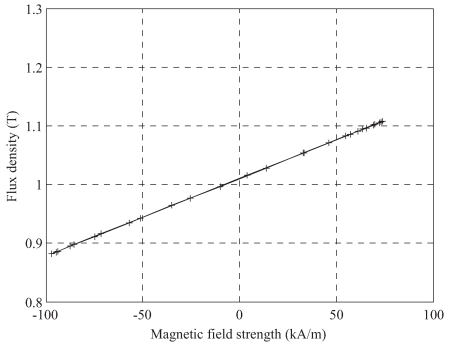

Fig. 15. Flux density variation in the top centermost magnet in Fig. 14. The flux density travels across the B-axis via the remanent flux density of the material ($B_r = 1.01$ T). Hysteresis is not seen as the software used in the calculations does not support such a solution. However, in reality, this magnet should, in addition to eddy-current losses, also suffer from hysteresis losses, and the total magnet losses could be significant. A 1–2-mT-high hysteresis loop should result.

Observing the leftmost magnet shows that its flux density and magnetic field strength vary between 1.14 and 1.28 T, with a field strength of $+100$–$+200$ kA/m. This magnet always stays at this load in the first quadrant and does not experience hysteresis loss. Observing the rightmost magnet shows a flux density variation between 0.19 and 0.23 T with -620–-587 kA/m. This magnet is heavily demagnetized and always stays at this load in the second quadrant, experiencing no hysteresis loss.

The no-load PM flux density is naturally in the second quadrant, and no hysteresis loss will take place. However, as the load increases, the armature reaction starts increasing the flux density at the northwest and southeast edges of the magnets. As a result, first, the top leftmost magnets' operating point reaches, in average, the remanent flux density level, and as the load increases, a similar operation point starts traveling toward the centermost magnet. Therefore, at higher loads, there are always some magnets that experience flux density traveling across the B-axis, i.e., the change of the sign of the H-field, and experience hysteresis losses. The height of the hysteresis loop

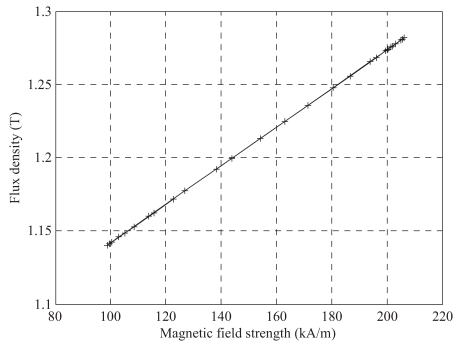

Fig. 16. Flux density variation in the leftmost magnet in Fig. 14.

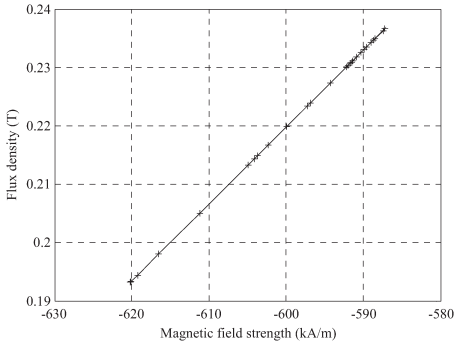

Fig. 17. Flux density variation in the rightmost magnet in Fig. 14.

should be about $\Delta B = 1{-}2$ mT, whereas $\Delta H = 175$ kA/m. Each cycle creates a hysteresis loss density of $175{-}350$ J/m^3 in the magnets. In this case, the machine operates at 50 Hz. As the number of slots is $Q_s = 30$, the slot frequency shall be $f_s = 1500$ Hz. Now, the hysteresis specific power should be in the range of $267{-}525$ kW/m^3. The magnet dimensions, i.e., the width, the height, and the length, are 25, 10, and 400 mm, respectively. In the magnet with a clear hysteresis loop in itself, there should be even $25{-}50$ W hysteresis loss. Such a design should be, naturally, avoided.

VI. Conclusion

The hysteresis behavior of sintered NdFeB PM materials when applied in the design of rotating electrical machines was studied. Normally, only eddy-current losses have been considered the sources of losses in these magnets, and possible hysteresis losses have been ignored. However, for instance, Fukuma *et al.* [12] claim that significant hysteresis losses also occur in PMs.

In practice, however, to have a clear minor loop in a PM material, the crossing of the J-axis (or the B-axis) with a positive H-field is needed to see clear hysteresis behavior in NdFeB materials. This is normally not the case in rotating electrical machines as they are designed in a way that the BH behavior in the magnet takes place in the second quadrant of the PM material's hysteresis loop.

After reevaluating the literature results and based on our own measurement results, we are convinced that hysteresis losses in carefully designed machines play no significant role in PM materials when normally used in rotating machines, as the PM materials, in practice, always operate in the second quadrant of the BH curve and no crossing of the J-axis, enabling clear hysteresis behavior, takes place. However, for instance in the utmost conditions in the traction motor used as an example during the highest accelerating torque values, the crossing of the J-axis may also take place, resulting in hysteresis losses in the magnets. Such a condition cannot, however, last for a long period of time as the copper losses under high accelerations are also very large that the machine windings rapidly heat up and the drive has to return to the normal operating range, where no crossing of the J-axis certainly takes place.

In addition, this paper has been also based on several test machines and an evaluation of the PM losses in them. For example, in [16], we tested an axial-flux tooth-coil open-slot machine with bulky or laminated magnets. In this case, the slot openings were very wide, and the flux density dips caused by them were very large. The losses, however, were reduced according to the eddy-current loss theory, and no significant hysteresis loss could have been included in the loss analysis. The hysteresis loss is about constant independent of the magnet lamination thickness. In [11], the losses dramatically decreased when laminated magnets were used instead of bulky magnets. This is another practical indication of the nonexistence of significant hysteresis losses in carefully designed rotating electrical machinery.

However, in machines with a high per-unit magnetizing inductance, the armature reaction may bring the PM material's operating point close or even beyond the remanent flux density of the PM material. Two-pole PM machines clearly belong to the machine in which there is a risk of hysteresis losses in PMs if the machine is not correctly designed. It is the task of the designer to carefully analyze the armature reaction effects on the PMs, and if the machine tries, in a normal operation, to bring some of its magnets to hysteresis loss danger, it is important to redesign the machine. In normally designed and operated PM electrical machines, in which the magnets operate in the second quadrant of the JH curve, hysteresis losses play no important role and can be neglected in practice.

References

[1] J. Nerg, M. Rilla, V. Ruuskanen, J. Pyrhönen, and S. Ruotsalainen, "Direct-driven interior magnet permanent magnet synchronous motors for a full electric sports car," *IEEE Trans. Ind. Electron.*, vol. 61, no. 8, pp. 4286–4294, Aug. 2014.

[2] P. Lindh, J. Montonen, P. Immonen, J. A. Tapia, and J. Pyrhönen, "Design of a traction motor with tooth-coil windings and embedded magnets," *IEEE Trans. Ind. Electron.*, vol. 61, no. 8, pp. 4306–4314, Aug. 2014.

[3] T. Baumgartner, R. M. Burkart, and J. W. Kolar, "Analysis and design of a 300-W 500 000-r/min slotless self-bearing permanent-magnet motor," *IEEE Trans. Ind. Electron.*, vol. 61, no. 8, pp. 4326–4336, Aug. 2014.

[4] T. D. Kefalas and A. G. Kladas, "Thermal investigation of permanent-magnet synchronous motor for aerospace applications," *IEEE Trans. Ind. Electron.*, vol. 61, no. 8, pp. 4404–4411, Aug. 2014.

[5] R. S. Semken *et al.*, "Direct-drive permanent magnet generators for high-power wind turbines: Benefits and limiting factors," *IET Renew. Power Gen.*, vol. 6, no. 1, pp. 1–8, Jan. 2012.
[6] K. Kamiev, J. Pyrhönen, J. Nerg, V. Zaboin, and J. Tapia, "Modeling and testing of an armature-reaction-compensated (PM) synchronous generator," *IEEE Trans. Energy Convers.*, vol. 28, no. 4, pp. 849–859, Dec. 2013.
[7] F. Dubas and A. Rahideh, "Two-dimensional analytical permanent-magnet eddy-current loss calculations in slotless PMSM equipped with surface-inset magnets," *IEEE Trans. Magn.*, vol. 50, no. 3, p. 6300320, Mar. 2014.
[8] B. Aslan, E. Semail, and J. Legranger, "General analytical model of magnet average eddy-current volume losses for comparison of multiphase PM machines with concentrated winding," *IEEE Trans. Energy Convers.*, vol. 29, no. 1, pp. 72–83, Mar. 2014.
[9] S.-H. Han, T. Jahns, and Z. Zhu, "Analysis of rotor core eddy-current losses in interior permanent-magnet synchronous machines," *IEEE Trans. Ind. Appl.*, vol. 46, no. 1, pp. 196–205, Jan./Feb. 2010.
[10] N. Bianchi, S. Bolognani, and E. Fornasiero, "An overview of rotor losses determination in three-phase fractional-slot PM machines," *IEEE Trans. Ind. Appl.*, vol. 46, no. 6, pp. 2338–2345, Nov./Dec. 2010.
[11] G. A. Jubb and R. A. McCurrie, "Hysteresis and magnetic viscosity in a Nd–Fe–B permanent magnet," *IEEE Trans. Magn.*, vol. 23, no. 2, pp. 1801–1805, Mar. 1987.
[12] A. Fukuma, S. Kanazawa, D. Miyagi, and N. Takahashi, "Investigation of AC loss of permanent magnet of SPM motor considering hysteresis and eddy-current losses," *IEEE Trans. Magn.*, vol. 41, no. 5, pp. 1964–1967, May 2005.
[13] H. Domeki *et al.*, "Investigation of benchmark model for estimating iron loss in rotating machine," *IEEE Trans. Magn.*, vol. 40, no. 2, pp. 794–797, Mar. 2004.
[14] S. Ruoho and A. Arkkio, "Partial demagnetization of permanent magnets in electrical machines caused by an inclined field," *IEEE Trans. Magn.*, vol. 44, no. 7, pp. 1773–1778, Jul. 2008.
[15] S. Ruoho, E. Dlala, and A. Arkkio, "Comparison of demagnetization models for finite-element analysis of permanent-magnet synchronous machines," *IEEE Trans. Magn.*, vol. 43, no. 11, pp. 3964–3968, Nov. 2007.
[16] J. Pyrhönen, H. Jussila, Y. Alexandrova, P. Rafajdus, and J. Nerg, "Harmonic loss calculation in rotor surface magnets—New analytic approach," *IEEE Trans. Magn.*, vol. 48, no. 8, pp. 2358–2366, Aug. 2012.

Juha Pyrhönen (M'06) received the M.Sc. degree in electrical engineering and the Licentiate of Science and D.Sc. degrees in technology from Lappeenranta University of Technology (LUT), Lappeenranta, Finland, in 1982, 1989, and 1991, respectively.

Since 1993, he has been with the Department of Electrical Engineering, LUT Energy, School of Technology, LUT, where he initially served as an Associate Professor and has been a Professor in electrical machines and drives since 1997. From 1998 to 2006, he also worked as the Head of the same department. He is active in the research on and the development of electric motors and electric drives.

Sami Ruoho (M'10) received the M.Sc. degree in applied physics from Turku University, Turku, Finland, in 1997 and the D.Sc. degree in technology from Aalto University, Espoo, Finland, in 2011.

He is an independent researcher. His research interests include the properties of rare-earth magnets and the electromagnetic and thermal modeling of electromagnetic devices.

Janne Nerg (M'99–SM'12) received the M.Sc. degree in electrical engineering and the Licentiate of Science and D.Sc. degrees in technology from Lappeenranta University of Technology (LUT), Lappeenranta, Finland, in 1996, 1998, and 2000, respectively.

He is currently an Associate Professor with the Department of Electrical Engineering, LUT Energy, School of Technology, LUT. His research interests include the field of electrical machines and drives, particularly the electromagnetic and thermal modeling and design of electromagnetic devices.

Martti Paju (M'05) received the M.Sc. degree in physical metallurgy and the Licentiate of Science and D.Sc. degrees in technology from Helsinki University of Technology, Espoo, Finland, in 1981, 1983, and 1990, respectively.

He is currently the Director of the Magnet Technology Centre, Prizztech Oy, Pori, Finland. His research interests include the field of permanent-magnet materials and their properties and applications.

Sampo Tuominen received the M.Sc. degree in applied physics from the University of Turku, Turku, Finland, in 2009.

Since graduating in 2009, he has been with the Magnet Technology Centre, Prizztech Oy, Pori, Finland, where he is currently the Manager of Magnetic Measurement Services. His research interests include the material properties of hard magnetic materials.

Harri Kankaanpää received the M.Sc. and Ph.D. degrees in physics from the University of Jyväskylä, Jyväskylä, Finland, in 1996 and 2001, respectively.

Since 2007, he has been with Neorem Magnets Oy, Ulvila, Finland, where he is an Application Engineer. His current research interests include permanent-magnet applications and measurement development.

Raivo Stern received the M.Sc. degree in condensed matter physics from Tartu University, Tartu, Estonia, in 1987 and the Ph.D. degree in solid-state physics from Zürich University, Zürich, Switzerland, in 1995.

He is currently a Senior Research Associate with the Department of Chemical Physics, National Institute of Chemical Physics and Biophysics (NICPB), Tallinn, Estonia, where he has also been serving as the Director of the NICPB since 2006. His research interests include the field of various modern materials, particularly quantum magnets, string permanent magnets, and unconventional superconductors.

Aldo Boglietti (M'04–SM'06–F'12) was born in Rome, Italy, in 1957. He received the Laurea degree in electrical engineering from the Politecnico di Torino, Turin, Italy, in 1981.

In 1984, he started his work as a Researcher of electrical machines with the Department of Electrical Engineering, Politecnico di Torino, where he was an Associate Professor of electrical machines in 1992, was the Head of the department from 2003 to 2011, and has been a Full Professor since November 2000. He is the author of more than 130 papers in the field of energetic problems in electrical machines and drives, high-efficiency industrial motors, magnetic materials and their applications in electrical machines, electrical machine and drives models, and thermal problems in electrical machines.

Prof. Boglietti is the Chair of the Electric Machine Committee of the IEEE Industry Applications Society. He is an Associate Editor of the IEEE TRANSACTIONS ON INDUSTRIAL ELECTRONICS and a Reviewer for IEEE and other international journals.

Nikita Uzhegov (S'14) received the B.Sc. degree from Moscow Power Engineering Institute, Moscow, Russia, in 2010 and the M.Sc. degree in electrical engineering from Lappeenranta University of Technology (LUT), Lappeenranta, Finland, in 2012. He is currently working toward the Ph.D. degree in the Department of Electrical Engineering, LUT Energy, School of Technology, LUT.

His main research interests include electrical machines and drives, particularly high-speed machines.

ACTA UNIVERSITATIS LAPPEENRANTAENSIS

664. KLEMOLA, KATJA. Tuottavuuden, vaikuttavuuden ja kustannusvaikuttavuuden arviointi alueellisesti integroiduissa sosiaali- ja terveyspalveluissa – palvelujen käyttöön perustuva malli ja esimerkkejä. 2015. Diss.

665. HEROLD, KRISTIINA. Impact of Word-of-Mouth on consumer decision-making: An information processing perspective in the context of a high-involvement service. 2015. Diss.

666. OLABODE, MUYIWA. Weldability of high strength aluminium alloys. 2015. Diss.

667. VANHALA, ERNO. The role of business model in computer game development organizations. 2015. Diss.

668. SALAMPASIS, DIMITRIOS. Trust-embedded open innovation: Towards a human-centric approach in the financial industry. 2015. Diss.

669. DE SMET, DIETER. Innovation ecosystem perspectives on financial services innovation. 2015. Diss.

670. PORRAS, PÄIVI. Utilising student profiles in mathematics course arrangements. 2015. Diss.

671. SALMINEN, JUHO. The role of collective intelligence in crowdsourcing innovations. 2015. Diss.

672. ROSAS, SAILA. Co-operative acquisitions – the contextual factors and challenges for co-operatives when acquiring an investor-owned firm. 2015. Diss.

673. SINKKONEN, TIINA. Item-level life-cycle model for maintenance networks – from cost to additional value. 2015. Diss.

674. TUUNANEN, JUSSI. Modelling of changes in electricity end-use and their impacts on electricity distribution. 2015. Diss.

675. MIELONEN, KATRIINA. The effect of cationic-anionic polyelectrolyte multilayer surface treatment on inkjet ink spreading and print quality. 2015. Diss.

676. OMAJENE, JOSHUA. Underwater remote welding technology for offshore structures. 2015. Diss.

677. NUUTINEN, PASI. Power electronic converters in low-voltage direct current distribution – analysis and implementation. 2015. Diss.

678. RUSATSI, DENIS. Bayesian analysis of SEIR epidemic models. 2015. Diss.

679. STRAND, ELSI. Enhancement of ultrafiltration process by pretreatment in recovery of hemicelluloses from wood extracts. 2016. Diss.

680. TANNINEN, PANU. Press forming of paperboard – advancement of converting tools and process control. 2015. Diss.

681. VALTONEN, PETRI. Distributed energy resources in an electricity retailer's short-term profit optimization. 2015. Diss.

682. FORSSTRÖM-TUOMINEN, HEIDI. Collectiveness within start up-teams – leading the way to initiating and managing collective pursuit of opportunities in organizational contexts. 2015. Diss.

683. MAGUYA, ALMASI. Use of airborne laser scanner data in demanding forest conditions. 2015. Diss.

684. PEIPPO, JUHA. A modified nominal stress method for fatigue assessment of steel plates with thermally cut edges. 2015. Diss.

685. MURASHKO, KIRILL. Thermal modelling of commercial lithium-ion batteries. 2016. Diss.

686. KÄRKKÄINEN, TOMMI. Observations of acoustic emission in power semiconductors. 2016. Diss.

687. KURVINEN, EMIL. Design and simulation of high-speed rotating electrical machinery. 2016. Diss.

688. RANTAMÄKI, JUKKA. Utilization of statistical methods for management in the forest industry. 2016. Diss.

689. PANOVA, YULIA. Public-private partnership investments in dry ports – Russian logistics markets and risks. 2016. Diss.

690. BAHARUDIN, EZRAL. Real-time simulation of multibody systems with applications for working mobile vehicles. 2016. Diss.

691. MARTIKAINEN, SOILI. Development and effect analysis of the Asteri consultative auditing process – safety and security management in educational institutions. 2016. Diss.

692. TORVINEN, PEKKA. Catching up with competitiveness in emerging markets – An analysis of the role of the firm's technology management strategies. 2016. Diss.

693. NORONTAUS, ANNUKKA. Oppisopimuskoulutus yritysten tuottamana koulutuspalveluna: tavoitteista vaikutuksiin. 2016. Diss.

694. HALMINEN, OSKARI. Multibody models for examination of touchdown bearing systems. 2016. Diss.

695. TALONPOIKA, ANNA-MARIA. Financial working capital – management and measurement. 2016. Diss.

696. INKINEN, HENRI. Intellectual capital, knowledge management practices and firm performance. 2016. Diss.

697. YANG, XIAOCHEN. Development of a welding production quality control and management system model for China. 2016. Diss.

698. LEMINEN, VILLE. Leak-proof heat sealing of press-formed paperboard trays. 2016. Diss.

699. LAAKSONEN, LAURI. Spectral retinal image processing and analysis for ophthalmology. 2016. Diss.

700. OINONEN, MINNA. Management of customer co-development in business-to-business markets. 2016. Diss.

701. ALATALO, SARA-MAARIA. Hydrothermal carbonization in the synthesis of sustainable porous carbon materials. 2016. Diss.